UNIVERSIDADE FEDERAL DO RIO GRANDE DO SUL
INSTITUTO DE FÍSICA
PROGRAMA DE PÓS-GRADUAÇÃO EM MICROELETRÔNICA

RICARDO AUGUSTO ZANOTTO RAZERA

Hybrid Organic-Inorganic Perovskite Solar Cells: Analysis of Performance and Stability in Reverse Bias

Thesis presented in partial fulfillment
of the requirements for the degree of
PhD in Microelectronics

Advisor: Prof. Dr. Henri Ivanov Boudinov
Coadvisor: Prof. Dr . Adriano Friedrich Feil

Porto Alegre
April 2021

RICARDO AUGUSTO ZANOTTO RAZERA

Hybrid Organic-Inorganic Perovskite Solar Cells: Analysis of Performance and Stability in Reverse Bias

Orientador: Dr. Henri Ivanov Boudinov

Coorientador: Dr. Adriano Friedrich Feil

Porto Alegre

April 2021

Aos meus pais, que sempre colocaram a educação dos filhos acima de todo o resto.

Abstract

Lead-halide perovskites show great promise for high-efficiency Si/perovskite tandem solar cells, with record efficiencies now surpassing 25 % in single junction. However, to reach commercialization, it is necessary for the cell to be stable under several stressing conditions that the field imposes, such as currents up to 25 $\mathrm{mAcm^{-2}}$, voltages from -1.2 V to 1.2 V, temperatures up to 85 °C, illuminations of more than 1000 $\mathrm{Wm^{-2}}$ and humidities up to 100 %. This work first presents an extensive review of these problems and the solutions that have appeared so far. Then, the methods and layer recipes that we used to fabricate perovskite solar cells and study these problems are described. Results of substructures containing individual layers of TiO_2 and poly(3-hexylthiophene-2,5-diyl) (P3HT) are then analyzed, showing how they influence the final device by introducing series resistance and interface recombination. We then move on to describe complete solar cells with formamidinium/cesium lead iodide/bromide as the perovskite, using techniques such as current-voltage scans, maximum power point tracking, external quantum efficiency, photoluminescence, dark lock-in thermography and electron microscopy. We finish by describing the instabilities of these solar cells caused by reverse biases. These damages can be triggered by reverse voltages as low as -0.3 V for opaque solar cells. We demonstrate that at least four main processes occur when reverse voltages are applied, such as electrochemical reactions between layers, phase transitions of the perovskite and metal migration from the electrodes.

Abstract

Perovskitas de chumbo-halogênio apresentam uma grande promessa para células solares tandem de Si/perovskita de alta eficiência, com eficiências recorde ultrapassando 25 % em monojunção. No entanto, para alcançar comerciabilidade, é necessário que a célula seja estável sob muitas condições de estresse que o campo introduz, como correntes até 25 mAcm^{-2}, tensões de -1.2 V até 1.2 V, temperaturas de até 85 °C, iluminações de mais de 1000 Wm^{-2} e humidades de até 100 %. Este trabalho primeiramente apresenta uma extensiva revisão destes problemas e das solução que apareceram até agora. Então, os métodos e receitas de camada que foram usados para fabricar células solares de perovskita são descritos. Resultados de subestruturas contendo camadas individuais de TiO_2 e poly(3-hexylthiophene-2,5-diyl) (P3HT) são analisadas, mostrando como elas influenciam o dispositivo final introduzindo resistência em série e recombinação de interface. Nós, então, seguimos em frente para mostrar células solares completas com formamidínio/césio chumbo iodeto/brometo como a perovskita, usando técnicas como varreduras de corrente/tensão, rastreamento de ponto de máxima potência, eficiência quântica externa, fotoluminescência, termografia de escuro por lock-in e microscopia eletrônica. Nós terminamos descrevendo as instabilidades destas células solares causadas por tensões reversas. Estes danos podem ser acionados por tensões reversas tão baixas quanto -0.3 V para células solares opacas. Nós demonstramos que pelo menos quatro processos podem ocorrer quando tensões reversas são aplicadas, como reações eletroquímicas entre camadas, transições de fase da perovskita e migração metálica dos eletrodos.

Artigos publicados pelo autor referentes a este trabalho

Artigos em periódicos:
1. “Anomalous Current–Voltage Behavior in Al/TiO2/n-Si Structures” na revista Physica Status Solidi Rapid Research Letters. DOI: 10.1002/pssr.201800057
2. “Instability of p-i-n perovskite solar cells under reverse bias” na revista Journal of Materials Chemistry A. DOI: 10.1039/c9ta12032g

Resumo apresentado em conferência:
1. “Stability of perovskite and two terminal Si/perovskite tandem solar cells under reverse bias”, apresentado pelo autor na conferência HOPV em Roma em 2019.

Contents

List of Figures

List of Tables

List of Symbols

I_{Earth}	energy current leaving Earth's surface
I_{Sun}	energy current reaching Earth's atmosphere from the Sun
I_{atm}	energy current leaving Earth's atmosphere
R_{Earth}	reflectivity of the Earth
Ω	solid angle
r	radius or reflection coefficient
σ	Stefan-Boltzmann's constant or conductivity or capture cross-section
T	temperature
g	Earth's gravity
p	pressure or hole density
A	area
m	mass
E	energy
$\hbar$	Planck's constant
ω	frequency
E_g	bandgap
t	perovskite's tolerance factor
μ	mobility
k	Boltzmann's constant or extinction coefficient
q	proton's charge
J_{sc}	short-circuit current
V_{oc}	open-circuit voltage
FF	fill factor
ϕ	quasi-Fermi level or phase
P	power
I	current
V	voltage or volume
J	current-density
J_0	saturation current-density
n	ideality factor or electron density or refractive index
J_L	light-generated current density

x	position
ϵ	relative dielectric constant
N_{ions}	concentration of ions
R	recombination rate density or resistance
G	generation rate density
J_n	electron current density
J_p	hole current density
B	radiative recombination constant
v_{th}	thermal velocity
N_t	density of midgap defects
n_i	intrinsic carrier concentration
p_0	hole concentration in thermal equilibrium
n_0	electron concentration in thermal equilibrium
τ	recombination lifetime
λ	wavelength
α	absorption coefficient
V_{bi}	built-in voltage
S	surface recombination velocity
W	layer thickness
η	efficiency
V_{mpp}	maximum power point voltage
J_{mpp}	maximum power point current
C	capacitance
c	speed of light
I	light intensity
EQE	external quantum efficiency
d	layer thickness
ϕ_F	workfunction
ϵ_0	dielectric constant of vacuum
Q	charge
N_D	donor doping density
N_A	acceptor doping density
V_{FB}	flatband voltage
L_D	Debye length
V_{bd}	breakdown voltage

Chapter 1

Introduction

The purpose of this chapter is two fold. First, a motivation to the study of solar energy is given, heavily based on the topic of climate change. There are other ways to motivate research on solar energy (e.g. by its space applications, the possibility of a distributed electricity generation system, the fact that it is a completely renewable source of energy), but we focus on climate change because of its current relevance to the global political scenario. Then, we move on to motivate the research on perovskite solar cells, a specific kind of solar cell which is the topic of this thesis. We arrive at the concept of tandem solar cells, which are currently the best promise for future high-efficiency solar cells. At last, we describe the objectives set by this thesis.

1.1 Climate Science

All consequences related to climate change can be traced back to two effects: the greenhouse effect and ocean acidification, both of which are caused by increases in concentration of the gas CO_2 in the atmosphere. Ocean acidification is a consequence of the fact that water is able to dissolve CO_2, so as its concentration increases in the atmosphere, more will be absorbed by the oceans. These in turn become acidic[1] because of the balances $CO_2 + H_2O \leftrightarrow HCO_3^- + H^+ \leftrightarrow CO_3^{2-} + 2H^+$, affecting many ecosystems and most sea-related food chains [2]. The greenhouse effect is a consequence of the fact that gas molecules such as CO_2, H_2O, O_3, CH_4, N_2O and chlorofluorcarbon (CFC) gases, henceforth called collectively as greenhouse gases (GHGs), have absorption bands in the infrared but not in the visible range of wavelengths. The peak of the Sun's spectrum is at 0.5 μm, in the visible range, so most of its radiation is only absorbed by the Earth's surface. On the other hand, the peak of the Earth's spectrum is at 2.4 μm, in the infrared range, so a large portion of it is absorbed by the atmosphere, which then heats up and re-radiates half of the absorbed radiation back to Earth. The planet warms up as a consequence of this trapped heat. Note that nitrogen (N_2) and oxygen (O_2) constitute about 99 % of the air and have no absorption lines in the near infrared, so they do not contribute directly to the greenhouse effect. However, they do influence the effect indirectly by pressure-broadening the absorption lines of the GHGs and by exchanging heat with them [3, 4].

---

[1] Actually, since the oceans are currently slightly basic [1], technically this effect causes the oceans not to become acidic but less basic, but the conclusion is the same.

It is possible to estimate Earth's surface temperature with a simple zero-dimensional model [5], illustrated in Fig. 1.1. The Sun sends an energy current I_{Sun} to Earth, the Earth sends an energy current I_{Earth} to the atmosphere and the atmosphere sends half of I_{atm} back to Earth and the other half to space. The critical simplifications are that the atmosphere is 1) completely transparent to solar radiation, 2) completely opaque to Earth's radiation, and 3) concentrated in a very thin layer with uniform temperature[2]. At steady-state, then,

$$I_{Earth} = I_{atm} \tag{1.1}$$

$$I_{Earth} = I_{Sun} + \frac{1}{2} I_{atm} \tag{1.2}$$

leading to

$$I_{Earth} = 2 I_{Sun} \tag{1.3}$$

I_{Sun} can be calculated from

$$I_{Sun} = (1 - R_{Earth}) \times \Omega r_{Sun}^2 \times \sigma T_{Sun}^4 = 1.2 \times 10^{17}\ W \tag{1.4}$$

where $R_{Earth} \approx 30\%$ is the reflectivity of Earth's surface, $\Omega = 5.70 \times 10^{-9}$ sr is the solid angle of the Earth as seen from the Sun, $r_{Sun} = 6.96 \times 10^8$ m is the Sun's radius, $\sigma = 5.67 \times 10^{-8}$ W/K^{4}m^2 is Stefan-Boltzmann's constant and $T_{Sun} = 5778$ K is the Sun's surface temperature. Since $I_{Earth} = 4\pi r_{Earth}^2 \sigma T_{Earth}^4$, Earth's temperature is, from Eq. (1.3),

$$T_{Earth} = \sqrt[4]{2 \frac{I_{Sun}}{\sigma 4 \pi r_{Earth}^2}} = 302\ K \tag{1.5}$$

where $r_{Earth} = 6.37 \times 10^6$ m is Earth's radius. The actual mean surface temperature of the Earth is about 288 K, 14 °C lower than what Eq. (1.5) predicts, although it is increasing by a few tenths of a degree per decade [7]. The overestimation comes from the simplifications: some of the Sun's radiation is in the infrared and is absorbed by the atmosphere before reaching the Earth, meaning a value of I_{Sun} in Eq. (1.5) lower than that from Eq. (1.4) should be used instead. Furthermore, the atmosphere is not infinitely thick and not all wavelengths emitted by the Earth are in the absorption bands of the atmosphere, so some of Earth's radiation escapes from the atmosphere's trap. At the opposite extreme, where the atmosphere is completely transparent to infrared radiation, there would be no factor of 2 inside the forth-root in Eq. (1.5) and Earth's temperature would be 254 K. Liquid water would not be present and complex life as we know it would have never sprung on Earth.

This calculation shows that, as the Earth's atmosphere becomes more and more opaque to infrared radiation, the planet will gradually warm. A common source of confusion in the popular media regarding this topic is the fact that CO_2 is not the main contributor to the infrared-opacity of Earth's atmosphere [3]. Water vapor is. This is because water has stronger absorption lines than CO_2 and because it is present in larger quantities in the air. (The concentration of H_2O in air can be as high as a few percent in humid, warm days.) More precisely, water vapor accounts for about 50 % of the total

---

[2] We also ignore the heat coming from Earth's core, which is $\sim$ 0.01 mW/cm^2 [6] and therefore negligible compared with the average heat coming from the Sun, $\sim$ 30 mW/cm^2.

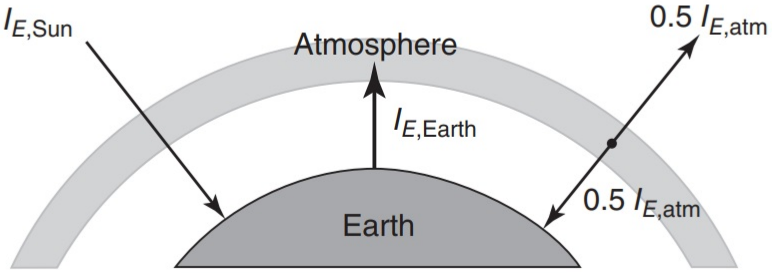

Figure 1.1: Energy current balance between Earth, atmosphere and Sun. From [5].

greenhouse effect in Earth, while clouds account for about 25 %, CO_2 for about 20 % and the other GHGs together for about 5 % [3]. However, water condenses as it moves up into the atmosphere and is constantly being cycled between liquid form, water vapor, clouds and rain. If no warming from the other, non-condensable GHGs (namely all the other ones besides H_2O) was present, water vapor would condense (and freeze), leave the atmosphere and have no further contribution to the greenhouse effect. Therefore, although water is indeed the most potent GHG, it is only an amplification factor for the non-condensable GHGs [3, 8]. Carbon dioxide is currently the main contributor in this category and therefore is the one that receives the most attention.

There is overwhelming evidence [7] that in the pre-industrial ages, when carbon dioxide levels were at 280 ppm (they are currently at around 410 ppm [9]), the globe's temperature was about 1 °C lower. Furthermore, if the current CO_2 emissions continue at the same levels they are today, it is predicted that by 2100 the Earth's temperature will have risen by another ~ 1 °C [10]. Of course, a 2 °C increase in the mean surface temperature does not mean the end of life on Earth[3]. The real problem is in the possibility that this warming triggers uncontrollable positive feedback loops, although it is not known how high Earth's temperature would have to become. One of these feedback loops is that of water vapor and was already explained. Some of the other ones are [10–13]: melting of ice from glaciers, decreasing the reflectivity of Earth; melting of methane hydrates from the oceans floor releasing methane (which is also even more infrared-absorbing than CO_2); decrease of solubility of CO_2 in the oceans' water caused by increasing temperature, releasing even more CO_2 to the atmosphere; and the increase in probability of wild fires in forests, again releasing more CO_2. All these effects can generate runaway greenhouse effects where the temperature of the planet becomes incredibly high. In fact, this is currently the best hypothesis for what happened with the planet Venus [8], with its 90 bar atmosphere composed 99 % of CO_2 and with surface temperatures of about 475 °C.

It should be noted that many important industries would be affected if we suddenly decided that no CO_2 is to be emitted any longer. The (not electric) car and aviation industry depends on burning petroleum products, the electricity production industries, especially in China and the United States, depend heavily on burning diesel, coal or natural gas to run steam turbines, the construction industry depends on the calcination reaction ($CaCO_3 \rightarrow CaO + CO_2$) to produce cement (which also requires high tempera-

---

[3] However, this warming is sufficient to increase the sea level by about 3 mm per year, change agriculture and fishing patterns and cause more frequent and intense extreme-weather events [10]. It is currently unknown the cost that these effects will have on the global economy.

tures and therefore a lot of electricity) and the agriculture and ranching industry depends on the "slash and burn" technique to clear land and on the emission of other greenhouse gases by animals (methane) and fertilization of soil (nitrous oxide). Therefore, given the typical human cognitive biases, it should be no surprise that a lot of skepticism revolves around the theme of climate change for those whose lives depend directly on these sectors of the economy, which is about everyone in the world. It becomes extremely important to check if these effects are indeed caused by human activities. The evidences that the Earth is warming and that the concentration of CO_2 in the atmosphere is increasing are by now quite undisputed [10], but correlation does not always mean causation. The two best arguments provided for the possibility that global warming caused by CO_2 emissions is not necessarily what is happening with the Earth are 1) that the increase in CO_2 could be coming not from human sources but rather from other natural processes and 2) that, even if it were, the Earth's surface temperature increase could be caused not by the "tiny 0.04 % concentration of CO_2", but by an increase in the Sun's brightness. If either of these possibilities is true, it would still mean that we have a global warming problem, but not that the industries are the ones to blame.

Unfortunately, plenty of evidence shows that these arguments are not factual [10]. The second argument was refuted by directly measuring the Sun's brightness overtime and comparing with measurements of Earth's surface temperature, as shown in Fig. 1.2a. In the last 50 years, the Sun actually became slightly dimmer, while the Earth's temperature continued increasing, refuting the hypothesis. The first argument, that perhaps CO_2 emissions come mainly from natural processes, can also be directly proven incorrect by measuring the ratio of ^{13}C to ^{12}C in the air. Living organisms have a lower ratio of ^{13}C to ^{12}C than the air because of the mechanisms behind photosynthesis, which preferentially absorb $^{12}CO_2$ over $^{13}CO_2$ to form sugars and wood [14]. Now, if emissions come mainly from humans (meaning almost entirely by fossil fuels, which were once living organisms performing photosynthesis[4]), we expect the ^{13}C to ^{12}C ratio in the air to decrease, while if it comes from natural processes (meaning almost entirely from outgassing of the oceans, which does not differentiate between ^{13}C and ^{12}C) we expect it to be constant. Measurements have shown [15] it is in fact decreasing, as shown in Fig. 1.2b. It is actually incorrect to think that (at constant temperature) outgassing of CO_2 from the oceans increases the carbon concentration in the atmosphere, because at the same time that oceans release CO_2, they absorb CO_2; the system is in balance. It is human emissions and global warming itself, through one of the positive feedback loops, that change this balance.

---

[4] Unlike ^{14}C, ^{13}C is stable, so it does not decay even after millions of years.

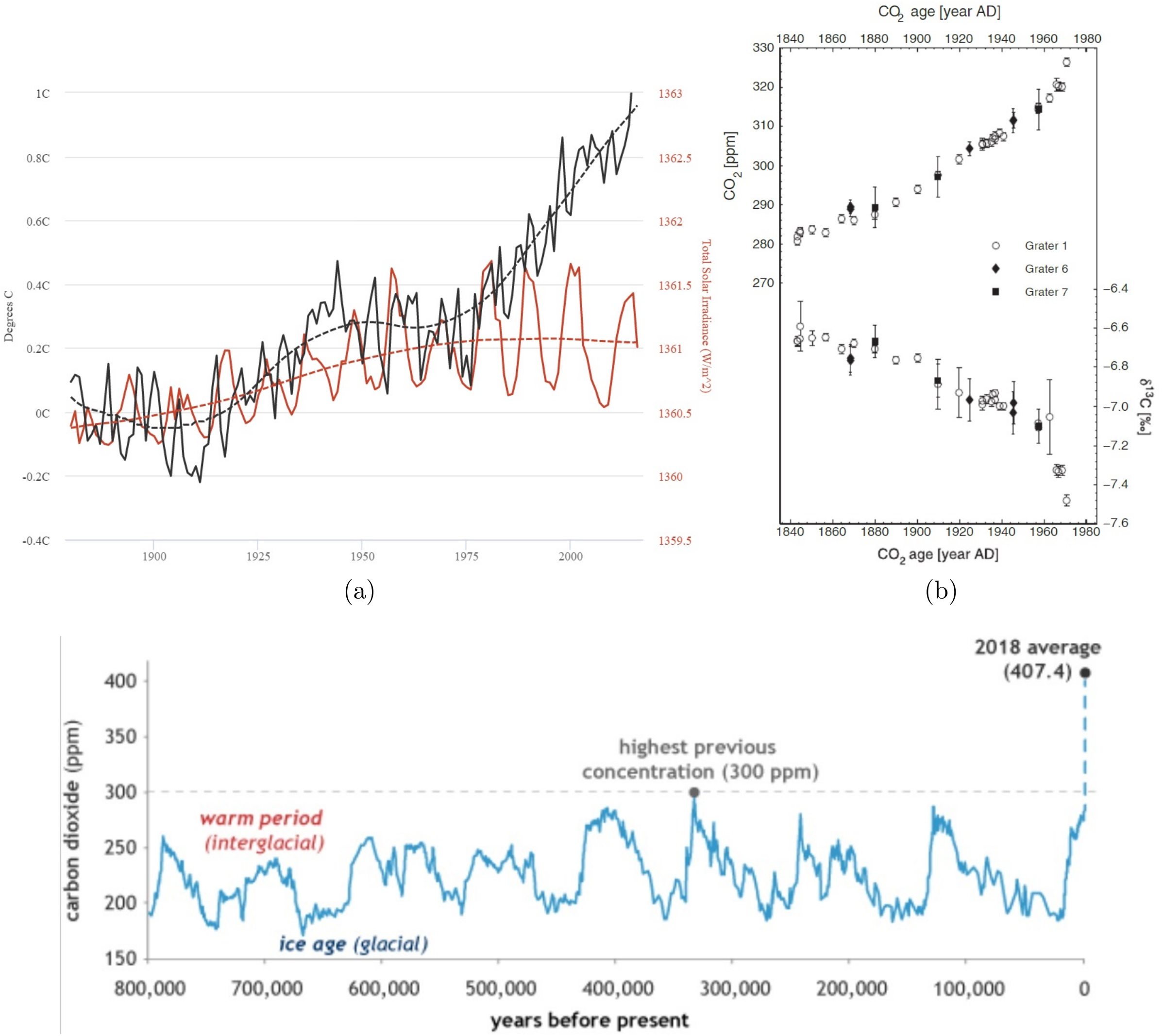

(a) (b)

(c)

Figure 1.2: Evidences that CO_2 increase is caused by burning fossil fuels and not natural causes. a) Earth's surface temperate anomaly (i.e., difference between instanteneous temperature and mean temperature), left axis, and total solar irradiance, right axis. b) Concentration of CO_2 in the atmosphere, left axis, and fraction of ^{13}C in CO_2, right axis. From [15]. c) CO_2 concentration over the past hundreds of thousands of years. From [16].

Perhaps even more convincing are the measurements of Earth's mean surface temperature and atmospheric CO_2 concentration over the past hundreds of thousands of years, such as the one shown in Fig. 1.2c. This data can be obtained via geological methods, for example by measuring the concentration and isotope fraction of carbonated rocks dated to hundreds of thousands to millions of years ago [16]. These graphs became known as "hockey stick" graphs because of the shape of the curve [7]. It would be an incredible coincidence if it was by some mysterious effect that right in 1850, in the beginning of the industrial revolution, the Earth's temperature and CO_2 concentration suddenly started to increase on its own at the fastest rate observed in the last hundreds of thousands of years [7, 16].

There is also a third argument sometimes used against climate change scenarios: even if CO_2 is increasing because of humans and even if it caused the warming observed so far, further increasing the CO_2 concentration in the atmosphere could not further increase Earth's surface temperature because the CO_2 currently present in the atmosphere is already enough to absorb all the infrared emitted by the Earth, so adding more makes no difference. The atmosphere is allegedly already saturated with CO_2 and the dependence of warming on CO_2 concentration is logarithmic, meaning that each additional CO_2 causes less warming than the previous addition. As it turns out, this argument is wrong in many ways [8]. First, the current concentration of CO_2 is not in the level of saturation yet [10]. Second and more importantly, even if it were, it is not just the fact that CO_2 absorbs infrared that warms the Earth, but also that it re-emits half of what it absorbed back to Earth and the other half to space. Refering to Fig. 1.1, emitting more CO_2 is like adding more infrared absorbing layers on top of the already existing ones, compounding greenhouse effects on everything underneath the last layer. In fact, one can add more layers of atmosphere to this model and prove that the temperature of the Earth with n infrared-absorbing layers, T_n, would be

$$T_n = \sqrt[4]{n+1}\, T_0 \tag{1.6}$$

where $T_0 = 254$ K is what Earth's temperature would be with no layers (i.e., with no atmosphere) [5]. It is clear that with an arbitrarily large number of layers the temperature of the Earth is arbitrarily large. Of course, at some point T_n would be as large as the Sun's temperature and the assumptions of the model (that the atmosphere is transparent to the Sun's radiation but not to that of Earth) would become invalid, but the model still proves that adding more infrared-absorbing layers would increase the planet's temperature [8]. Third, saturation only applies to each GHG separately[5], so positive feedback loops involving other GHGs would still be of worry even if the saturation argument was valid.

As a final note on the topic, we mention that the claim that fossil fuel reserves are about to finish is misleading. Indeed, estimates give ~ 50 years (a very low number) until we run out of oil [17], but these estimates only take into account the known reserves. However, it is possible to estimate the total amount of carbon in fossil fuels, also accounting for the reserves that haven't been found yet, as follows [5]. In the first years of Earth's formation most of the atmosphere was CO_2 and N_2, with no O_2, because with the temperatures prevailing at this stage of Earth's formation any O_2 would quickly react with any form of carbon. It was during the billions of years while the Earth was cooling down and photosynthesis was converting CO_2 into O_2 plus sugars that the carbon was slowly being put to solid form. The atmosphere then became oxygenated; the oxygen in the air came from the photosynthesis that produced the living organisms that later became fossil fuels. Therefore, as long as there is oxygen in the air, there must be carbon in the ground for us to burn. The mass of oxygen in the air, m_{O_2}, can be calculated from the mass of air in the atmosphere, m_{air}, which can be obtained from $m_{air} \times g = p \times A_{Earth}$, where $g = 9.8$ m/s^2 is the acceleration of gravity, $p = 10^5$ N/m^2 is the atmospheric pressure and $A_{Earth} = 5.1 \times 10^{14}$ m^2 is Earth's surface area, giving $m_{air} = 5.2 \times 10^{18}$ kg. Since 20 % of the air is oxygen, $m_{O_2} = 1.0 \times 10^{18}$ kg. The mass of carbon is 12/32 the mass of O_2 in the molecule of CO_2, so the mass of carbon in the ground is 3.9×10^{17} kg.[6] About

---

[5] More precisely, to each infrared absorption band separately.

[6] This carbon mass also accounts for the plants and animals (including people) alive today, so not all

1.04×10^{16} kg of carbon in coal, natural gas and petroleum have been found so far [20], accounting for only 3 % of the reserves. Note that this is probably an underestimation to the true size of the total reserves, because it does not account for all the oxygen that was formed by photosynthesis but reacted with Fe, Si, Mg and Ca to form their respective oxides, the most abundant rocks on Earth's surface. Also, it neglects the fact that fossil fuels also have other atoms beside carbon, like H, N and O, that further increase their mass. At some point something will stop us from burning stuff for energy, but it will not be lack of stuff to burn.

1.2 A Solution: Photovoltaic Power

Having shown that a serious problem faces humanity, we turn to solutions. The most obvious one is to stop emitting CO_2, but doing so without sacrificing all the progress in society development. A recent assessment [20] by the International Energy Agency (IEA) puts the transportation and electricity generation industries as the two largest emitters of CO_2, holding 65 % of all emissions. For the transportation industry, there are two known ways to eliminate emissions coming from combustion engines: 1) to not use combustion engines at all and substitute for electric cars and 2) to use engines that burn fuels other than gasoline or diesel, such as hydrogen (which would emit water) or alcohol. Burning alcohol also emits CO_2, but since ethanol comes from biomass, which comes from the CO_2 in the air, the net result of burning it is no CO_2 increase; it is said to be a carbon-neutral technology. The disadvantage is the vast amounts of other resources such as water and land required to grow biomass. Electric cars, on the other hand, emit no CO_2, but they increase the demand of electrical energy. If this energy comes from CO_2 emitting sources, no benefit will result, only a simple shift of emissions from the transportation sector to the electricity generation sector. Thus, a clean source of electricity is urgently needed. In this thesis, we advocate this source to be solar power.

It was calculated in the last section that a total of 1.2×10^{17} W arrive at the Earth from the Sun (already discounting the reflected part). The Earth's atmosphere absorbs and scatters part of this power, so the incident power on a small area of the Earth's surface depends on the thickness of atmosphere between the surface and outer space or, in other words, it depends on the direction of the Sun in the sky. Very roughly, when the Sun is directly overhead on a clear sky and the observer is at sea level, the atmosphere absorbs about 30 % of the incident power, while at sunset it absorbs about 70 % (for more precision, see Refs. [21,22]). So, ignoring clouds, about 50 % or 6×10^{16} W of power arrives at (half of) the Earth's surface as sunlight. In the year of 2017, the total amount of electrical energy that humans produced was about 2.9×10^{16} Wh [20, 23]. Thus, if humans were to cover the entire surface of the Earth with solar panels with an efficiency of 15%, it would take about 3.2 h for these solar panels to produce all the energy they

---

of it is in the form of fossil fuels, although we can, and do, also burn the currently alive plants for energy. In any case, the carbon mass in the animals alive today is negligible compared to the carbon mass of all animals that have ever lived. It takes ~ 50 million years for plants and animals to become fossil fuels during sedimentation [18], but life has existed on Earth for about 4000 million years, so we estimate that about 98.7 % of the calculated carbon mass is fossil fuels. More precise estimates put the carbon mass on alive animals and plants at 5.5×10^{14} kg [19], giving a value of 99.94 % for the fossil fuels part of the total carbon mass.

needed for the year.

Of course, although these numbers look promising, the assumption that humans can cover the entire surface of the Earth with solar panels is a problem. A more realistic assumption is to cover only the surface needed for the power produced to meet the power demanded. If it takes 3.2 hours to produce an year's worth of energy with an Earth's area of solar panels, in 1 year = 8760 hours it would take an area of 9.3×10^{10} m^2 of solar panels (about a third of the size of the state of Rio Grande do Sul, Brazil). By the end of 2016, the installed photovoltaic (PV) capacity was approximately 7.5×10^{10} W [24, 25], which, if one considers an average of 300 W and 2 m^2 per panel, gives an installed area of 5×10^8 m^2. Therefore, ignoring any increase in demand, humans need to increase their solar power capacity by a factor of 186 if they want to be completely fueled by solar energy.

Two problems must be faced in order to produce all these solar cells. The first is the time it takes. In 2017 the world PV production capacity reached about 100 GW per year [25]. (For 300 W per panel, this means 3.8×10^4 panels and 2.7×10^6 cells per hour. If there are about 50 industries in the world, each produces an impressive average of 5.3×10^4 solar cells per hour.) Nevertheless, at this rate, it would take about 200 years to produce all the solar panels needed, which is unacceptable. We must find ways to make more efficient solar panels with a faster method and build more industries.

The second problem is the resources it takes. A common way to quantify this problem is by the levelized cost of electricity (LCOE), which is the minimum price that 1 kWh of solar energy must be sold at so that the investment in the solar system is exactly paid off by the end of its projected lifetime. The world average LCOE for various types of power sources is plotted in Fig. 1.3 for the last two decades, showing the abrupt drop in solar energy price. The main reason for this cost decrease is related to the economies of scale associated with huge production facilities built in the last decade, mainly in China [26]. In any case, clearly PV is finally becoming financially competitive with the other power sources and it is reasonable to believe that solar energy will become a major energy source in the next few decades [23].

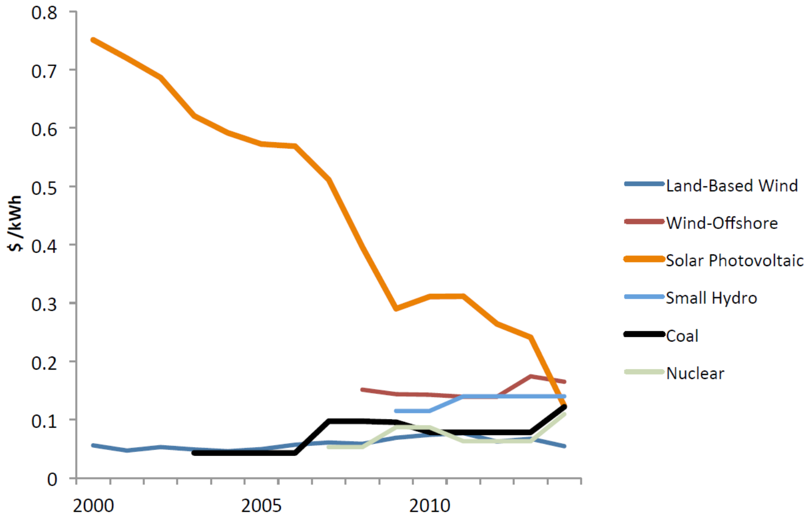

Figure 1.3: World average levelized cost of electricity for various power sources. Data from the International Energy Agency [23].

Currently the best method to further reduce cost is to increase efficiency of the solar cells. The reason is the following. The market of solar panels is dominated by the mono-junction Si technology [25], where Si solar cells are made from Si wafers and connected together to form modules. A considerable cost is associated to both the manufacturing process and the raw materials, but, currently, about half of the cost of the PV system comes from the other devices besides the solar panels, like the inverter, mounting structure, connection cables and installation (see Ref. [25] for a detailed cost analysis of each industry involved in solar cell manufacturing). For utility scale the land itself also adds a considerable cost. However, except for the inverter, all these other costs are, like the panels themselves, area-related and would be reduced if the efficiency of the cells was increased. Furthermore, only about 25 % of the solar cell production cost comes from turning silicon wafers into solar cells, the remaining coming from growing the wafers, wiring cells together to produce modules and from encapsulation. Now, if each cell is more efficient, less cells have to be produced and all these other costs are reduced, lowering the cost of PV systems.

1.2.1 Improving Solar Cell Technology

Efficiency is thus the key concern. The record efficiency for Si solar cells is currently 26.6 % [27], although commercial cells are usually in the range of 18-22 % efficiency depending on the technology employed by the manufacturer. Unfortunately, it is very hard to go much beyond these numbers because there are limits to how efficient a solar cell can be [28]. First, the second law of thermodynamics imposes a limit of $1 - 4T_{Earth}/3T_{Sun} + T_{Earth}^4/3T_{Sun}^4 = 93.1\%$ [29] to a solar converter that produces no entropy[7]. However, solar cells made from semiconductors do produce entropy [30] even if fully-concentrated light is used, so the limiting efficiency is lower and turns out to be 86.8 % [31] if an infinite number of different bandgaps are used to convert each wavelength of the solar spectrum. If only one bandgap is used, as is the case for today's commercial solar cells made from silicon, the limit is very much lower for three reasons: 1) photons that have energy lower than E_g are not absorbed, where E_g is the bandgap's energy; 2) photons that have energy higher than E_g lose most of their excess energy, $\hbar\omega - E_g$, by heating the cell (because phonon absorption and emission are usually too fast to be prevented); and 3) there is always at least one mechanism of recombination, namely radiative recombination. Taking these additional losses into account, Shockley and Queisser (SQ) [32] determined the theoretical limit of efficiency as a function of bandgap if only these losses are present. This limit is plotted in Fig. 1.4 for 100 mW/cm^2 incident power and AM1.5G spectrum. The SQ limit for silicon solar cells, which have bandgap of 1.1 eV, is 31%. However, in silicon, Auger recombination is actually even more important than radiative recombination and, when one takes into account this additional recombination mechanism, the actual limit is 29.4% [33]. The additional losses present in the record efficiency of 26.6 %, which are at least theoretically avoidable, come from reflection from the surfaces, non perfect light trapping for infrared photons, the presence of defects in the lattice which provide an

---

[7] The Carnot efficiency would be $1 - T_{Earth}/T_{Sun} = 95\%$, but solar cells are not Carnot engines. They are not even engines in the usual thermodynamic sense, but are rather the instrument that produces work in some abstract engine in which the working substance is the radiation field between the Sun and the Earth.

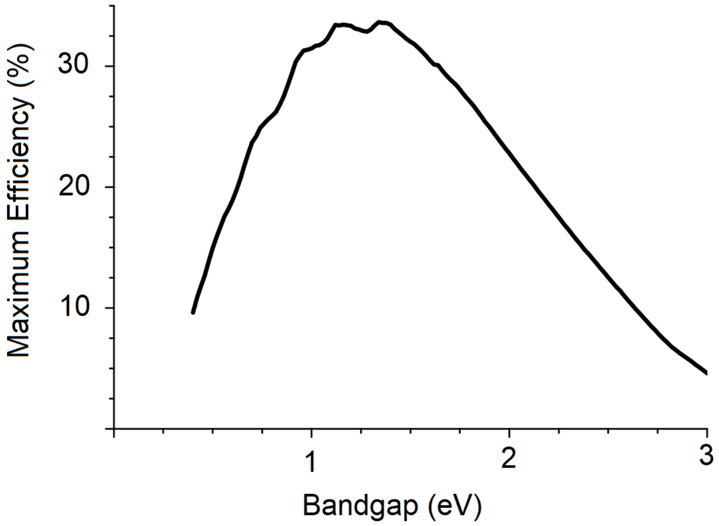

Figure 1.4: Shockley-Queisser limit for single junction solar cells illuminated with AM1.5G spectrum at irradiance of 100 mW/cm^2. The non-smooth character of the curve's peak is caused by the non-perfectly blackbody spectrum of AM1.5G radiation, a consequence of atmosphere absorption.

additional recombination mechanism and non-zero series resistance from the contacts [27]. Therefore, although the industry still has some room for improvement in cell efficiency when compared to the laboratory record of 26.6 %, it is clear that the technology is reaching its theoretical limit.

Worst still, even searching for new absorber materials will not provide much room for efficiency improvement in single junction solar cells, because even if the optimal bandgap of 1.44 eV is used, the theoretical maximum efficiency is only 33 %. Indeed, gallium arsenide solar cells, with bandgap of 1.42 eV, already have a close-to-optimum record efficiency of 29.1 % [34], but no scalable methods of producing such efficient cells are known. The straightforward conclusion would be that the only remaining option for cell improvement is to find cell designs and materials that provide efficiencies similar to those of Si but with lower manufacturing costs[8]. It is with this promise that, in 2009, a new type of solar cell technology appeared in the research community. [35,36] The technology has been called hybrid organic-inorganic perovskite solar cells, or just perovskite (PK) solar cells for short. We will concentrate the rest of this thesis on explaining how this new type of solar cell works and why it holds so much potential as the future of PV.

1.3 Hybrid Organic-Inorganic Perovskites

1.3.1 Material Properties

The name perovskite refers to a class of materials with chemical formula ABX_3, where A is called the cation of the PK, B is usually a transition metal and X is the anion of the PK. These elements form a unit cell where the B and X form a BX_6 octahedron and the

---

[8] Tandem solar cells, discussed later on, violate this conclusion.

A sits in the spaces in between the octahedra, as illustrated in Fig. 1.5a. In a crystal, this unit cell can be replicated in an orthorhombic, hexagonal, tetragonal or cubic lattice depending on temperature and pressure. All the different lattices are still called perovskites, but only the tetragonal and cubic ones lead to the semiconductors relevant for solar cells because the other ones have too large bandgaps [37]. The first mineral identified with the perovskite structure was $CaTiO_3$ back in 1839. For PV applications, the perovskites of interest are hybrid organic-inorganic materials, with the most studied composition being $CH_3NH_3PbI_3$ [38], or MALI for short. Methylammonium (MA, CH_3NH_3) is the organic part and occupies the cation position, Pb is the transition metal and I is the halogen, forming together the inorganic part. At room temperature, MALI has a tetragonal lattice which transitions to cubic at 54 °C [39]. It has a direct bandgap of 1.61 eV at room temperature [39]. Other common PK compositions involve formamidinium (FA, $CH(NH_2)_2$) or Cs as the cation, Br and Cl as the anion and Sn as the metal. Mixed-cation, mixed-metal and mixed-anion perovskites, for example $FA_{0.83}Cs_{0.17}Pb_{0.5}Sn_{0.5}(I_{0.6}Br_{0.4})_3$, are also possible and routinely used.

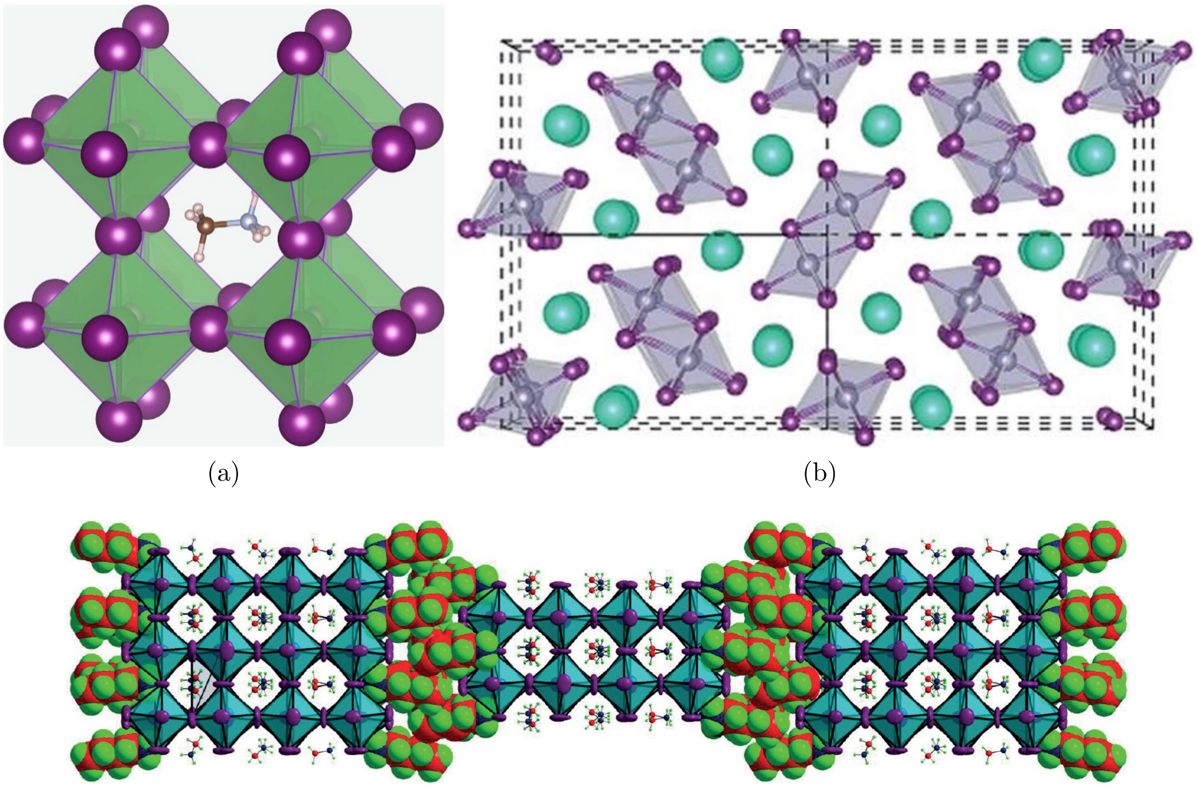

(a)

(b)

(c)

Figure 1.5: a) Methylammonium lead iodide crystal structure. From [40]. b) Crystal structure of $CsPbI_3$. From [37] c) Example of Ruddelsden-Popper perovskite structure with $BA_2MA_3Pb_4I_{13}$. From [41].

There are also the Ruddlesden-Popper perovskites, with formula $A'_2A_{n-1}B_nX_{3n+1}$. An example is $BA_2MA_3Pb_4I_{13}$ with $n = 4$, illustrated in Fig. 1.5c, where BA is butylammonium ($CH_3(CH_2)_3NH_3$). These are called 2D perovskites, because of the layered structure where a regular perovskite phase (with n layers) is sandwiched by a larger, insulating cation, BA in this case. Furthermore, there are so-called 1D phases, formed, for example, by the all-inorganic $CsPbI_3$ composition, as illustrated in Fig. 1.5b, although some authors do not refer to this phase as a perovskite [37].

Note that there is not much freedom in choosing the A cation in lead-halide perovskites. This is because the A cation must be monovalent for charge balance. Furthermore, the size of the cation dictates the Pb-X bond angle and therefore the orientation of the PbX_6 octahedra. If a given composition will result in stable tetragonal or cubic perovskites is largely dictated by the sizes of each atom composing the lattice. As a rule of thumb, one can use the tolerance factor, $t = (R_A + R_X)/(\sqrt{2}(R_B + R_X))$ where $R_{A,B,X}$ are ionic radii, to probe which compositions will lead to stable cubic or tetragonal lattices [42]. If the ionic radius of the A is too small ($t << 1$) with respect to B and X, the resulting lattice is orthorhombic, while if it is too large ($t >> 1$) the lattice is hexagonal. Experimentally, the only known tetragonal and cubic perovskites have tolerance factors between 0.8 and 1, as illustrated in Fig. 1.6, although not all compositions with t in this range result in tetragonal or cubic perovskites [43]. Only Cs, MA and FA have ionic radii in the appropriate range for PbI_6 octahedra [43]. Cs is actually too small and results in an orthorhombic lattice. FA is too big and results in an hexagonal lattice. This is why it is necessary to mix FA and Cs in mixed-cation perovskites, because otherwise the stable lattice at room temperature would not be cubic or tetragonal. MA does not have this problem. We mention that, although smaller monovalent cations (Na, K, Rb) do not form useful perovskites in the Pb-X system, it has been shown that they can be used in small quantities for surface and bulk passivation, such as in the quadruple cation perovskite RbCsFAMA [43] or in the perovskites with K surface treatment [44]. Larger cations such as BA, on the other hand, lead to Ruddelsden-Popper PKs.

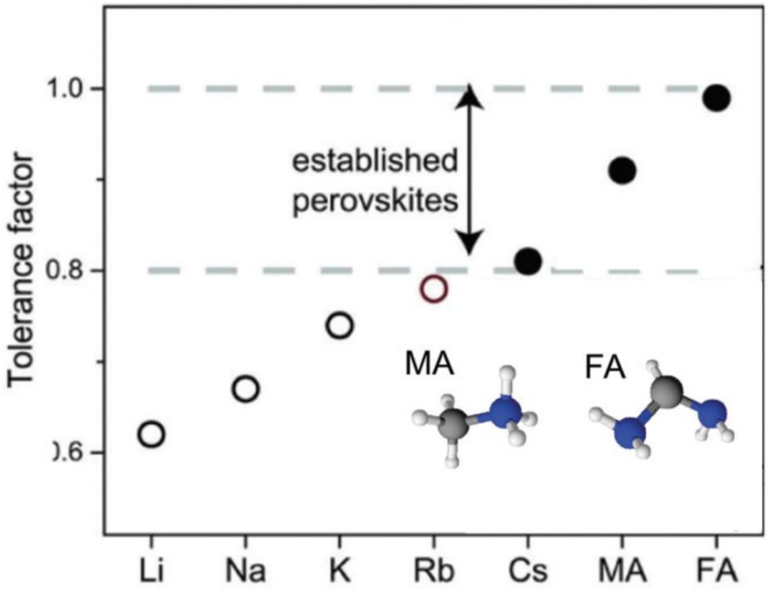

Figure 1.6: Tolerance factor for different cations (increasing in size from Li to FA) for PbI_6 octahedra. The inset shows the molecules referred to as MA and FA. All PV-relevant perovskites found so far have a tolerance factor between 0.8 and 1, although not all perovskites with tolerance factor in this range are relevant for PV, as is the case for $FAPb_3$ and $CsPbI_3$. Adapted from [43].

It is clear that many different materials can be (and are) used in the perovskite solar cell research community. It is impossible to cover in depth all these materials in a single thesis, so we will focus on the composition that has shown the most promise so far, namely those involving the mixed composition $FA_xCs_{1-x}Pb(Br_yI_{1-y})_3$.

The band structure of these perovskites has been calculated by many different groups [45–47], although there is still debate on the uncertainties of such calculations. The main technique used for band structure estimation is DFT, yielding results such as that shown in Fig. 1.7. What can be said with reasonable certainty is that hybrid organic-inorganic perovskites have direct bandgaps and the valence and conduction bandwiths are fairly large, leading to high mobilities (tens of cm^2/Vs in single crystal MALI) [45]. Another important point of the band structure shown is that the valence and conduction bands are mainly formed by Pb and I orbitals, while the organic cation orbitals sit far below the valence band. Thus, opto-electronic properties of these materials are mostly determined by the B and X atoms of the perovskite. In this view, hybrid organic-inorganic perovskites still behave as regular inorganic materials. The purpose of the organic part is only to provide structural stability. This view is somewhat misleading, however, because changing the cation does alter the bandgap because the size of A changes the Pb-X bond length and direction [45, 48]. Also, these perovskites are highly ionic materials and thus electrical conduction is caused by polarons, not free carriers, and since the A species influences the phonon spectrum, it also influences electrical transport.

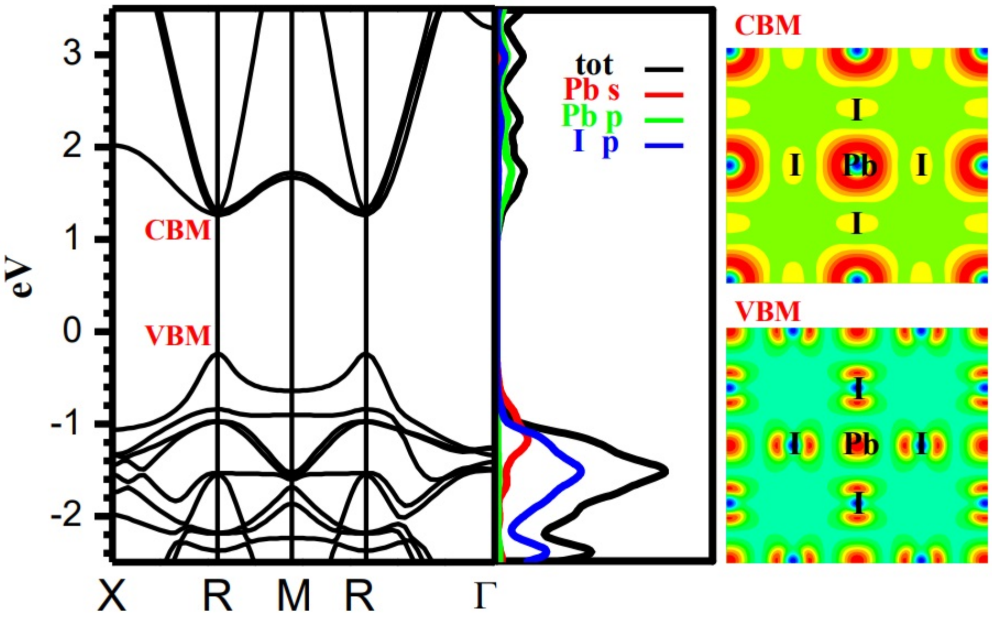

Figure 1.7: Band structure calculations for cubic MALI. From [47].

The main reason for mixing I and Br in halide perovskites is to tune the bandgap. Br is smaller than I, so the Pb-Br bond length is smaller and the bandgap is higher. Still in the early years of perovskite research it was already noticed that it is possible to alloy I and Br in any fraction desired [49], giving bandgaps ranging from 1.55 eV for pure I to 2.29 eV for pure Br, as illustrated in Fig. 1.8 for the $MAPb(I_xBr_{1-x})_3$ case. For reasons already discussed, mixing the cation also changes the bandgap [50, 51], but in a smaller range, as illustrated in Fig. 1.8d for the $FA_xCs_{1-x}Pb(I_{1-y}Br_y)_3$ alloys.

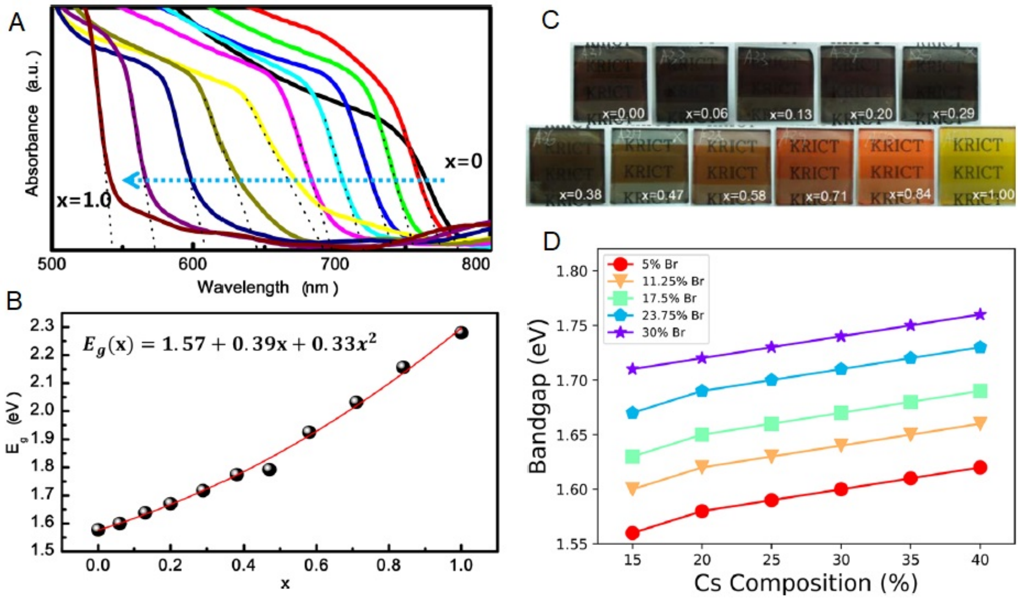

Figure 1.8: (A-C) Bandgap tuning of $\mathrm{MAPb(I_{1-x}Br_x)_3}$ alloys, showing absorption spectra and colors of layers of perovskites with different values of x, and also the bandgap as a function of x. From [49]. (D) Bandgap as a function of Cs concentration for different Br concentrations in the $\mathrm{FA_xCs_{1-x}Pb(I_{1-y}Br_y)_3}$ system. From [51].

The defect energy levels of some perovskites have also been calculated using DFT [47], as shown in Fig. 1.9 for the MALI case. Defect levels are extremely important in semiconductor devices for various reasons [52], but mainly because they 1) determine if the material will present self-doping effects, 2) influence the mobility as a result of electron-defect scattering and 3) influence recombination lifetimes as a result of the Shockley-Read-Hall (SRH) recombination mechanism [53]. In addition to the energy level of the defects, their formation energy is also important because it dictates the density (and thus relevance) of each defect at room temperature.[9] An interesting result shown in Fig. 1.9 is that, at least for MALI, most defects only generate levels close to the valence or conduction bands. This is important because only levels close to mid-gap behave as efficient recombination centers and lower lifetime. The few defects that do generate deep-levels have high formation energies and therefore are not present in significant quantities. This is currently the best explanation for the experimental observations that hybrid organic-inorganic perovskites are defect tolerant [54], meaning their defects do not completely hinder electrical conduction.

Most of the oxide perovskites (like $\mathrm{CaTiO_3}$ and $\mathrm{SrTiO_3}$) are ferroelectric. This is not the case for the halide perovskites [55]. In the beginning of perovskite solar cell research, it was believed that the high performance of these materials was possibly due to ferroelectricity [56]. Today it is known that it is due to their material properties such

---

[9] However, it is not at all uncommon for defect densities to depend on fabrication methods and conditions. Defects can be created during fabrication in states very out of equilibrium and survive metastably when cooled down to room temperature, grossly violating the formation energy rule. In perovskites these effects are exacerbated by the fact that PKs used in solar cells are usually polycrystalline, and the size and distribution of grain boundaries in the PK layer depend strongly on each specific PK layer recipe for each specific solar cell design.

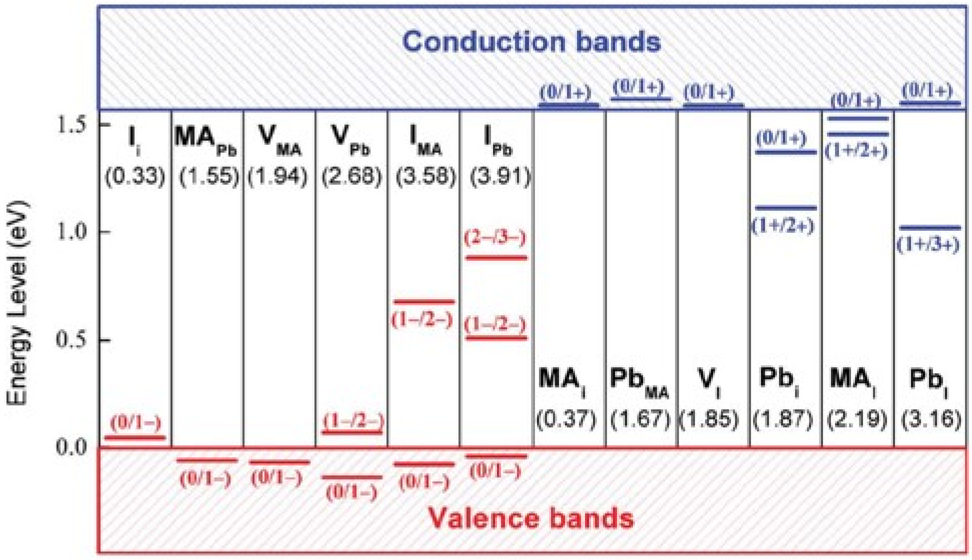

Figure 1.9: Defect energy levels of MALI calculated using DFT. Blue lines show donor levels and red lines show acceptor levels. The numbers in parenthesis show the formation energy of the corresponding defect in eV. From [47].

as high mobility and lifetime, properties which are closely linked to defect tolerance [45].

A very important feature of these materials is ionic conduction. It has been established by numerous experiments [57–60] that at least one species (probably iodine vacancies) is mobile inside halide perovskites. This is not by any means the first solid-state material to show ionic conduction (another example being AgI, once used in photographic plates), but it is the first that has been used as the absorber layer of a solar cell. It is caused by the weak bond between Pb and I. As will be discussed in the next chapter, ionic conduction influences both the stability of the perovskite layer and the performance of the device.

1.3.2 Implications to Solar Cells

There are two main advantages of these halide perovskites over Si: 1) because they have direct bandgaps, the absorption coefficient for wavelengths close to the bandgap is orders of magnitude higher than in Si [61] and 2) because they are defect tolerant, even perovskite layers with many defects result in efficient solar cells [46]. These properties mean that the absorber layer of the PK solar cell can be made much thinner than that of Si solar cells and also that it does not have to be a single crystal. Indeed, efficiencies of about as high as those of the silicon technology, higher than 20 %, have been shown [27, 34] (in the 1 cm^2 cell level) using non-epitaxial thin film deposition methods, where the absorber layer is typically 400 to 500 nm thick [62–64]. For comparison, the wafer of Si solar cells is usually 100 to 200 μm thick [27]. Therefore, PK solar cells have the potential to be more cost effective than the traditional Si technology because 1) less material is required and 2) high temperature steps such as those used in fabricating the Si ingot or in making the p-n junction by diffusion are not necessary. These are the main reasons for the excitement of the PV community over this material.

On the other hand, the main problem with the PK technology is its frequently reported instability, where the cell degrades in hours or days and its efficiency decreases to negligible values [37]. The mechanisms of degradation include ion migration under applied bias [58, 65], phase segregation under illumination [66] and reactions with moisture and oxygen when the device is not properly encapsulated [66–68]. Another non-trivial problem is the up-scaling of the technology, because the high efficiencies were only demonstrated on 1 cm^2 devices. More research is demanded in perovskite solar cells so that, if possible, a reliable commercial product is achieved. This thesis addresses the need for understanding the mechanisms behind these instabilities of perovskite solar cells.

1.3.3 Degradation of Perovskite Layers

Before discussing degradation mechanisms, one must list the conditions in which the cell will have to survive. These conditions vary with location and season where the solar panel is employed, but range from -40 °C to 85 °C in temperature, from 0 % to 100 % in relative humidity, from 0 to more than 100 mW/cm^2 in illumination, from at least ~ -1.2 V to at most ~ 1.2 V in applied voltage and from up to ~ 25 mA/cm^2 in current. It should also be mentioned that after the device is fabricated it must be encapsulated and this procedure usually requires temperatures up to 150 °C.

Leitjens et al. [37] have classified the possible degradation mechanisms in four (not unrelated) groups: structural, thermal, atmospheric and reactivity with the electrodes. In summary, these problems are related to:

1. Phase transistions of the perovskite layer [37];
2. Volatility of the organic molecule in the cation position of the perovskite (e.g. CH_3NH_3) [69];
3. Reactions with ambient moisture [68]; and
4. Reactions with adjacent layers [70].

All these mechanisms are affected by the specific composition of the perovskite. For example, $CH_3NH_3PbI_3$ is known to have a phase transition from a tetragonal to a cubic lattice at 54 °C [37]. However, only slight changes in bandgap and mobilities occur, so the solar cell maintains its high efficiency despite the phase transition and does not suffer from problem 1. On the other hand, CH_3NH_3 is very loosely bonded to the inorganic part of the perovskite, so it does suffer from problem 2 [69]. This was the problem encountered in the first PK solar cells. MA is quite acidic, so it is deprotonated easily by an iodine ion forming the gases HI and CH_3NH_2 (two of the PK precursors), which evaporate from the lattice and leave PbI_2 (the third precursor), a semiconductor with unsuitably high bandgap. In practice this is seen as a color change from black to yellow during a few days after the layer was formed. Furthermore, moisture serves as a catalyst in this reaction, so unencapsulated devices in humid ambients present even faster degradation (problem 3). A fix for these issues was found by substituting MA by FA, a heavier and less acidic cation [37]. This substitution did solve (at least partially) problems 2 and 3, but it introduced problem 1. Unfortunately, $FAPbI_3$ has an hexagonal, yellow structure at room temperature and only transitions to the cubic, black phase at 150 °C. It is possible to maintain it in the cubic phase metastably after a thermal treatment [71], but it slowly degrades back to its non-working phase during device operation, specially when heated. The reason it has an unsuitable structure turns out to be the too high ionic radius of FA, making this molecule not fit properly between octahedra of PbI_6. A fix to this new problem was then found by introducing cesium (Cs), which has a smaller ionic radius than FA. Actually, contrary to FA, Cs has a too small ionic radius, so the structure $CsPbI_3$ also does not crystallize in the tetragonal or cubic phases at room temperature [37]. However, mixing Cs and FA to form the mixed stoichiometry $FA_xCs_{1-x}PbI_3$ compound has been proven [37] to provide perovskites that have the appropriate phase at room temperature, are stable during heat and humidity tests and are able to provide high efficiency solar cells ($> 20\%$).

Problem 4 is largely caused by the reactivity of metals and halogens. Ag, for example, is a common metal used as electrode in PK solar cells [70], but it quickly reacts with I in the PK and forms the insulating material AgI. In principle the metal electrode should not be in contact with the PK; the cell structure usually has other layers in between the absorber and the metal contact and this problem should not exist. However, it turns out that many of the materials used in between the metal and the PK are permeable to both Ag and I when the device is heated or under electric fields [70, 72]. Al, Cu and even Au have the same problems, readily forming their respective iodides [37]. A solution to this problem was found by using ITO as both front and back contacts [73]. ITO is non reactive and dense, being effective in blocking moisture and oxygen diffusion into the PK and the volatile components of the PK out of it.[10] Another solution was the use of carbon as electrode, but the efficiency was modest [74].

A peculiar phase transition of mixed halide perovskites, particularly $MAPb(I_xBr_{1-x})_3$, can be triggered by light [59, 75–81]. This was found in 2015 by Hoke et al [75]. The mechanisms causing this instability are still under debate [78, 79, 81], but the effect is that the mixed-state of the I/Br alloy is only stable up to a certain concentration of free carriers inside the perovskite. Above this critical concentration, the PK segregates into Br-rich and I-rich nuclei, as illustrated in Fig. 1.10. This effect was first evidenced by a shift in the bandgap peak in photoluminescence (PL), as shown in Fig. 1.10b. After a few seconds or minutes of exposure to the PL laser, the bandgap of the mixed-halide perovskite was suppressed and a new peak corresponding to the $MAPb(I_{0.8}Br_{0.2})_3$ composition grew [75]. The effect apparently indicates that for the MALIBr system there is a critical Br concentration of 0.2 above which the perovskite is unstable for high free carrier densities. The authors also found that the transition is reversible; in the dark, the mixed phase of the perovskite reforms in a few minutes [77]. The phenomenon has been called light-induced phase segregation, but it can also be triggered by injecting carriers with an electric current [80], although in this case is not clear if the effect is still reversible [72]. Even though in the case of light-induced segregation the effect is reversible, this instability has important implications for solar cells that make use of high bandgap perovskites. For example, the ideal PK bandgap for a Si/PK tandem solar cell (which will be discussed

---

[10] However, as we will show in the Results chapter, even ITO blocking layers can be permeable to ions depending on the applied electric field (in particular, in reverse bias conditions). It is believed that the permeability of ITO is a result of the grain boundaries in the layer, which might be weak regions where ions can leak from one layer to another. In this case, it might be possible to solve this problem by making the ITO completely amorphous, but this will affect device performance.

in more detail later on) would be about 1.7 eV, corresponding to a Br concentration of 0.25, but this concentration gives unstable perovskites. Once the cell is illuminated, Br-deficient regions appear. These regions have lower bandgap than their surroundings and act like traps for the generated carriers, giving lower performance cells. This is why most Si/PK tandems have so far used non-ideal PK bandgaps such as 1.63 eV, corresponding to a Br concentration of 0.17. Fortunately, it has been shown that it is possible to change the onset of this instability by changing the PK's composition. Recently, Xu et al. [82] have shown that the Cl-containing perovskite family has appropriate bandgaps for tandems and much higher carrier concentration onsets for phase segregation. In particular, they showed that the composition $(\mathrm{Cs_{0.25}FA_{0.75}Pb(I_{0.85}Br_{0.15})_3})_{0.95}(\mathrm{MAPbCl_3})_{0.05}$ has a bandgap of 1.67 eV and is stable against phase segregation even when illuminated with up to 100 suns in intensity, which is well above the levels that the cell will experience during operation. Tandem efficiency was also very high: 27.3 %.

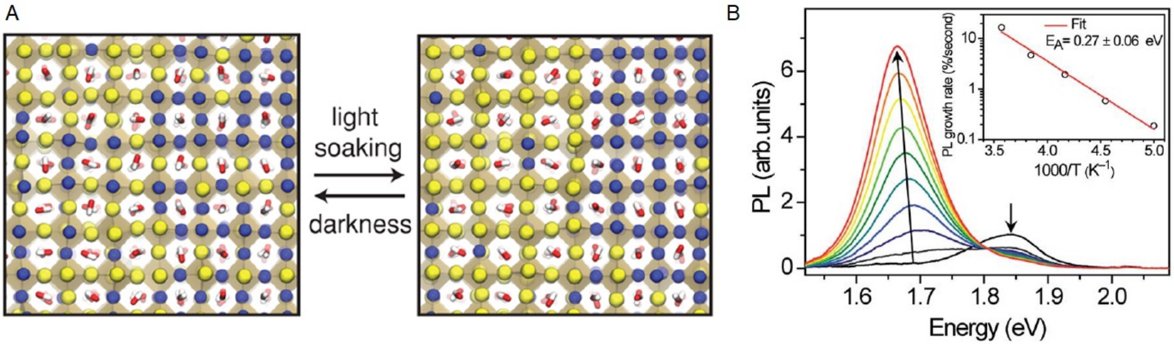

Figure 1.10: Phase segregation of $\mathrm{MAPb(I_{1-x}Br_x)_3}$ during carrier injection with light. A) Illustration of Br clustering (I is yellow and Br is blue). From [78]. B) Bandgap shifts observed while the layer is illuminated with the PL laser. From [75].

It should be noted that these instability problems are all related to the mobile ions present during operation. The weak bond between the cation or the metal with the halogen means that halogen ions can readily move under a driving force such as bias or light. Under this driving force, they may reach an adjacent layer and react irreversibly with ions from this layer, or they may cluster and form regions with different bandgaps. Unfortunately, mobile ions seem to be an intrinsic property of hybrid organic-inorganic perovskites and no clear way of eliminating them has been found. Therefore, the route to stability seems to be applying barrier layers in between the PK and the remaining layers. Ideally these barriers would be the active layers of the cell themselves, but it is hard to find materials that have the right transport properties, can be deposited with scalable techniques and additionally provide barriers for halides.

So far, the most stable cell design that has been found employs $(\mathrm{FAPbI_3})_{0.83}(\mathrm{CsPbBr_3})_{0.17}$ as the absorber layer and ITO electrodes on both sides [37], giving efficiencies of about 15 % in single junction and up to 28 % in tandem with heterojunction Si cells. When encapsulated, these cells can survive for more than 1000 hours when tested for temperature and humidity resilience in damp heat tests.

Another problem is that solar cells can be reverse biased in the field. This happens if the solar module is partially shaded so that some cells produce more current than others. Since the cells are usually all connected in series, this means that the illuminated cells try to drive the shaded cells with a current higher than they can produce, meaning the shaded cells are driven into reverse bias, as illustrated in Fig. 1.11. In reverse bias, the cells dissipate power instead of producing it, but more problematic is the fact that usually this power is dissipated in local shunts because in reverse bias the active regions are non-conducting. This means that a lot of power can be dissipated in a small region, leading to high temperatures that damage the cell and encapsulation, even to the point of melting the contacts [83–86]. In perovskites, it has been shown [72, 87] that many other mechanisms of degradation are present under reverse bias, such as electrochemical reactions between the PK and the adjacent layers, current-induced phase segregation and metal migration from the contacts, which shunt the device. These mechanisms will be discussed further in the Results chapter. Unfortunately, as of January 2021, no clear solution to these problems has been found, although there are methods to alleviate them at the module level [88] by e.g. using bypass diodes or changing the cell interconnection scheme.[11]

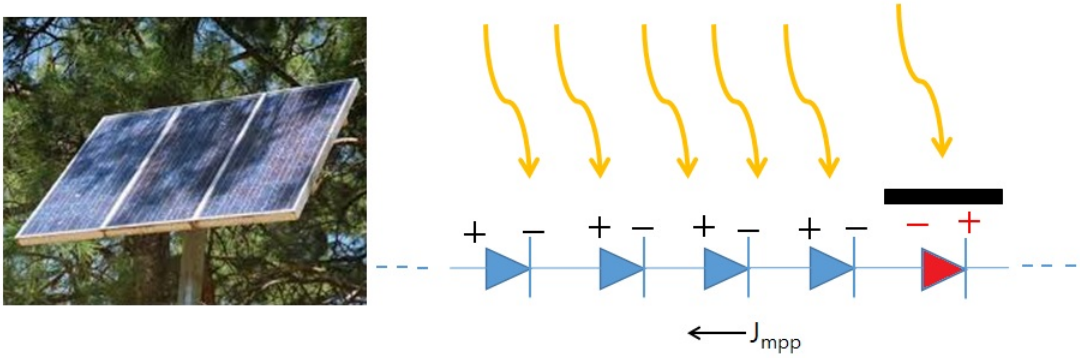

Figure 1.11: Illustration of the reverse bias problem that happens when a module is partially shaded (by, for example, a nearby tree). The shaded cell (in red) is being driven by the illuminated cells into reverse bias. Adapted from [86].

1.3.4 Brief History of Perovskite Solar Cell Development

Perovskite solar cells were born from yet another solar cell concept, that of dye-sensitized solar cells (DSSC) [36]. In this approach, a dye is deposited on a porous layer (usually TiO_2) which is itself deposited on a conducting transparent substrate (usually glass coated by fluorine-doped SnO_2 (FTO)) and the whole structure is immersed in an electrolyte. The dye absorbs the light and the excitons generated are separated in electrons that go into the TiO_2 and holes that go into the electrolyte. In 2006 the PK $MAPbBr_3$ was first used in the form of quantum dots as the dye in a DSSC by the group of Miyasaka in Japan, with cell efficiencies of about 2.2 % [36]. Organic-inorganic perovskites had actually been synthesized by Weber in 1978 [36] and later used by Mitzi at IBM in the

---

[11] CdTe solar modules, another thin-film solar technology which is already in the market, also present reverse bias problems and no clear solution has been found so far. The suppliers simply alert the clients to have extreme care not to let the module be partially shaded during operation. Si solar cells also have reverse bias problems, but in this case the cells are much more resilient (Si solar cells can survive up to tens of volts in reverse bias depending on the technology), so that it is possible to avoid the problem with bypass diodes.

1990's [42] to test its applicability in transistors and LEDs, but the subsequent use in photovoltaics was not pursued by Mitzi because of the low stabilities observed [36, 42]. The first journal publication appeared in 2009 from Miyasaka's group, reporting on a DSSC 3.8% efficient using $CH_3NH_3PbI_3$ or $CH_3NH_3PbBr_3$ [89]. The cell was reported to present stabilities on the order of minutes.

A major leap was the substitution of the liquid electrolyte by the solid-state hole transporting material N^2,N^2,$N^{2'}$,$N^{2'}$,N^7,N^7,$N^{7'}$,$N^{7'}$-octakis(4-methoxyphenyl)-9,9'-spirobi[9H-fluorene]-2,2',7,7'-tetramine, also known as spiro-OMeTAD, in 2011, which was independently reported by joint publications by the Graetzel and Park groups [90], from Switzerland and Korea, and by the Snaith and Murakami groups [91], from England and Japan. Both publications reported "excellent longterm stabilities", with the latter paper showing a 10.9 % efficient device which passed a 1000 hours stability test under simulated sunlight. In this same study, Lee et al. [91] made the perhaps even more important discovery that substituting the material of the mesoporous layer from TiO_2 to the insulator Al_2O_3 showed no device performance decrease (in fact, the cell efficiency increased by a few percent). This immediately suggested that the TiO_2 was not needed to break excitons inside the PK, as was previously believed. It was then shown that the PK behaved as an ambipolar semicondutor and that, in this material, light generates free electrons and holes with separate quasi-Fermi levels instead of excitons. Simple planar devices, without any mesoporous layer, were demonstrated in the same paper (although with considerably less efficiency). The solar cell concept was no longer the same as that in DSSCs [92, 93].

By 2013, efficiencies higher than 15 % started to be reported. In particular, Graetzel's group [94] reported on a 2-step method of depositing the PK, where first the PbI_2 is deposited by spin-coating on the TiO_2 mesoporous layer and then the structure is immersed in a methylammonium iodide solution. Using this method the authors reported a higher control of the PK crystallization, providing better layer morphologies and consequently improved efficiency (about 15 %). Snaith's group [95] also reported on a different strategy for depositing the PK, namely evaporation, and achieved higher than 15 % efficiencies. By the end of 2014, Seok's group from Korea managed to further improve PK morphology by careful solvent engineering [96], reporting 16.2 % efficient solar cells. It was also realized that by using perovskites with mixed halogens and mixed cations, namely $MA_xFA_{1-x}Pb(I_yBr_{1-y})_3$, the PK bandgap could be engineered and the device stability improved. FA is slightly larger than methylammonium, giving larger bond lengths for Pb-I and resulting in a lower bandgap PK that better matches the solar spectrum. This fact permitted Seok's group to achieve the first perovskite solar cell with 20 % efficiency [62] by mid-2015. This same group currently holds the record efficiency of 25.2 % [34] for single junction PK solar cells, although the details of how to reach this efficiency have not been published yet.

Although the jump from 2 % to 20 % in less than 10 years is remarkable, it must be noted that the devices that reach the top efficiencies have very poor stabilities, of a few months at best [36, 37]. Some degrade during the measurement of efficiency itself. It is clear that to reach commercialization this problem must be solved and, indeed, it seems that most of the current (2018-2020) research is addressed to improving stability rather than to improving efficiency [36, 37, 97]. However, this problem was recognized from the start and, by now, some of the degradation mechanisms have been understood. In fact, various groups are now reporting PK cells that are able to pass standard stability tests provided by the International Electrotechnical Commission (IEC) and still retain considerable efficiency [63, 98, 99].

1.4 Concepts of Tandem Solar Cells

In discussing the SQ limit, we concluded that there is little room for further increasing solar cell efficiency because of inherent limits of absorbing light with a semiconductor. The limit is associated to the fact that a semiconductor only absorbs photons of energy higher than a threshold (the bandgap) and that it is only able to convert a bandgap's worth of energy for the photons that it does absorb. This conclusion is correct, but only as long as we restrict ourselves to using a single semiconductor.

Indeed, stacking solar cells that use semiconductors of different bandgaps is a demonstrated method of going beyond the SQ limit [100]. These stacked solar cells are called tandems. The idea is to put a cell with higher bandgap on top of a cell with lower bandgap, as illustrated in Fig. 1.12, because if the photons of higher energy are absorbed by higher bandgaps, less energy is lost as thermalization of hot carriers. In the same way that Shockley and Queisser calculated the limit for single-junction solar cells, one can calculate the limits for multiple junctions. This has been done by several authors in the 1980's [31]. The result for double-junctions is that the maximum efficiency is 47 % for 0.96 eV and 1.63 eV bandgaps [101]. This is a substantially larger efficiency than the single junction limits; solar panels with 40 % efficiency produce double the power of those with 20 % efficiency. Indeed, solar cells with efficiency higher than 40 % have been demonstrated [34], the current record being 47.1 % (under 143 Suns concentration) with a 6-junctions solar cell that uses InAlGaAsP-based materials for bandgap tuning [102]. However, no scalable method is known to produce reliable layers of these materials, so the market still relies on c-Si. Nevertheless, given the market pressure for high efficiency, it would be revolutionizing to find a material that can be partnered with Si to make tandems. This is not easy because this material must be constrained to have a bandgap in the appropriate range, have high mobilities and lifetimes, be composed of abundant precursors and allow for scalable deposition methods. As it turns out, halide perovskites are the first materials found to fit all these requirements.

In fact, soon after the birth of PK solar cells it was already noticed that these cells could be well matched partners to silicon because of their controllable bandgap [103]. For a two bandgaps solar cell, the best match to the silicon 1.1 eV would be a top cell using a bandgap of 1.7 eV, resulting in a theoretical maximum efficiency of 42% [104]. This is also a much easier way for the new technology to enter the market, as it would take advantage of the already cost effective Si technology and could be seen as an efficiency booster. Indeed, Si/PK tandems have already been demonstrated, with a record of 29.1 %, and show great promise for commercialization [34]. The company Oxford PV leads the market of this technology with its pilot production plant in Germany [105]. Even triple junctions, Si/perovskite(mid-bandgap)/perovskite(high-bandgap) have already been demonstrated [106], although efficiency was only 13.2 % because of a low fill factor.

Currently, the most promising way to commercialize PK solar cell technology seems to be partnering it with Si in tandems. This thesis will thus focus on PK solar cell architectures that can be applied in tandem with Si. This severely constraints the possible

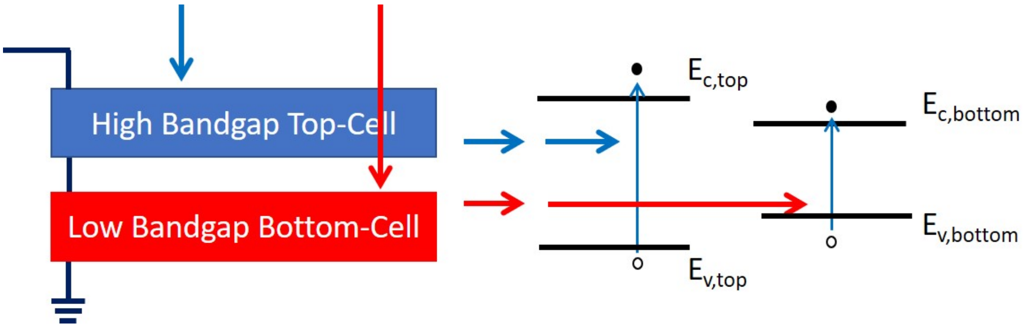

Figure 1.12: The tandem solar cell concept. Two solar cells using absorbers with different bandgaps are stacked so that the top cell, which has a higher bandgap, absorbs higher energy photons, while the bottom cell, having a lower bandgap, absorbs the lower energy photons. Usually the two cells are fabricated monolithically (i.e., in a single device) and connected in series. The concept also allows for more than two cells to be stacked. Increasing the number of bandgaps allows for better usage of the solar spectrum.

materials that can be used, because the Si bottom cell has a textured surface to reduce reflectance, as illustrated in Fig. 1.13. Only materials that can be deposited by evaporation, sputtering, CVD or ALD can be used because the layers of the top perovskite solar cell must be conformal to the pyramids of the bottom cell. The fact that this is even possible has already been demonstrated by Sahli et al. [107], resulting in a 25.2 % efficient solar cell.

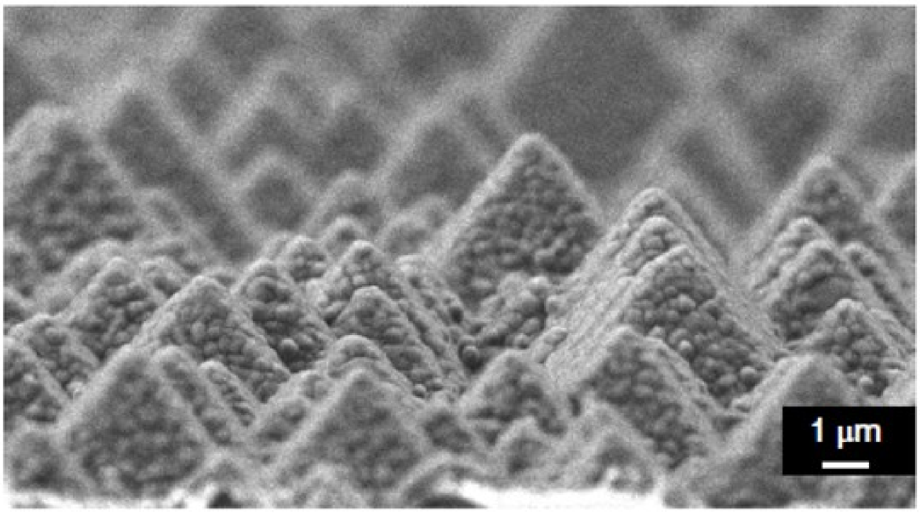

Figure 1.13: Scanning electron microscope image of a Si/PK tandem solar cell fabricated on a textured surface. The Si surface is covered by the perovskite grains; it would be highly smooth otherwise. From [107].

Concerning their history, Si/PK monolithic tandems also developed rapidly [103]. In 2014 it was shown that perovskites have a very steep absorption edge and low sub-bandgap absorption [61], which are essential properties for a top subcell in a tandem device. Device modeling and simulations were also published providing guidelines for reaching efficiencies higher than 30% [108]. The major initial challenge was parasitic absorption in the carrier selective layers and in the transparent electrodes [109] and the necessity of substituting the opaque rear metal used in single junction perovskite cells by a transparent recombination layer or tunnel junction. The first experimental report of a monolithic Si/PK tandem solar cell was in March of 2015 [110] by a joint publication from the Buonassissi (from MIT) and McGehee (from Stanford) groups, with an efficiency of 13.7 % using a polished, diffused-junction Si bottom-cell and a MALI top-cell with mesoporous TiO_2 and spiro-OMeTAD. A Si tunnel junction was used to connect the two subcells and the transparent top contact was of Ag nanowires. The efficiency was being reduced primarily by parasitic absorption from the charge transport layers [110]. Changing the TiO_2 to SnO_2, the top contact to sputtered ITO (indium tin oxide) and using a more efficient Si heterojunction bottom cell, Albrecht et al. [111] demonstrated 18.1 % efficiency in October of 2015. In February 2016, Werner et al. [112] reported 21.2 % efficiency using a C_{60} electron selective layer and IZO (indium zinc oxide) as a recombination layer to connect the two subcells. In these reports, one of the main problems was the use of polished surfaces, which were necessary for depositing the perovskite top-cell. In February 2017, Bush et al. [113] used a rear-side textured silicon bottom-cell to improve infrared light trapping and achieved 23.6 % efficiency, but the front surface was still polished in order to deposit the PK top-cell. In this case a mixed formamidinium-Cs perovskite was used because it was proved earlier [114] that this composition provides much better stabilities. Indeed, the device passed damp heat tests [113]. In June 2018, Sahli et al. [99] demonstrated the first fully textured Si/PK tandem solar cell, providing improved light trapping and achieving an efficiency of 25.2%, the current record for this architecture. The devices also presented an encouraging stability, having retained at least 90 % of its initial efficiency after 1000-hours of a damp heat test at 85 °C and relative humidity of 85 % and also after 270 hours of a light soaking degradation test, where the cell is held in constant illumination at the maximum power point [99].

1.5 Objectives

There is no doubt that for perovskite solar cells to become commercial it is necessary to solve stability problems. Unfortunately, these problems have proven themselves to be formidable, and it has become clear that a deep analysis of the physics and chemistry governing the mechanisms of degradation is necessary before we can find solutions. Therefore, we set as the main objective of this thesis to provide detailed mechanisms for the degradation of perovskite solar cells. We will focus on one particular mechanism that we think has been underappreciated by the community, even though it is fundamental for the technology to be reliable in the field: the stability of perovskite solar cells under reverse bias.

Unfortunately, as of January-2021, perovskite solar cell research is not very common in Brazil yet, even though the technology holds great potential for the future. Therefore, another important goal of this thesis is to give a comprehensive introduction to perovskite solar cells to any future student that might want to take this work further.

Chapter 2

Device Physics

The classical view of solar cell operation is described in textbooks such as that by Green [115] and Luque & Hegedus [31] (see also the last chapter of Sze [116]). In essence, these books describe the p-n junction operation when the device is under sunlight. The description is as follows. A semiconductor containing a p-n junction is exposed to sunlight, creating free[1] electrons and holes that eventually reach the depletion zone at the p-n interface because of their thermal motion, unless they recombine first. The electric field in the depletion zone sends electrons (which are negative) one way and holes (which are positive) another, effectively separating the opposite charges to create the voltage and current applied in the external circuit.

This description is correct, but somewhat restrictive. It is not necessary to have a p-n junction for a solar cell to produce work [5, 117]. All that is needed is some mechanism that preferentially sends electrons and holes in different directions, acting like selective membranes. In perovskite solar cells, the membranes are not p-n junctions but heterojunctions. The idea is to sandwich an absorber material (the perovskite) within a layer that is a good conductor of electrons but not of holes and another layer that is a good conductor of holes but not electrons, as illustrated in Fig. 2.1a. These layers are called the electron transport layer (ETL) and hole transport layer (HTL). None of these layers is necessarily doped, although they usually are because of intrinsic defects that slightly change their stoichiometry or because of intentional doping for improving conductivity and reducing series resistance. The electron (hole) selection effect at the interface between ETL (HTL) and PK occurs simply because the ETL has a higher electron (hole) conductivity than a hole (electron) conductivity, either because of a higher electron (hole) mobility or because of a higher free electron (hole) concentration. Both ETL and HTL are then contacted by their respective conductive contact, usually one being a transparent conductive oxide (TCO) such as ITO or FTO[2] and the other being a metal such as Ag or Au. Examples of ETLs are TiO_2, SnO_2, PEDOT:PSS and C_{60} and of HTLs are NiO, CuSCN, spiro-OMeTAD and poly(triaryl amine) (PTAA).

Note how the principle of operation of perovskite solar cells does not require any of its

---

[1] By free it is meant that the electrons and holes are in the bottom or top of their respective bands, where conduction is appropriately described with an effective mass.

[2] FTO (SnO_2:F) is another type of TCO, like ITO (In_2O_3:SnO_2). These materials are very highly doped semiconductors, usually to the point of degeneracy, giving decent conductivity (although not as high as regular metals) but also transparency, since they still have a band gap of a few electron volts.

layers to be doped. Nevertheless, there is still a junction between materials of different carrier concentrations because in general each layer of the cell has a different workfunction. In this sense the perovskite solar cell can be described in the same way of a p-i-n silicon solar cell, where the HTL plays the role of the p-type layer, the perovskite is the intrinsic layer and the ETL is the n-type layer. However, we mention that, in principle, it is not even necessary to have a junction between materials of different carrier concentrations to have a working solar cell, be it a homojunction or heterojunction. In Ref. [117] it is shown how a hypothetical stack of layers having different mobilities for electrons and holes, while at the same time having constant free carrier concentrations throughout all the layers, can act like a photovoltaic cell and even have high efficiency. Note that in such a mobility-junction solar cell there is no built-in electric field, and yet it is still possible in principle for such a cell to approach the SQ limit in efficiency. Nevertheless, all efficient solar cells fabricated to date have built-in electric fields, perovskite solar cells included.

There are advantages and disadvantages on heterojunction devices compared to homojunction devices. The main advantage is that, since the materials are different, they possibly have different energy levels for valence and conduction bands, as is the case in Fig. 2.1b. A misalignment in the valence (conduction) band between ETL (HTL) and absorber can behave as an energy barrier for holes (electrons), increasing membrane-selectivity and therefore cell performance. The main disadvantage is that the interfaces of heterostructures usually have a high concentration of defects that significantly increase non-radiative recombination, lowering cell performance [116]. Also, the energy alignment problem between two materials is still a highly debated subject [118] and, in the vast majority of cases, the simple electron affinity/ionization potential rule for conduction/valence band alignment gives grossly incorrect values when tested experimentally. This severely complicates analyses and simulations of heterojunction devices.

The purpose of this chapter is to provide a more in depth description of device operation.

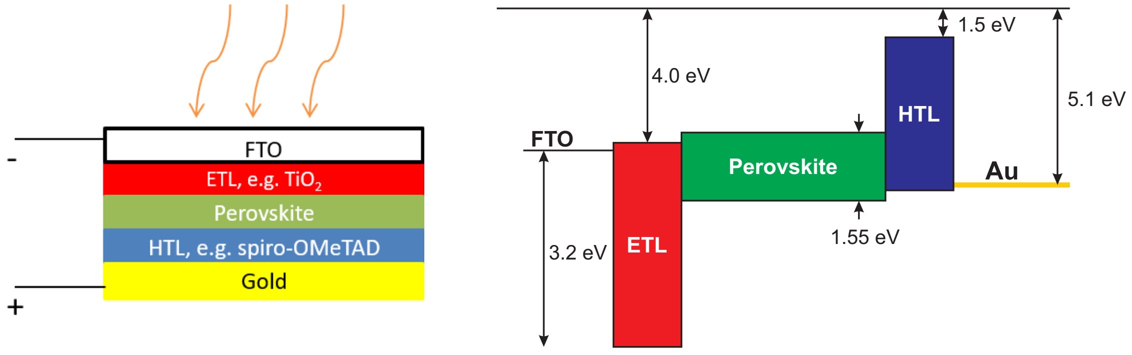

(a) (b)

Figure 2.1: a) Common layered structure of perovskite solar cells. b) Band diagram before equilibrium when the ETL is TiO_2 and the HTL is spiro-OMeTAD.

2.1 Qualitative Description

Before equilibrium is reached, each layer has its own Fermi level and the band diagram for the stack is as shown in Fig. 2.1b. To minimize the energy of the system, electrons are transferred between layers until the Fermi level of the whole system becomes the same, reaching equilibrium. The band structure becomes that of Fig. 2.2a, with depletion regions occurring at the interfaces between layers. Note that for the case where the absorber layer is intrinsic and there are no mobile ions (i.e., there are no net charges inside the layer) the depletion region would extend throughout the entire layer and contain a constant electric field, a result that follows directly from Gauss' law.

When light is applied, the system is brought out of equilibrium and, in principle, the concept of chemical potential (i.e. Fermi level) loses meaning[3]. However, we make the common assumption that the electron and hole gases are each in a separate equilibrium described by quasi-Fermi levels [31,116]. This assumption is justified as follows. Suppose electrons can jump between levels of the conduction band very easily. This is a good approximation because electrons can absorb and emit phonons, which are very numerous and in the right range of energies (tens to hundreds of meV), in order to jump between levels of the same band. This means these levels will share a common chemical potential. The same is true for holes in the valence band. Experimentally, the relaxation time (i.e. the time it takes for a given non-equilibrium distribution to relax to an equilibrium distribution described with a chemical potential) is of order of picoseconds, which is far too short in comparison with the regular time scales involved in transport of electrons and holes in semiconductor devices, including perovskite solar cells.[4] Therefore, it is justified to use a single chemical potential for levels in the same band.

On the other hand, this justification breaks down for levels in different bands, because the bandgap is too large (a few eV) for phonon interactions. Only by emitting photons can the two bands interact. The associated time scales are then of order ~ 100 ns in direct-bandgap semiconductors [116] such as perovskites. These larger time scales are within range of the time scales involved in extraction of electrons and holes created inside the absorber of the solar cell. To see this, one can calculate the associated length scale relevant to electron/hole transport by using the mobility. In perovskites, the mobility is of order $\mu \sim 10$ cm^2/Vs [45,119] and the fields applied are of order $\sim 10^4$ V/cm, so a carrier can drift within such a field before recombining for $\sim 10 \times 10^4 \times 10^{-7} = 10^{-2}$ cm $= 100$ μm. For diffusion transport, the length scale is $\sqrt{kT/q \times \mu \times \tau} \sim \sqrt{0.026 \times 10 \times 10^{-7}} \sim 1.6$ μm at 300 K. Both length scales are higher than the thickness of the perovskite layer (~ 0.5 μm). Therefore, electrons and holes can be extracted from the perovskite before they reach chemical equilibrium with each other and it is necessary to use separate chemical potentials for each gas. The two gases will only be in chemical equilibrium with each other inside the semiconductor if no light and no voltage are applied[5], in which case they

---

[3] We make no distinction between chemical potential and Fermi level because to a good approximation they have the same value. Remember that chemical potential is the energy added to the system when a particle is added, and Fermi level is the energy that (relevant) electrons have in the solid. To a good approximation, adding only one electron to the system does not change the Fermi level, so the electron's energy would be that of the Fermi level.

[4] Thermalization of hot carriers is an example of a relaxation process.

[5] But they will have the same temperature even though they are not in equilibrium with each other, because both gases are in the same thermal bath of phonons.

will share the same chemical potential and the situation in Fig. 2.2a will result.

Having two gases at different chemical potentials, one can generate work at the external load by extracting each gas at separate contacts, which is done with the ETL and HTL membranes. The voltage that the cell produces will be the difference between the Fermi levels of each contact, which are set by the quasi-Fermi levels of the PK. If the rate of transfer of electrons (holes) from the PK to the ETL (HTL) and from the ETL (HTL) to its contact is much higher than the rate of recombination with holes (electrons), the electron (hole) chemical potential at the ETL's (HTL's) metal contact will be equal to that in the PK and there will be minimum voltage loss.

If one joins the two contacts in short-circuit, the Fermi levels of the contacts become the same. There is a current, J_{sc}, flowing through the wire that connects the terminals because it is faster for photoelectrons to recombine with photoholes via the external wire than via direct recombination inside the PK. Thus, this current consists of all electrons and holes that were generated by light and did not recombine before being extracted by the terminals. The band diagram is that in Fig. 2.2c. If, on the other hand, the terminals are left unconnected, the quasi-Fermi levels reach their maximum separation (assuming no external voltage is applied), no current flows and the solar cell produces its maximum photovoltage $V_{oc} = \phi_p - \phi_n$, where $\phi_{p,n}$ are the quasi-Fermi levels of holes and electrons inside the PK. Note that this condition does not necessarily mean that the bands are flat, only that the quasi-Fermi levels are flat, since current is the gradient in quasi-Fermi level. If, instead of zero or infinite, an intermediate resistance is attached as load, the band diagram is somewhere in between the two previous cases. There is a particular resistance that maximizes the power $P = I \times V$ drawn from the solar cell, where $I = JA$ and A is the cell area. The point of the J-V curve corresponding to this current and voltage is called the maximum power point. An external circuit is used to control the load resistance seen by the cell and maintain the device at its maximum power point.

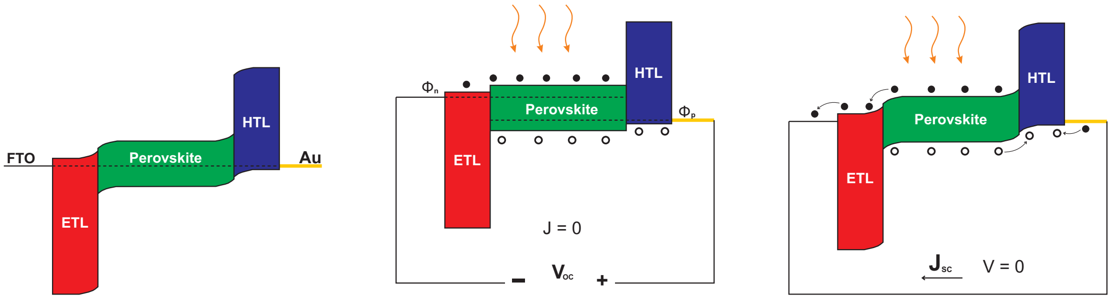

(a) (b) (c)

Figure 2.2: a) Band diagram for the structure in Fig. 2.1 after thermal equilibrium is reached. b) Band diagram with light at V_{oc}. c) Band diagram with light at J_{sc}.

To calculate the J-V behavior, one must find the distributions of electric potential and of electron and hole concentrations throughout the device. Standard textbooks on semiconductor device physics [116] show how to solve this problem analytically in the case of a p-n homojunction, obtaining the Shockley diode equation:

$$J = J_0(\exp(qV/nkT) - 1) - J_L \tag{2.1}$$

where J is current density, J_0 is a saturation current density, q is the proton charge, V

is voltage, n is the ideality factor, k is Boltzmann's constant, T is temperature and J_L is the current density generated by light.

In perovskite solar cells, the problem is much more complicated for two reasons: 1) mobile ions play an important role [120–122] and 2) a universal rule to align bands in heterojunctions is not known [118]. Nevertheless, important insight can be obtained by numerically solving the Poisson and continuity equations, the solution of which can be compared to experiments. We will now briefly outline this approach.

2.2 Quantitative Description

The electric potential, V, electron concentration, n, and hole concentration, p, throughout the perovskite layer are obtained by solving the steady state versions of the Poisson equation

$$-\partial_x^2 V(x) = \frac{q}{\epsilon}\left(p(x) - n(x) + N_{ions}(x)\right) \tag{2.2}$$

and continuity equations:

$$\frac{1}{q}\partial_x J_n(x) - R(x) + G(x) = 0 \tag{2.3a}$$

$$-\frac{1}{q}\partial_x J_p(x) - R(x) + G(x) = 0 \tag{2.3b}$$

where q is the proton charge, ϵ is the perovskite dielectric constant, N_{ions} is the concentrations of ionic charges (from ionized donors and acceptors and from mobile ions) at depth x, J_n and J_p are electron and hole current densities and R and G are the recombination and generation rates per unit volume.

Note that in writing these semiconductor equations for the perovskite layer we are already making some questionable assumptions. First, we are using 1D equations to describe a 3D device. This is only strictly permissible as long as no mesoporous layer is used, films are sufficiently uniform and the contacts cover the entire area of the cell. Second, we are assuming it is possible to treat any polarization of the perovskite lattice by an appropriate dielectric constant[6]. This treatment is at least doubtful, if not impossible, when the material is ferroelectric, which is the case for some oxide perovskites. We are assuming, therefore, that the PK under consideration is not ferroelectric, a fair assumption for halide perovskites [55]. Third, it is implicitly assumed in these equations that light generates free electrons and holes, not excitons. This is a valid assumption because the binding energy of excitons in perovskites has been measured to be at most of the same order of the thermal energy at room temperature [123]. Therefore, if the absorption of a photon leads to an exciton it is quickly dissociated and free electrons and holes are created in their respective gases in quasi-equilibrium.

To solve Eqs. (2.2) and (2.3), it is necessary to build models for the current densities, ionic density and recombination and generation rates in terms of the unknowns (V, n and

---

[6] This dielectric constant takes into account the polarization of the charges in the material that have bounded motion. The mobile ions, electrons and holes also screen electric fields, but this screening is being taking into account by solving the Poisson equation. Including it again in the dielectric constant would be double counting. Also note that it is extremely hard to determine experimentally what this dielectric constant would be. It is usually taken as a phenomenological parameter when fitting experimental curves.

p) and some model parameters. We will now consider each of these models, highlighting their subtleties when applied to PK solar cells.

For the current densities, the usual model is the same as that of silicon solar cells, namely drift and diffusion [124]:

$$J_n = q\mu_n \left(-n\partial_x V + \frac{kT}{q}\partial_x n\right) \tag{2.4a}$$

$$J_p = q\mu_p \left(-p\partial_x V - \frac{kT}{q}\partial_x p\right) \tag{2.4b}$$

where $\mu_{n,p}$ are the mobilities of electrons and holes. The drift-diffusion equations can in fact be derived from the more general Boltzmann transport equation [125], which also provides correction terms to this model. However, this would give more precision than experiments would be able to verify, so these corrections will not be considered further.

For the recombination rate, one usually includes two mechanisms: radiative and defect recombination. Radiative recombination is the counterpart of generation by light and is linear in both the electron and hole densities [116]. Defect recombination (also known as Shockley-Read-Hall (SRH) recombination [53]) depends on the concentration and distribution, both in real and energy spaces, of defects in the perovskite. It is common to make the approximation that there is only one type of defect which produces an energy level at midgap. This is justified because midgap levels are the most efficient recombination centers, since for a trap level to assist in a recombination event it must be efficient in capturing both holes and electrons, but trap levels that are too close to the conduction (valence) band have low probability of being occupied by holes (electrons). Under the further simplifying condition that the capture cross sections of holes and electrons by the defect are equal, the complete equation for R becomes [31]:

$$R = B(np - n_i^2) + \sigma v_{th} N_t \frac{np - n_i^2}{n + p + 2n_i} \tag{2.5}$$

where B is a constant that determines the probability for a radiative recombination event, σ is a capture cross section for a defect recombination event, v_{th} is the thermal velocity of electrons and holes ($\approx 10^7$ cm/s), N_t is the concentration of midgap traps and n_i is the intrinsic carrier density of PK. Note that we have ignored Auger recombination, which is justified because it is much more improbable than either of the other two mechanisms when the semiconductor has a direct bandgap, which is the case for PK. It cannot be ignored, however, in silicon cells having a substrate with low defect density [126]. In materials that are at least moderately doped and are in low injection conditions, Eq. (2.5) can be further simplified, because, if for example the material is p-type, $p_0 >> n_0$, where p_0 and n_0 are the equilibrium concentrations. In low injection, we also have that p is negligibly changed from its equilibrium value. Now, since $n_i^2 = n_0 p_0$, Eq. (2.5) becomes

$$R = \frac{n - n_0}{\tau} \tag{2.6}$$

where $\tau = (Bp_0 + \sigma v_{th} N_t)^{-1}$ is an effective lifetime that takes into account both radiative and defect recombination rates. For high injection, we have that $n \approx p >> n_i$ and Eq. (2.5) can be simplified to

$$R = Bnp + \sigma v_{th} N_t \frac{np}{n + p} \approx Bn^2 \tag{2.7}$$

The second term has been ignored because it is linear in n while the first is quadratic. Note that in a lifetime versus light intensity measurement one observes a change from linear to quadratic dependence once high injection is reached. For even higher injections, Auger recombination would become dominant and the dependence would become cubic, but in perovskites these injection levels are not of concern [52].

The generation rate is given by the light absorption profile throughout the perovskite. This can be very intricate, given that the perovskite solar cell is a stack of thin films and it is necessary to account for the interference between the transmitted and reflected light at each interface as well as for the absorption of light in each layer. Furthermore, the generation rate must also take into account the luminescent photons that are produced in radiative recombinations that occur sufficiently far away from the surface, having a chance to be reabsorbed in the PK[7]. As a simple estimation, valid if the PK is sufficiently thick and the front layers are sufficiently transparent, one may ignore interference effects, parasitic absorptions and photon recycling, resulting in an exponential decrease of light intensity with depth for each incident wavelength. Then, the generation rate term is given by [31]

$$G(x) = \int_0^\infty (1 - r(\lambda)) f(\lambda) \alpha(\lambda) e^{-\alpha(\lambda)x} d\lambda \tag{2.8}$$

where r is the reflection coefficient of the stack glass/FTO/ETL/PK, f is the number of photons incident on the cell (which contains the information of the sunlight spectrum), α is the absorption coefficient of PK and λ is wavelength. Note that r depends on the complex indexes of refraction ($n - jk$, $j = \sqrt{-1}$) of all layers on top of the PK, which means it depends on the specific compositions of each layer[8]. The limit of validity of Eq. (2.8) depends on the absorption coefficient of PK. For $CH_3NH_3PbI_3$, the PK thickness must be higher than ≈ 900 nm [124]. Given that usual film thicknesses are lower than ≈ 500 nm, this equation must be used only as a rough estimation. For device simulation the full interference-dependent absorption profile must be calculated [128]. This problem can be solved analytically using the transfer matrix method [129].

The final model needed is for the profile of fixed charges, N_{ions}, throughout the PK. In silicon, this charge profile is simply a constant equal to the donor dopant density, N_D, at the n side and another constant equal to the acceptor dopant density, N_A, at the p side. In perovskites this model deserves more attention because there are overwhelming evidences of mobile ions in PK, which redistribute under applied bias [65, 130]. To account for the mobile ions, one simply has to realize that they contribute no current during steady state because they (ideally) do not flow through the contacts. Instead, they accumulate at the contacts until steady state is reached, after which their only effect is the band bending they produce. Therefore, we may obtain the distribution $N_{ions}(x)$ by equating the diffusion ion current to the drift ion current [87], giving

$$\frac{kT}{q} \partial_x N_{ions} = N_{ions} \partial_x V \tag{2.9}$$

This equation should be treated as an additional differential equation coupled to Eqs. (2.2) and (2.3).

---

[7] This phenomenon is called "photon recycling" and also occurs in Si solar cells [31].

[8] The complex refractive indexes as a function of wavelength can be found in Ref. [127] for some PK compositions.

To uniquely solve the equations one needs boundary conditions. For V, n and p, one condition is needed for each variable or variable's spacial derivative at each interface, PK/HTL and PK/ETL. For N_{ions} only one condition is needed since Eq. (2.9) is of first order, for a total of seven boundary conditions. Let $x = 0$ denote the PK/HTL interface and $x = W$ the PK/ETL interface, where W is the PK thickness. Then the conditions for V are: $V(0) = V_a - V_{bi}$, where V_a is the applied voltage and V_{bi} is the built-in voltage, and $V(W) = 0$, since we have the freedom to choose the zero of the voltage scale wherever it is desired. Note that we ignored the series resistance introduced by the ETL and HTL, so that the voltage applied drops entirely on the PK layer. This can easily be generalized with basic circuit theory.

To determine the boundary condition for the carrier concentrations we use the fact that the hole concentration at the interface PK/HTL is set by the hole quasi-Fermi level at the contact, which is equal to the voltage applied when there is no series resistance. Assuming Boltzmann statistics (i.e. non-degenarate doping) we have that the hole concentration in the PK just next to the PK/HTL interface is $p(0) = N_V \exp((qV_a - \Delta E_V)/kT)$, where N_V is the number of states per unit volume at the valence band maximum and ΔE_V is a barrier caused by band discontinuities between the HTL and PK. It is very hard to predict from first principles the value of this barrier [118], but it can be treated as an empirical parameter [116]. For the other interface, ideally no holes can pass through the ETL so that $J_p(W) = 0$, giving a condition on $\partial_x p(W)$ from Eq. (2.4). However, this is usually too restrictive, because the PK/ETL interface usually has a high concentration of defects that facilitate recombination with the electrons at the ETL. It is common to model this recombination with the same mechanism of SRH recombination discussed previously, giving a hole current of $J_p(W) = q(p(W) - p_0)S_p$, where p_0 is the equilibrium concentration of holes and S_p is the surface recombination velocity, a model parameter that depends on the amount, energetics and cross section of the interface defects [31]. This value for $J_p(W)$ can then be used in Eq. (2.4) to obtain, after some cumbersome algebra, a condition involving $\partial_x p(W)$ and $p(W)$, completing the boundary conditions for p. An exactly analogous discussion can be used to derive the boundary conditions for electrons.

The only remaining condition is then for the concentration of mobile ions, N_{ions}. Bowring et al. [87] derived this condition by using the fact that the ions do not flow through the contacts and thus their number is conserved: $\int_0^W N_{ions}(x) = N_0$, where N_0 is a constant equal to the total number of mobile ions inside the perovskite. This integral condition determines the seventh integration constant when solving Eq. (2.9).

The problem is now reduced to math. However, when the models are substituted in the Poisson and continuity equations, a highly coupled and non-linear set of differential equations results. There is no hope for an analytical solution of these equations. However, they can be, and have been, solved numerically [120,124] yielding predictions for the solar cell behavior to which measurements can be compared. Usual tools for obtaining such solutions include the finite-elements differential equation solver COMSOLE and the open-source solar cell simulator SCAPS [120]. In this thesis we will use SCAPS to help with the interpretation of results.

2.3 Figures of Merit of Solar Cells

Eq. (2.1) is plotted in Fig. 2.3 highlighting the parameters that determine solar cell performance. V_{oc} is the maximum voltage produced by the cell (for a given light intensity) and occurs only when there is no load connected to it (or, in other words, the load resistance is infinite), so obviously there is no power being drawn from the cell at this point of the J-V curve. J_{sc} is the maximum current produced by the cell and occurs only when the cell's terminals are shorted, so again there is no load and again the power produced is zero. In-between these two points the load resistance has a finite non-zero value and the power produced is also non-zero, being maximized at a unique point obtained by setting $\partial_V(J \times V) = 0$. This point is called the maximum power point and corresponds to the voltage V_{mpp} and current J_{mpp}. The efficiency, η, of the cell is obtained from

$$\eta = \frac{V_{mpp}J_{mpp}}{P_{Sun}} = FF\frac{V_{oc}J_{sc}}{P_{Sun}} \tag{2.10}$$

where P_{Sun} is the incident sunlight power per unit area and $FF \equiv V_{mpp}J_{mpp}/V_{oc}J_{sc}$ is the fill factor, being a measure of the "squareness" of the J-V curve. Although the definition of this factor may seem superfluous at this point, it is convenient when determining the effects of series and shunt resistances, both of which modify the single-exponential form of the J-V curve [31], as exemplified in Fig. 2.3b and 2.3c. It also depends on the dominant recombination mechanism, because it changes the ideality factor in Eq. (2.1) [31, 131]. When the series resistance is zero, the shunt resistance is infinite and the recombination mechanism is exclusively radiative the FF is about 90% for $P_{Sun} = 100$ mW/cm^2 with AM1.5G spectrum [31].

P_{sun} is usually considered a constant (equal to 100 mW/cm^2 with AM1.5G spectrum) during solar cell development, although it changes in the field during the Sun's movement in the sky. Device performance is thus maximized by increasing the cell's J_{sc}, V_{oc} and FF, since their product gives the efficiency for a constant P_{sun}.

To these figures of merit one should add two other related parameters: durability and cost. The cost of PK solar cells is usually not a problem, because it is made from abundant materials and because it is a thin film cell made with low temperatures, although efficient, high-area panels fabricated with scalable techniques have not been demonstrated so far. Currently, the largest concern is durability. Manufacturers of Si solar panels usually give warranties that the panels will have at least 80 % of its initial efficiency after 25 years of fabrication. This 80 %-time, T_{80}, has become a figure of merit for solar cell degradation assessment. Unfortunately, only in a few cases the T_{80} of PK solar cells is larger than a year [98] and, in most cases, it is of order of a month. In the Results chapter, we will show developments on the understanding of the degradation mechanisms discussed in Section 1.3.3.

2.4 Additional Considerations for Si/Perovskite Tandems

This thesis will not present results on Si/PK tandem solar cells. However, the single-junction cells that will be analyzed are optimized so that they can be applied in tandems, so a quick review on the peculiarities of tandem cells will be given.

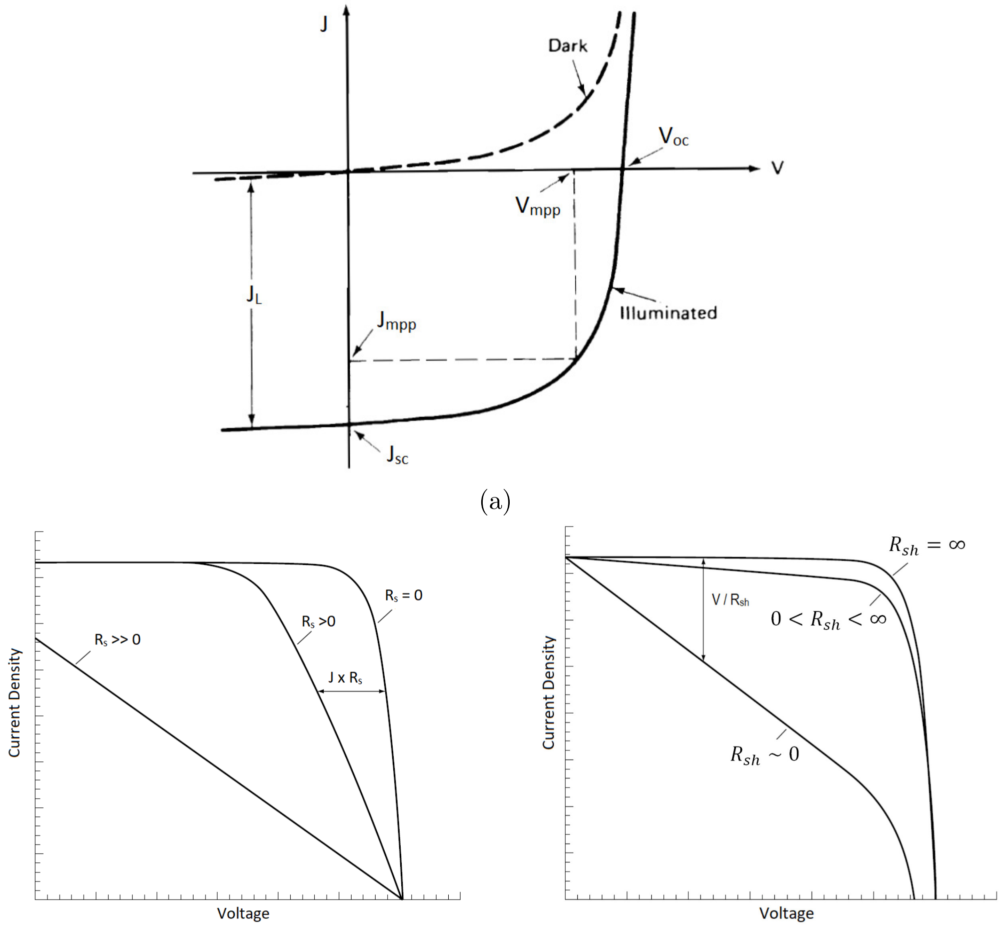

(a)

(b)

(c)

Figure 2.3: a) Generic J-V curve of solar cells illustrating the figures of merit. From Ref. [115] b) Effects of series resistance and c) effects of shunt resistance on the J-V curve, from Ref. [31]. Note that in b) and c) the y axes are inverted, so that produced current is positive.

When tandems are under consideration, one must first decide if the subcells are to be fabricated independently and later stacked mechanically, as shown in Fig. 2.4a, or if the subcells are to be fabricated monolithicaly (i.e., in a single device) [103, 113], as shown in Fig. 2.4b. Fabricating the cells independently has the obvious advantage of process simplicity, since fabrication constraints of one cell (e.g., temperature tolerance, surface roughness, solvents) do not affect the fabrication of the other cell, but are also less cost effective because at least an additional layer (a transparent electrode) is required compared to the monolithic design. For this reason we concentrate only on monolithic structures[9] even though the fabrication complexity is higher.

Having chosen the monolithic design, the simplest way to connect the subcells is in series (Fig. 2.4b). In this case the tandem must be fabricated such that both subcells have the same polarity (both n-p or both p-n), otherwise they will simply shunt each other.

---

[9] Instead of stacking the subcells, one could also use mirrors and filters to redirect the parts of the solar spectrum to the appropriate cells [31, 103]. However, the optical system introduces more cost and the area needed for the solar panels approximately doubles.

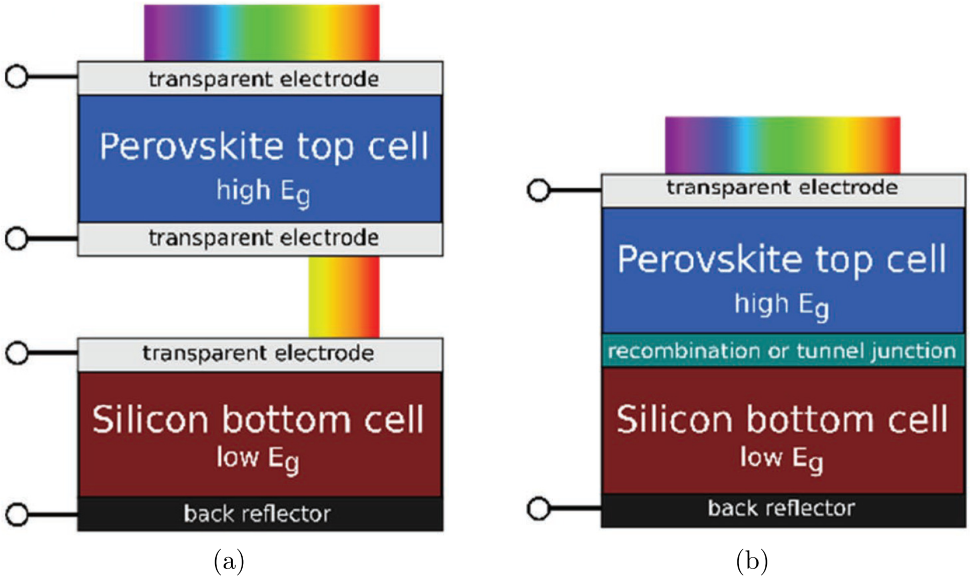

Figure 2.4: Possible configurations for Si/PK tandem solar cells. a) Mechanically stacked. b) Monolithic. From Ref. [103].

Since the cells are in series, they operate at the same current, meaning the fabrication of each cell must be tailored so that their maximum power points occur at the same current, otherwise the cell with lower current will force the cell with the higher current to operate out of its maximum power point. If the cells are fabricated such that both produce the same current, they are said to be current-matched. This is achieved by selecting a PK with appropriate bandgap and by tailoring its thickness. The tandem cell will then have the lesser of the two currents and the voltage equal to the sum of the two subcells voltages.

The analysis of multijunction solar cells follows the same strategy outlined in section 2.2. The main difference is that, for the bottom cell, the integrand in the generation rate expression (Eq. (2.8)) must be multiplied by $\exp(-\alpha(\lambda)W)$ to account for the light absorbed in the top cell. This changes the value of J_L in Eq. (2.1), but not the form of the diode law. The Si cell in the tandem device will produce less current than it would produce by operating alone in a single junction device, since most of the higher energy photons are not reaching it. However, the tandem cell voltage is approximately the sum of the voltages of each subcell operating individually, since it depends only on the logarithm of J_L and the light intensity.

An example of complete Si/PK tandem cell is illustrated in Fig. 2.5. Note that an intermediate layer is required to connect the two subcells. Without it, the n or p layer of the bottom cell would create a reverse biased diode with the p or n layer of the top cell. To circumvent this problem one uses a tunnel junction or a recombination layer. The purpose of both is to facilitate the recombination of photoholes from one cell and photoelectrons from the other. Consider first the tunnel junction. Electrons generated in the Si bottom cell reach this junction from the n^{++} side and holes generated in the PK top cell reach this junction from the HTL/p^{++} side. These carriers then recombine with each other by band-to-band tunneling. The series resistance associated with this junction is the bulk resistance of the p^{++} and n^{++} layers, which is negligible because both layers are heavily doped and very thin (a few nanometers), and the resistance associated with the tunneling process, which is also small because a high tunneling transmission probability is obtained when the layers are so heavily doped that the depletion layer becomes very thin [116]. A recombination layer, which could be used in the place of the tunnel junction, is simply a conductive layer such as ITO or similar transparent metal-like material which is able to make ohmic contacts to both p and n layers above and underneath it.

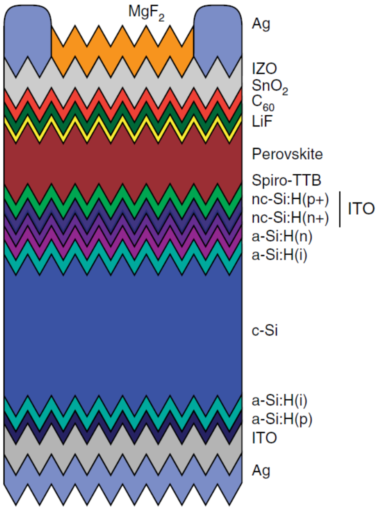

Figure 2.5: Example of Si/PK monolithic tandem design. The top MgF_2 is an anti-reflection coating deposited by thermal evaporation. IZO is deposited by sputtering and is used to improve lateral conductivity to the Ag contacts. SnO_2 is a buffer layer to prevent sputtering damage of IZO on C_{60} and is deposited by ALD. C_{60} and LiF together form the ETL of the PK subcell and are deposited by thermal evaporation. The PK is deposited by a two-step method, first evaporating PbI_2 and CsBr and then depositing FAI and FABr by spin-coating. Spiro-TTB is the HTL and is also deposited by evaporation. The amorphous layers of the SHJ bottom subcell are deposited by PECVD. The connection of the two subcells is made by a nanocrystalline-Si n^{++}/p^{++} tunnel junction or with an ITO recombination layer. From Ref. [99].

It may seem strange that one can improve solar cell performance by facilitating recombination between photoelectrons and photoholes. The catch here is that these carriers do not come from the same cell. It may be remembered from the discussion in Section 2.1 that easy recombination means the quasi-Fermi levels will be equal, which is exactly what is wanted here. The quasi-Fermi level of holes from the bottom cell should be the same as the quasi-Fermi level of electrons of the top cell (or, in other words, there should be no voltage drop in between the top contact of the bottom cell and the bottom contact of the top cell).

Chapter 3

Methods

Many different combinations of layers and fabrications procedures were studied during this work. Describing every procedure in each experiment is impossible. Therefore, we have structured this chapter in two parts, as follows. First we will give a general explanation of solar cell fabrication, without mentioning details of thin film deposition procedures. Then, these details are described separately in specific sections for each layer recipe. In the Results chapter, the devices analyzed are applications of the recipes described in the second half of this chapter using the architectures described in the first half.[1] Finally, we describe the characterization techniques and the simulation parameters used to study the devices.

The steps necessary to fabricate PK solar cells are shown in sequence in Tab. 3.1 and the final device is shown in Fig. 3.1. Note that this is not meant to be an extensive review of thin film deposition techniques, but merely to describe the nuisances of these techniques when used for the materials involved in the perovskite solar cell. A thorough review paper giving the subtle (but important) details on fabrication procedures is given in Ref. [132], but it should be noted that it is not uncommon to have irreproducible results with these techniques. Although the field develops rapidly, PK technology is still in its infancy.

We mention that some results on layer characterization will be given in this chapter instead of in the Results chapter. The latter will be reserved for the results obtained in complete devices.

3.1 Overview of Solar Cell Fabrication

All devices studied in this work were fabricated in 2.5 cm x 2.5 cm glass/ITO (sheet resistance of $\sim 5\ \Omega$/sq) or glass/FTO (sheet resistance of $\sim 7\ \Omega$/sq) slides.

The first step is to pattern the ITO or FTO substrates so as to avoid shunting between the two contacts in the final device. Note in Fig. 3.1 how the top contact is deposited partly on a region without ITO underneath. This prevents it from shunting to the bottom contact when the probes of the measuring device are forced against it. Also note how the bottom contact is also electrically connected laterally to the top contact. This is not

---

[1] Note that not all combinations of layers are possible because of constraints that the deposition of one layer imposes on the remaining ones, such as temperature, surface roughness, material hardness and solvents.

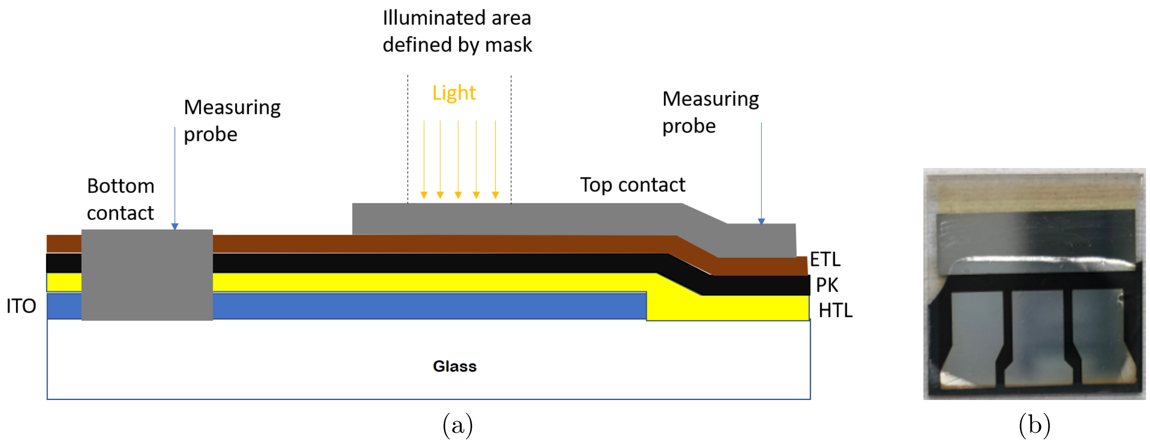

Figure 3.1: a) Illustration of the solar cell's cross-section. b) Picture of real device seen from the top view (when testing, illumination comes from the other side).

Step	Materials used	Equipment
Substrate Patterning	—	Fumehood
Substrate cleaning	ITO- or FTO-coated glass, acetone and isopropanol	Fumehood with ultrassound.
Surface activation*	O_2 gas	Plasma chamber.
HTL	NiO or PTAA	Sputtering or spin-coating
Perovskite deposition*	PbI_2, $PbBr_2$, MAI, MABr, FAI, FABr, CsI, CsBr	Spin-coating. Inside a glovebox.
ETL deposition	C_{60}	Evaporation. Inside a glovebox.
Back metal contact	Ag, Al, Au, ITO, etc	Evaporation or sputtering.

*Ideally, this step should be performed immediately before the next step

Table 3.1: Fabrication steps used in this work to fabricate p-i-n PK solar cells.

a problem because the lateral separation between the top and bottom contacts are a few millimeters while vertically the separation is only about one micrometer, so the lateral conductance is negligible. Also note that, even though the bottom ITO presents metallic conduction, we still deposit a metal on the bottom contact to reduce contact resistance with the measuring probe. Both top and bottom metal contacts are deposited during the same deposition.

Then, after the substrates are cleaned, each layer of the cell is deposited in sequence. The first layer is that which will be facing the Sun in the final device, so if it is an ETL, the cell will be of n-i-p type. If it is an HTL, the cell will be p-i-n. In the cells studied in this work, this first layer was one of the four following possibilities: 1) spin-coated TiO_2; 2) sputtered TiO_2; 3) sputtered NiO; or 4) spin-coated PTAA. The first two result in n-i-p cells and the other two result in p-i-n cells. Notice that this layer is chosen taking into account that it will have to endure the solvent of the PK, which will be deposited right on top of it, and the annealing of every subsequent layer. For the PK, several compositions in the formula $(CsFAMA)Pb(IBr)_3$ were tested. For the layer on top of the PK, we used one of the three following possibilities: 1) evaporated C_{60}; 2) SnO_2 from ALD; or 3) spin-coated P3HT (for n-i-p configuration). For the back metal contact, we explored Ag, Cu, Ni, Al, Au and ITO. All layers are deposited inside a glovebox, with the exception of NiO for p-i-n cells, TiO_2 for n-i-p cells and SnO_2 in semi-transparent p-i-n cells.

Before the top contact is deposited, it is necessary to open a path for the bottom contact to reach the ITO. This is accomplished by scratching away all layers of the cell with a scalpel in the region where the contact will be deposited. The bottom ITO, which comes with the glass substrate, is not scratched away with the scalpel because it is a harder material. Note that if one of the cell layers is too hard, it might not be possible to scratch this layer with the scalpel. In our cells this was the case with NiO and TiO_2. To avoid this problem, we covered the region where this contact is deposited with tape before depositing the NiO/TiO_2, so that the bottom contact region is free from this material when scratching.

Each substrate contains three separate solar cells. The advantages of making more than one cell per substrate is that it gives better statistics and allows some cells to be recuperated in the cases where one or more layers are locally scratched by accident during device fabrication. The device is measured using a mask with 5 mm x 5 mm windows positioned in the centers of each solar cell. The top contacts themselves are about 8 mm x 8 mm, but when measuring the device the illuminated area is much more conductive then the dark regions, so the effective cell area is 5 mm x 5 mm. (For dark measurements, the cell area is not very well defined with this architecture.)

It is important to take care when measuring the solar cells so as not to puncture the active cell region with the measuring probes. It is advised to make a dedicated sample holder for measuring the solar cell, preferably with a setup that uses the four-point technique to eliminate the series resistance between the measuring probes and the cell's contacts. This technique was used in all measurements of solar cells in this work.

The most basic cell architecture only requires a glovebox, a spin-coater and a hot plate to deposit the ETL, HTL and PK and an evaporator to deposit the metallic back contact. Cells with more than 20% efficiency have been demonstrated with such a simple setup [62, 132]. However, industrial scale devices will certainly not use spin-coating, so preferably the lab should be equipped with vapor-deposition equipments such as a chemical vapor deposition (CVD) chamber, an atomic layer deposition (ALD) chamber and a sputtering chamber, or other solution processing equipments such as blade-coating or screen-printing. Also, ideally the glovebox should contain an evaporator inside of it if layers that cannot be exposed to air have to be deposited. This was the case for the deposition of LiF and C_{60} on top of the PK in some p-i-n cells described in this thesis. For measurement techniques, at the very least the lab must have a Sun simulator and an IV-curve tracer. The next most useful equipment is a device to measure External

Quantum Efficiency (EQE); this equipment is a broadband lamp coupled with a chopper and a monocromator and a precision current measuring device (current measurement is performed with the lock-in principle).

We mention that part of this work was performed in the Microelectronics lab at UFRGS, Brazil and part was performed in the PV-lab at EPFL, Switzerland.[2]

3.2 Substrate Patterning, Cleaning and Surface Activation

Patterning can be accomplished with a solution that removes ITO and covering the relevant regions with tape. It is also possible to purchase the ITO glasses already patterned, which was the case for most cells of this work.

After substrate patterning, device fabrication proceeds by cleaning the ITO or FTO surfaces. This is accomplished with ultrassonication at ∼50 °C for 10 min first in acetone and then in isopropanol. Then, the samples are rinsed in DI water and quickly dried with a N_2 gun. This procedure can be done days in advance of the rest of cell fabrication, but preferably it is done within a day before the first layer is deposited. The substrates should always be kept inside a clean, dust-free environment, preferably a clean room.

If the first layer is deposited by spin-coating, a surface treatment is applied in an O_2 plasma chamber right before spin-coating. This surface treatment serves two purposes: to clean any residual carbon in the surface and to “activate” the surface with O bonds that improve wettability of the spin-coating solution. In this treatment the substrate surfaces are subjected to an O_2 plasma (O_2 pressure of about 1000 mTorr) for 5 min. If the samples are warm as a consequence of the plasma, they are left to cool for a few minutes before the start of spin-coating.

3.3 Recipes

3.3.1 Spin-Coated TiO_2

The substrate where TiO_2 is spin-coated must be FTO because an annealing step at 500 °C is necessary and ITO is degraded at such temperatures. This is also why TiO_2 can only be used below the PK, as the PK also cannot survive such high temperatures.

We used the organometallic molecule titanium diisopropoxide bis(acetylacetonate), shown in Fig. 3.2, as the TiO_2 precursor. Note that the precursor molecule is not the same as the final product, TiO_2, so during spin-coating reactions need to take place to produce the desired material. These reactions are instances of sol-gel chemistry, a well known technique [133] to produce oxides from organometallic compounds. In this case, water molecules attack the Ti-propoxide bonds producing TiOH bonds plus isopropanol. Then, two TiOH bonds react with each other to produce water and a Ti-O-Ti bond, which

---

[2] Also, we mention that two of the layers used in this thesis, NiO by sputtering and SnO_2 by ALD, were not fabricated by the author and will not be discussed. Instead, these layers were fabricated at the company CSEM, Neuchâtel, Switzerland. The recipes for these layers were always the same for every device that used them.

links the molecules together to form the TiO_2 framework. Water must be present during spin-coating, but usually the water vapor from air is enough to catalyze the reaction.

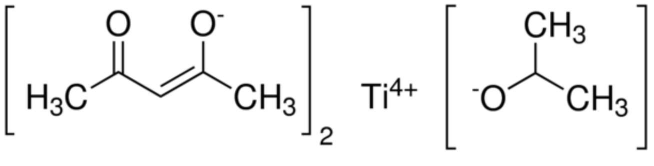

Figure 3.2: Titanium diisopropoxide bis(acetylacetonate), the precursor molecule used to fabricate TiO_2 layers by spin-coating.

The precursor is bought from Sigma Aldrich at 75 %wt, or 2.01 M, in isopropanol. All chemicals are handled in air inside the chapel of a clean room. In our recipe, we further diluted the precursor to 0.30 M with isopropanol. Different concentrations can be used to vary the thickness of the layer; a concentration of 0.30 M results in approximately 40 nm before annealing. For the deposition, 200 μL of the solution are dropped on the center of the FTO surface and the substrates are spinned at 3000 rpm for 30 s. The samples are then dried in a pre-heated hot plate at 125 °C. The resulting layer had an index of refraction of ~ 1.3 at 550 nm (as measured by ellipsometry, Tab. 3.2), indicating that it is very porous because the index of refraction of bulk TiO_2 is 2.48 [134] at this wavelength. To densify the layer, we annealed the samples at 500 °C for 30 min in an O_2 atmosphere. The resulting layer had thickness of ~ 20 nm and $n = 1.9$ (Tab. 3.2).

This recipe was obtained after an optimization of the layer using different precursor concentrations (0.30 M and 0.15 M), spin-coating speeds (1500 rpm and 3000 rpm) and annealing temperatures (480 °C, 500 °C, 520 °C and 540 °C). Tab. 3.2 shows the thickness and index of refraction for these different deposition parameters. The values of 0.30 M, 3000 rpm and 500 °C were chosen for device fabrication because they resulted in an appropriate thickness ($\sim$ 20 nm after annealing) and index of refraction (1.9).

Table 3.2: Thicknesses and refraction indexes of the TiO_2 films measured by ellipsometry.

Sample	d (nm)	n (550 nm)	R^2
0.15/AD	26.9 ± 0.2	1.305	0.9986
0.30/AD	43.9 ± 0.3	1.376	0.9945
Sputtering/AD	19.64 ± 0.05	2.234	0.9938
0.15/420	15.6 ± 0.2	1.447	0.9982
0.30/420	19.6 ± 0.1	1.730	0.9732
0.15/480	16.8 ± 0.1	1.478	0.9980
0.30/480	16.19 ± 0.03	1.914	0.9393
0.15/540	16.7 ± 0.15	1.394	0.9992
0.30/540	24.8 ± 0.18	1.594	0.9910
Sputtering/500	21.4 ± 0.1	2.484	0.9479

* AD = as deposited; d = thickness; n = index of refraction; R^2 = coefficient of determination from fitting.
** The uncertainties from ellipsometry correspond to the fitting procedure, not to film uniformity.

For comparison, we also deposited 20 nm layers of TiO_2 by sputtering. The resulting layer had $n = 2.28$, meaning it is significantly more dense than the spin-coated layers. After performing the same annealing treatment for these sputtered layers, we obtained $n = 2.48$, indicating that the final layer is as dense as bulk TiO_2.[3]

We also measured the photoluminescence of the TiO_2 layers using a 266 nm laser. A representative spectrum obtained is shown in Fig. 3.3. (We observed very little variation between the PL spectra of layers deposited in different conditions.) These spectra show three peaks, one at 3.4 eV that agrees with the bandgap of TiO_2 [135], and the other two at 2.9 eV and 2.5 eV that agree with transitions caused by oxygen vacancies and titanium intersticials [136, 137]. It is expected that these defects act as donor dopants in TiO_2, so even though the bandgap is large, an appreciable electron conductivity for these layers is expected.

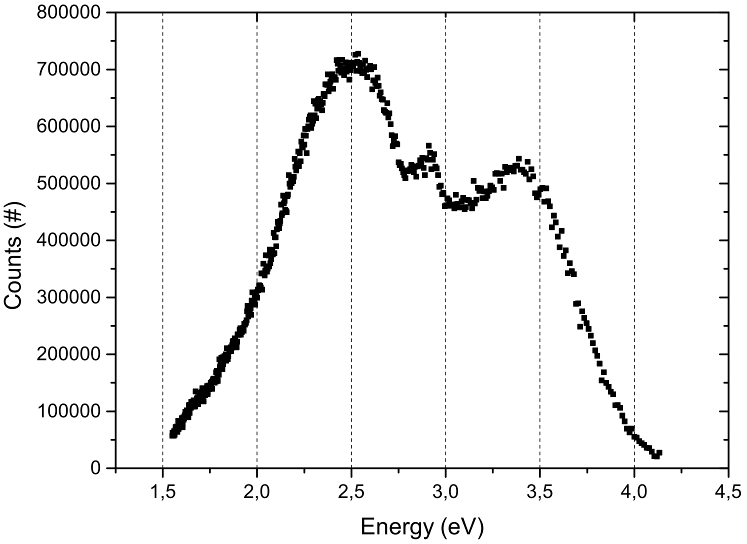

Figure 3.3: Representative photoluminescence spectrum of TiO_2 deposited by spin-coating.

3.3.2 Spin-Coated PTAA

The molecule of PTAA is illustrated in Fig. 3.4. The following simple recipe can be used to deposit it on ITO substrates. First, a 1-5 mg/mL solution of PTAA in toluene is prepared. The solution does not need to be prepared for each batch; as long as it is properly stored inside a glovebox, the same solution can be used for at least a month. For spin-coating, we used 1000 rpm for 20 seconds with acceleration of 1000 rpm/s. The thickness of the layer can be controlled by varying the solution concentration and the spinning speed. For 5 mg/mL and 1000 rpm, the resulting thickness is approximately 15 nm. The layer is transparent and, if successfully deposited, cannot be noticed with the

---

[3] A TiO_2 layer as dense as possible is not necessarily better than a porous one. For PK deposition, it is in fact desired to have a rough layer to assist PK crystallization during spin-coating [94].

naked eye. However, one can test the presence of the layer by scratching a corner with a metallic tweezers.

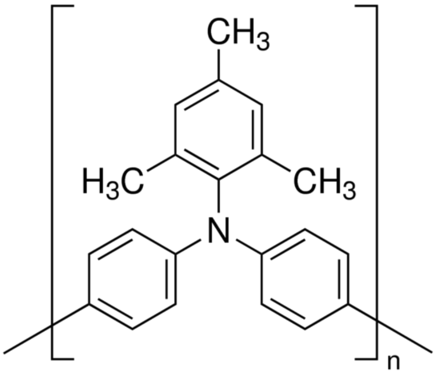

Figure 3.4: Molecule of poly(triaryl amine), or PTAA.

It must be mentioned that, although PTAA is one of the best-performing HTLs for PK solar cells found so far, depositing the PK on top of it is very tricky because the PK solvents do not properly wet the PTAA surface [138]. Frequently the PK solution is simply thrown away from the PTAA surface as soon as the substrate starts spinning. The exact variables that control the deposition of the PK on top of the PTAA are still currently unknown, and some labs are able to reproducibly fabricate it while others cannot, even though the same recipe is used[4]. In this work, we managed to make some working cells with PTAA, but there was a lot of batch-to-batch variation.

Some researchers use an additional thin layer (usually only a few monolayers) on top of the PTAA in order to aid the PK deposition. A popular material used for this purpose is poly[(9,9-bis(30-((N,N-dimethyl)-N-ethylammonium)-propyl)-2,7-fluorene)-alt-2,7-(9,9-dioctylfluorene)] dibromide (also known as PFN-P2) [138]. Although some authors report better results with this "interface compatibilizer", we have not found it to improve reproducibility in our recipes.

3.3.3 Spin-Coated Perovskite

There are many routes for depositing PK layers, such as using purely solution processing (e.g. spin-coating, blade coating, slot-die coating), purely vapor deposition (e.g. co-evaporation, chemical vapor deposition) and hybrid methods, where the inorganic part of the PK is first deposited by vapor methods and then the organic part is deposited by solution processing. Each method has advantages and disadvantages, but arguably the simplest technique is spin-coating. This is the method used in all cells produced in this thesis (even though it is not applicable in large scale production), so we only describe this method. Most of the record-efficiency PK cells to date still use spin-coating to deposit the PK layer [132].

---

[4] Some of the variables that are not usually controlled between different labs are 1) the molecular weight and the purity of the PTAA used (which can change from supplier to supplier), and 2) the glovebox temperature during the deposition (which can change from day to day). Some researchers have proposed that controlling these variables would yield more reproducible results.

Depositing the PK layer by spin-coating is the most user-dependent, and therefore the most sensitive, part of cell fabrication. First, the solution is prepared, preferably not more than a week before the spin-coating is to be performed. This is done inside a nitrogen-filled glovebox, where the solution is always kept. A new solution is prepared for each batch of cells.

Solution preparation can be accomplished in two possible ways: 1) first introduce all necessary powders in the same vial and then add the solvents to this vial; or 2) first dissolve each PK precursor in separate vials and then mix each precursor solution in the appropriate ratios in another vial. The first method has the advantage that more concentrated solutions can be made, but it can be less precise if the user does not take the appropriate care when mixing and weighing powders, which can be cumbersome when handling chemicals inside a glovebox. The second preparation option gives more precise precursor concentrations, but may not be applicable if too-concentrated solutions are necessary. For example, if one wants to prepare a 1.5 M solution of $MAPbI_3$ with solutions of MAI and PbI_2, these precursor solutions would have to be 3 M before mixing equal volumes of each. Unfortunately, the maximum solubility of PbI_2 is less than 3 M in all the common solvents (in DMF and DMSO it is about 1.6 M), so one has to take the first preparation method. All PK solutions used for this thesis were prepared with the first method.

The total volume of solution prepared for a batch depends on how many cells will be fabricated in the batch. For the 2.5 cm x 2.5 cm substrates used in this work, the volume of PK solution used per sample is 100 μL, so the total volume, V, is $V = N \times 100$ μL, where N is the number of cells. The weight of each powder i necessary to make the solution can be calculated from

$$m_i = M_i \mathcal{M}_i V \tag{3.1}$$

where m_i is mass, M_i is molarity, $\mathcal{M}_i$ is molar mass. An example calculation is shown in Table 3.3 for preparing a 1.5 M solution for 10 layers of $(CsPbBr_3)_{0.17}(FAPbI_3)_{0.83}$ from the precursors PbI_2, $PbBr_2$, FAI and CsBr (all purchased from Sigma with 99.99 % purity). In this example, we use DMF:DMSO 4:1 (both from Sigma, anihydrous) as solvent, a solvent composition taken from the literature [96] that was used in all cells fabricated for this thesis. After the powders and solvents are mixed, the solution is left to dissolve in a hot plate at 70 °C until it is completely transparent, which takes about 30 minutes.

Precursor	Molar mass	Desired molarity	Quantity used
PbI_2	461.01 g/mol	1.25 M	575.3 mg
$PbBr_2$	367.01 g/mol	0.25 M	91.8 mg
FAI	171.97 g/mol	1.25 M	215.0 mg
CsBr	212.81 g/mol	0.25 M	53.2 mg
DMF	-	-	800 μL
DMSO	-	-	200 μL

Table 3.3: Example calculation to prepare a 1.5 M solution of $(CsPbBr_3)_{0.17}(FAPbI_3)_{0.83}$ for 10 cells.

It is during spin-coating that the PK crystallizes from its precursors. In solution, the PbX_2 and AX are still separated (the solution is yellow, the same color as PbI_2).

Crystallization is caused by the evaporation of solvent during spin-coating, forcing the solutes beyond the solubility limit of the solvent. The solvent is strategically chosen in this context so as to balance the effects of a too-rapid crystallization, which would cause the PK to be very rough and with small grains, and a too-slow crystallization, which would cause the PK layer to be too thin. Usually an antisolvent recipe is used when spin-coating PK layers [96]. An antisolvent is a molecule that lowers the solubility of a solvent with respect to a solute (i.e. it is miscible in the solvent but it does not dissolve the solute). In this case, one wants to lower the solubility of the PK in the solvents DMF and DMSO in order to aid the precipitation of the PK phase. Common antisolvents are chlorobenzene, toluene and diethyl ether [96, 132].

Actually, DMSO does not only act as a solvent, it also forms complexes with PbI_2, such as $PbI_2(DMSO)_2$ [96, 139]. DMF is the actual solvent in this solution. During spin-coating, the $PbI_2(DMSO)_2$ complexes react with the other PK precursor AX to form an intermediate phase, generically called AX-PbI_2-DMSO. This phase is the brown layer observed before annealing. When heated, the DMSO evaporates and the PK phase is formed. This entire mechanism is illustrated in Fig. 3.5 and described in more detail in Ref. [96].

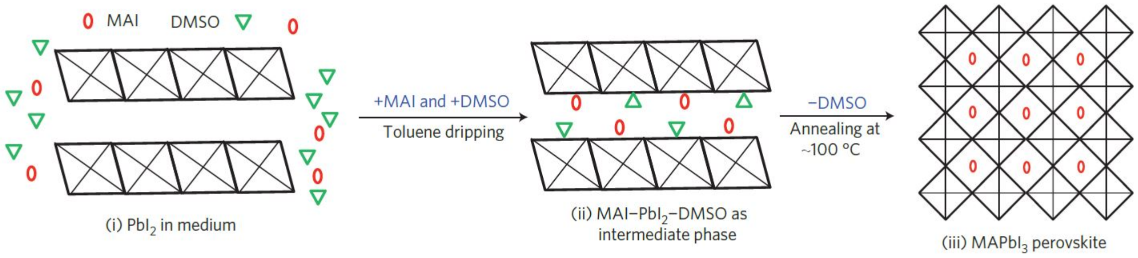

Figure 3.5: Formation mechanism of perovskite layers deposited with the antisolvent method. From [96].

The spin-coating recipe used in this work is as follows. First, 100 μL of solution is applied on the center of the sample and then a two-step recipe is begun: first at 1000 rpm for 10 s with acceleration of 200 rpm/s and second at 6000 rpm for 25 s with acceleration of 1000 rpm/s. The purpose of the first step is to evenly distribute the solution on the sample surface and for highly wettable surfaces it is not strictly necessary. At 5 s before the end of the second step, 200 μL of chlorobenzene (the antisolvent) is quickly dripped at the center of the rotating sample. At this stage the PK layer has a hazy brown color. Then the substrates are annealed in a pre-heated hot plate at 100 °C for 1h. In the first few seconds of annealing the PK color goes from brown to black.

The application of antisolvent during the deposition of the perovskite layer is a crucial step for obtaining high efficiency cells with the spin-coating method. Unfortunately, it is highly user-dependent and takes some practice before reproducible results can be obtained. Also, the details of this technique are not frequently published, probably because spin-coating is not a viable technique for the industry. Several not-well-controlled variables affect the deposition, such as: the speed with which the antisolvent leaves the pipette, how vertical the pipette is during deposition, the height between the pipette tip and the sample, the moment of application and even the temperature of the glovebox. It is not easy to control these parameters, so usually it takes a few batches for the user to standardize its technique. In the Results chapter we will show how small differences in the application technique of the antisolvent can have an influence on the complete device.

3.3.4 Spin-Coated P3HT

The P3HT layer is deposited immediately after depositing the PK, inside the glovebox. If the substrates are still hot from the PK annealing, they are left to cool for a few minutes before depositing the P3HT. The recipe for this layer was adapted from [140] where it was used to fabricate organic transistors.

We mention that it is not necessary to prepare a new solution of P3HT for each batch (we found reproducible results even after months using the same solution). The spin coating recipe used is 1000 rpm for 30 s. After spin-coating, the samples are immediately annealed in a pre-heated hot plate at 105 °C for 10 min.

3.3.5 Evaporated LiF and C_{60}

The LiF and C_{60} layers are used in p-i-n cells. (Note that LiF is used only as a passivator [138]. The electron selector is really C_{60}.) They are deposited immediately after the PK and the samples do not leave the glovebox between the PK and LiF/C_{60} depositions.

The evaporator used to deposit LiF and C_{60} layers was installed inside a glovebox (Fig. 3.6) so that the samples do not have to leave the inert environment. It is equipped with a crystal balance to monitor the deposition rate in real time, a shutter to stop the deposition instantaneously and two boats so that two different materials can be deposited without breaking vacuum. It also allows for the samples to rotate during deposition to improve uniformity. This same chamber also allows for sputtering depositions; the target is kept at the left of the chamber and can move to be aimed at the samples if activated by the user. The vacuum is produced with a turbomolecular pump. The boats are heated using the same power source (which can be alternated to power either boat, but not both boats at once). The power source keeps the power constant, not the temperature. The user may change the power manually during deposition to keep the deposition rate (monitored with the crystal balance) at the desired level.

When starting a deposition, the materials and samples are first loaded and the chamber is evacuated until the pressure reaches 2×10^{-6} mbar or lower. Then, the boats are heated first with the shutter closed, so as to evaporate some small amount of material on the shutter instead of on the samples. This is done to prevent possible surface impurities that may be present on the materials to be deposited and also to stabilize the deposition rate. The material of the boats themselves (in this case Al_2O_3) are chosen so as to not react with the material to be deposited.

The precision in thickness for evaporated layers is usually ∼1 nm or less. To calibrate the crystal, a tooling factor is measured (for each different material) by depositing a standard layer and measuring the thickness with a precision profilometer (precision of ∼1 nm) or with a scanning electron microscope (SEM). In all solar cells that used LiF and C_{60} in this thesis, the thickness of LiF was 1 nm with deposition rate of 0.2 Å/s and that of C_{60} was 20 nm with rate of 0.5 Å/s.

Figure 3.6: Picture of the evaporator (inside a glovebox) used to deposit LiF, C_{60} and the Ag contact.

3.3.6 Sputtered ITO and IZO

Semitransparent cells use a TCO as the top contact. The semitransparent cell still has metallic top contacts, but it is deposited as a grid in the perimeter of the active area instead of covering the entire active area. Only p-i-n semitransparent cells were fabricated in this thesis. In these cells, a layer of SnO_2 is first deposited by ALD on top of the C_{60} layer and then the TCO is deposited on top of SnO_2. The purpose of the SnO_2 layer is to prevent damage of the C_{60} by the TCO during sputtering. Ideally, for this architecture the ETL would be only SnO_2, without C_{60}, but (for reasons still obscure) the deposition of SnO_2 by ALD damages the PK underneath.[5] Therefore, we kept a C_{60}/SnO_2 stack as ETL for semitransparent cells.

We tested four different TCOs in this work: ITO (indium tin oxide), IZO (indium zinc oxide), IZrO (indium zirconium oxide) and AZO (aluminium zinc oxide). However, only ITO and IZO resulted in working devices. Probably the problems with IZrO and AZO were not related to device architecture, but instead to not optimized recipes for these layers.

The TCO sputtering was performed in the same chamber of the LiF and C_{60} described in the previous section. The target is composed of 90 % In_2O_3 and 10 % SnO_2. We used reactive sputtering; a partial pressure of 10 mTorr of O_2 is present during deposition together with an Ar partial pressure of 100 mTorr. Before beginning the deposition by opening the shutter, the target is sputtered for 30 s to remove surface impurities.

---

[5] It is conjectured that the damage is caused by one of the precursors of SnO_2 used in ALD: water. Halide perovskites are known to be very sensitive to humidity [141]. It is also possible that the perovskite is just not able to seed the growth of SnO_2 in the ALD technique.

3.4 n-Si/TiO_2/Al Devices

During the characterization of TiO_2 layers, we discovered an interesting effect for the structure n-Si/TiO_2/Al. The effect was published in Ref. [142] and will be described in the Results chapter. It is completely unrelated to perovskite solar cells, but we still think it is worth describing because it gives insight to the behavior of heterojunctions.

The structure is fabricated on a heavily doped n-Si wafer (resistivity of 0.01 Ωcm) that has a 60 μm thick n-Si epitaxial layer of high resistivity (resistivity of 20 Ωcm, donor density of 2×10^{14} cm^{-3}). The substrate was cleaned with a piranha solution and an HF dip prior to the TiO_2 deposition by spin-coating, which followed the recipe described in Sec. 3.3.1. Then, Al disks with 100 μm radius and $\sim$ 500 nm thickness were deposited by thermal evaporation through a shadow mask. The back contact to the n-Si wafer was made with an eutectic InGa alloy, which is known to provide an ohmic contact to the Si wafer.

3.5 Characterization Techniques

3.5.1 Current-Voltage

J-V curves are measured using a Sun simulator and a Keithley. The Sun simulator is composed of a Xe lamp and a halogen lamp and filters to approximate the Sun's spectrum. The intensity is calibrated by measuring the J_{sc} of a standard Si solar cell. The Keithley is controlled with a homemade software using LabView. The sample holder uses the four-point technique to eliminate series resistance between the probing contacts and the cells contacts.

The J-V scans were always performed in both directions, first with a forward (from -0.1 V to 1.2 V) and then with a backward scan (from 1.2 V to -0.1 V). The voltage step was always 20 mV. The delay (i.e. the time between arriving at the voltage V and the start of the current measurement) was always 10 ms, and so was the integration time for each voltage step.

Note that 10 ms is a not-too-short and not-too-long time scale compared to the time scales involved in ion conduction inside the PK [120]. If the delay in each point of the voltage scan is very long, ions will reach equilibrium in each voltage point, while if it is very short the ions do not have time to move at all. In both these situations one would not expect hysteresis between forward and backward scans. In perovskites, however, the delay would have to be impractically short or long to avoid these problems [143], so most researchers (ourselves included) use time scales around 10 ms and just accept that hysteresis will be observed. But this means that care must be taken to extract the J-V parameters from the measurement, because forward and backward scans can give different values.

A common way to avoid this problem and to ensure that the correct efficiency is measured is to use Maximum Power Point Tracking (MPPT), which we have used in numerous cases. Here, instead of a voltage scan, one applies a voltage close to V_{mpp} and uses a perturb-sense algorithm [144] to search if a nearby voltage actually gives a higher efficiency. As ions move, V_{mpp} changes, but the algorithm keeps tracking what the new value is. Usually after a few tens of seconds (sometimes a few minutes) the voltage stabilizes at the maximum power point, and the efficiency can be extracted with much better precision than with the regular J-V scan.

Some structures studied in this work used very small contacts (0.2 mm in diameter). In this case, the measuring probe is a tungsten needle with a tip of about 0.1 mm or less. The probe is positioned on the contact with the help of an optical microscope.

3.5.2 Capacitance-Voltage

We used the capacitance-voltage (C-V) technique to study TiO_2 and P3HT layers. The purpose of the technique is to measure how the capacitance of the sample changes with applied voltage, a dependence that can be related to the properties of the layers and interfaces of the sample. It is discussed in much detail in textbooks by Nicollian & Brews [145], Sze [116] and Schroeder [146]. Here, we will only discuss the setup used to obtain C-V curves in this work. Our impedance measurement device was an HP4284A, which allows for precision of 1 pA in current measurements up to frequencies of 10 MHz.

In this technique, a small oscillating voltage (in this work, always of 20 mV amplitude) is superposed on a DC bias and applied at the sample. The current passing through the sample as a result of the applied voltage has a DC component, which is ignored, and an oscillating component, of which the amplitude and phase with respect to the applied voltage is measured. The DC bias is scanned as for J-V curves. The frequency of the applied oscillating voltage can be changed to probe the response time of carriers or to change the importance of parasitic resistances with respect to the desired capacitance.

The amplitude and phase of the AC current signal caused by the applied voltage depend on the capacitance and resistance of the sample. If the sample does not conduct current at all, it will be a pure capacitor, the phase will be $-90°$ and the amplitude will be $\frac{1}{\omega C}V_{AC}$ where ω is the angular frequency of the applied voltage, V_{AC} is the amplitude of the applied AC voltage and C is the desired sample's capacitance. In general, the sample has some conductance and some series resistance, so it can be modeled as in Fig. 3.7 with a parallel resistance R_p and a series resistance R_s. Then, the phase ϕ and amplitude i_{AC} are given by

$$\phi = -\text{arctg}\left(\frac{\omega R_p^2 C}{R_p + R_s(1+\omega^2 R_p^2 C^2)}\right) \tag{3.2}$$

$$i_{AC} = \sqrt{\left(\frac{R_p}{1+\omega^2 R_p^2 C^2} + R_s\right)^2 + \left(\frac{\omega R_p^2 C}{1+\omega^2 R_p^2 C^2}\right)^2}\; V_{AC}, \tag{3.3}$$

formulas that can be deduced with standard circuit theory but that involve too many unknowns (R_p, R_s and C) to allow for an extraction of C from the two measured parameters (ϕ and i_{AC}). One way to work around this problem is to measure ϕ and i_{AC} at various frequencies, in which case the technique would be called impedance spectroscopy. Another method is to use lower frequencies for the applied AC voltage. Since R_p is usually much higher than R_s, and for a low enough frequency the reactance of the capacitor will also be much higher than R_s, one can ignore the series resistance. Setting R_s to zero in the equations above, one obtains two equations with two unknowns, which are then manipulated to give the desired value of C. Mathematically, R_s can be ignored in the denominator of Eq. (3.2) and in the first term inside the square root of Eq. (3.3) if

$$\omega \ll \frac{1}{R_p C}\sqrt{\frac{R_p}{R_s} - 1} \tag{3.4}$$

In our measurements this simpler method was enough to obtain meaningful information from C-V curves.

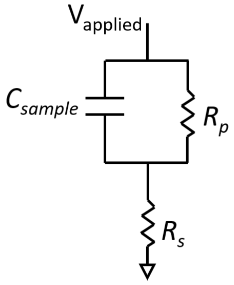

Figure 3.7: Electrical model for extracting the capacitance of a sample with series and shunt resistances.

3.5.3 External Quantum Efficiency

This technique is used only in complete solar cells. External Quantum Efficiency (EQE) is defined as the number of electron-hole pairs collected by the cell's terminals divided by the number of photons incident on the cell for a given wavelength. It is obtained by shining a light with known intensity, I, on the solar cell and measuring the current i that it produces. This measurement is performed for each point on a wavelength (λ) scan. The EQE is then calculated using

$$EQE = \frac{\#\text{ of ehp produced}}{\#\text{ of incident photons}} = \frac{i/q}{I/(hc/\lambda)} = \frac{hc}{q\lambda}\frac{i}{I} \tag{3.5}$$

where h is Planck's constant, c is the speed of light and q is the proton charge.

A block diagram of the equipment is shown in Fig. 3.8. The light is produced in a Xe lamp and passed through a monocromator, allowing for a wavelength range from 320 nm up to more than a 1000 nm. The light is then chopped at a known frequency fed from a lock-in device. This chopped light produces a current in the cell at the lock-in frequency. The measured current from the cell is then filtered so as to select only the lock-in frequency and eliminate every noise at other frequencies (including the DC current produced from ambient light).

The EQE is a useful technique because, in certain circunstances, it can be seen as a map of recombination rate as a function of depth inside the perovskite. Higher wavelengths are absorbed deeper in the absorber and, therefore, the EQE is influenced more by the recombination rate at the PK's sun-facing interface for higher wavelengths than for lower ones. Analogously, the EQE for lower wavelengths is influenced more by the PK's back interface. In Si solar cells, this principle can be used quantitatively if one also measures the wavelength-dependent reflection coefficient so that the reflected photons

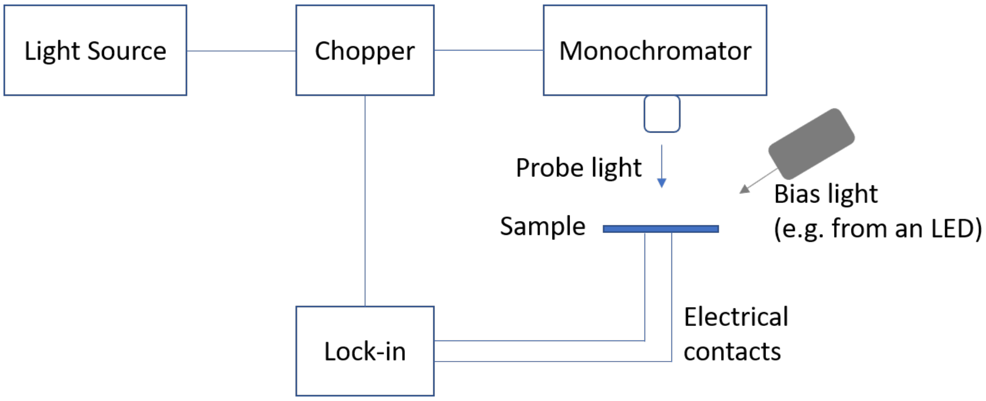

Figure 3.8: Diagram for external quantum efficiency measurement system.

can be accounted for, making the resulting quantum efficiency a direct map of extraction efficiency as a function of the depth at which carriers are generated. However, in the perovskite solar cell case, a quantitative analysis using this principle is complicated because interference effects within the thin films make the generation rate for each wavelength not a perfect exponential decay as a function of depth. In this work, only qualitative analyses of EQE spectra will be presented.

The EQE measurement can also be performed while the cell is biased. In this case it would be a generalization of the J-V curve, because then the $J(V)$ curve could be obtained by integrating the $EQE(\lambda, V)$ in wavelength, weighted by the Sun's spectrum:

$$J(V) = \int_0^\infty d\lambda \; P_{sun}(\lambda) \, \frac{q\lambda}{hc} \, EQE(\lambda, V) \tag{3.6}$$

where P_{sun} is the Sun's AM1.5G spectrum in $\mathrm{Wcm^{-2}nm^{-1}}$. Indeed, this is a useful equipment check between the EQE and J-V measurements, because one can obtain J_{sc} both from the J-V curve and from the EQE measured at 0 V using Eq. (3.6). A discrepancy would indicate that either the J-V or the EQE equipment is miscalibrated (e.g. with a dead lamp).

Even though the EQE can be measured with a voltage bias, usually it is measured at 0 V because the voltage dependence is more conveniently obtained from the regular J-V curve. More useful is the EQE measurement with a background light (also known as bias light). Adding a bias light is useful because it allows to probe the cell's extraction efficiency when it is flooded with carriers (remember that the recombination rate, and therefore the cell's extraction efficiency, might depend on the injection level). Note that the DC current produced by the bias light does not directly influence the current signal because of the lock-in technique, which ignores every frequency in the current signal other than the lock-in frequency. It only influences the measurement indirectly by changing the recombination rate of carriers inside the PK. If the EQE is lower with bias light than without it, it means the cell is less efficient at collecting carriers when there are too many carriers to colect.

3.5.4 Photoluminescence

In photoluminescence (PL), laser light is shone on a material and the re-emitted light from this material is detected, as illustrated in Fig. 3.9. The photon energy from the laser is selected to be higher than the material's bandgap. The emitted light, however, has the energy of the bandgap, because carriers first relax to the bottom or top of their respective bands before recombining radiatively. It is also possible for the material to emit light in energies lower than the bandgap if it has defect levels that allow for radiative transitions. It is important to remember that in PL one is only probing the radiative transitions; carriers might still recombine by other mechanisms and emit no photon. Such recombination events would not be detected by PL.

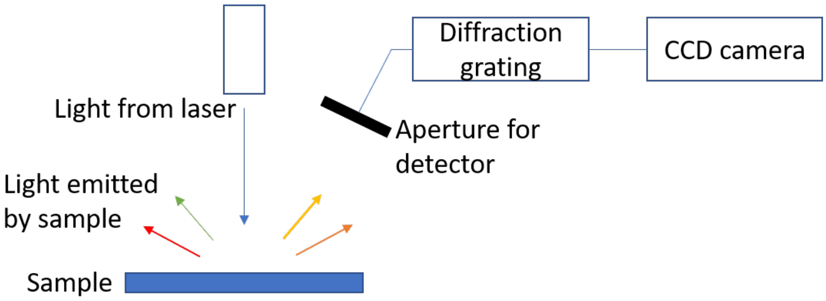

Figure 3.9: Diagram for the photoluminescence measurement system.

This technique is useful for mainly two reasons. First, it allows for a precise measurement of the material's bandgap. In PK research this is very useful because usually it is desired to tune the bandgap to a precise value. Also, it allows for the detection of bandgap shifts that may happen in some PK degradation mechanisms [72] or phase transitions [75]. Second, the PL measurement allows for probing the radiative recombination rate of the material by measuring the intensity of the emitted light. One wants a signal as strong as possible, because a strong PL signal means that non-radiative recombination is lower. This is a common source of confusion, because at first it seems that a strong PL signal would mean that the solar cell is emitting more light, which seems to indicate that it would be less efficient. This is incorrect, because a lower PL signal does not mean that carriers are recombining less, only that they are recombining preferably by non-radiative mechanisms, such as defect recombination. But defect recombination is avoidable in principle, while radiative recombination is not. Therefore, it is desired to have carriers recombining only by the radiative mechanism and eliminate non-radiative recombination as much as possible. This means that it is preferred to have a PL signal as high as possible.

Most PL setups (the one used in this work included) only measure a portion of the light emitted by the material, namely that which is emitted in the direction of the detector (see Fig. 3.9). This means that it is only possible to compare the PL signal between different PL measurements, because to probe the actual recombination rate in the material it would be necessary to detect all photons that are emitted in each direction.[6]

---

[6] Such setups do exist, however, and the technique is called absolute PL. For this measurement, an integrating sphere is used to collect all photons emitted by the material. Recently, absolute PL measurements have appeared in PK research to probe the quasi-Fermi level splitting inside the PK

We mention that in some cases the laser probe used in PL can damage the PK by heating. In these cases, it is necessary to reduce the laser intensity (with filters) or the integration time so that a reproducible measurement is obtained. In our measurements, we found that a laser intensity of 1 Sun (i.e. 100 mW/cm^2) and an integration time of 10 s was sufficient for a clean signal with no layer degradation.

3.5.5 Lock-in Thermography

Thermography is a useful technique to probe the lateral homogeneity of the layers in a solar cell [147]. Here, a known electric current is passed through the cell (usually in the dark), so that the cell warms up by Joule heating. An infrared camera then takes images of the temperature distribution on the cell area, which give information on how uniform the cell is. If there is a local shunt, for example, this region will conduct more current, heat more and be detected in the image. Even without shunts, this technique is useful to probe possible inhomogeneities in performance along the cell area; regions with lower V_{oc}, for instance, conduct more current for a given applied voltage, and therefore heat more than regions of higher V_{oc}.

One drawback of the technique is thermal blurring. High temperature regions dissipate heat to low temperature regions. Furthermore, a few tens of seconds of integration time are necessary to acquire an image with enough resolution. This means that it is necessary to wait for steady-state conditions before taking the image, but by then the contrast between the hot and cold regions will be mostly lost. This problem is circumvented using the lock-in technique. In this case, the probing current is oscillated with a known frequency (in this work, always 25 Hz), making the sample heat and cool at this same frequency. With an alternating heating profile the heat has less time to propagate and less thermal blurring results. The images obtained with the camera are analysed only at the lock-in frequency.

3.6 Simulations

Simulating I-V curves of solar cells is a helpful technique to identify the causes of inefficiencies in the device. It also gives insights on the working mechanisms of solar cells. To simulate the I-V curve of perovskite solar cells we uses SCAPS [148], an open source software created to simulate III-V solar cells such as CdTe. These solar cells are also made of thin films stacked on one another, also have direct bandgap absorbers and also take advantage of band misalignments between layers for device improvement, so they are similar in principle to PK solar cells. Indeed, there are publications that use this software to predict the behavior of PK solar cells [120]. SCAPS solves Eqs. (2.3) using the models described in the previous chapter using a finite elements numerical approach.

---

caused by light [138]. This is a very useful technique, because it can be performed in a single layer (not the complete device) and still give the implied V_{oc} that the cell would have with that layer as the absorber. (Remember that V_{oc} is equal to the quasi-Fermi level splitting between the two contacts.) After completing the device and measuring the V_{oc} with the IV curve, one can compare this V_{oc} with that implied from absolute PL and infer how much recombination was added by the layers adjacent to the PK.

We do not use SCAPS to fit experimental curves against models. Such fitting procedures cannot be performed because the models usually have too many free parameters, so the value obtained for any single parameter of a model is too dependent on the remaining model parameters, which are not very precisely measured themselves. This problem renders this method of analysis useless. Instead, we use SCAPS to show that a given model is consistent with the experimental results within the range of plausible model parameters.

Tab. 3.4 shows the parameters that must be set in order to perform simulations with this solar cell model. Some of the parameters were kept fixed in all simulations made for this work, while others were varied to illustrate a particular change in solar cell behavior when a particular variable is varied. The cell structure has five layers (the two contacts, the HTL and ETL and the perovskite) and two relevant interfaces (PK/ETL and PK/HTL). The model assumes:

- a non-uniform carrier generation profile caused by interference effects of the incident light (solved using the transfer matrix method);
- both radiative and SRH recombination (with a single midgap defect level) mechanisms in the bulk of the PK and at the interfaces with ETL and HTL;
- possibly different valence and conduction band energy levels for each layer;
- a Tauc model for the absorption coefficient dependence on wavelength for each layer;
- possible non-uniform doping profiles;
- and a thermionic emission model for the metal-ETL and metal-HTL contacts.

SCAPS does not take into account ionic conduction. This means that it is not possible to predict some of the effects (e.g. hysteresis) on the experimental J-V curves with this software. However, if the J-V scan is performed at a fast enough rate [143], the mobile ions do not have time to move and it is possible to model them as regular non-mobile dopants, as Jacobs et al. [120] have shown. In SCAPS, this simulation can be performed by adding non-uniform doping profiles to the perovskite layer. This workaround provides a method to interpret hysteresis effects on the IV curve, although it cannot be said that the model predicts such effects.

Layer	Parameter	Value
ETL	Thickness	20 nm
	Bandgap	3.2 eV
	Electron Affinity	4.0 eV
	Relative dielectric constant	2.5
	CB density of states	2.2×10^{18} cm^{-3}
	VB density of states	1.8×10^{19} cm^{-3}
	Electron mobility	10^{-1} cm^2/Vs
	Hole mobility	10^{-4} cm^2/Vs
	Doping density	$N_D = 10^{20}$ cm^{-3}
PK	Thickness	500 nm
	Bandgap	1.55 eV
	Electron Affinity	4.0 eV
	Relative dielectric constant	10
	CB density of states	10^{19} cm^{-3}
	VB density of states	10^{19} cm^{-3}
	Electron mobility	10 cm^2/Vs
	Hole mobility	10 cm^2/Vs
	Doping density	$N_A = 10^{17}$ cm^{-3}
	Radiative recombination coefficient	$B = 6 \times 10^{-11}$ cm^{-6}
HTL	Thickness	20 nm
	Bandgap	2.5 eV
	Electron Affinity	3.0 eV
	Relative dielectric constant	9
	CB density of states	10^{19} cm^{-3}
	VB density of states	10^{19} cm^{-3}
	Electron mobility	10^{-4} cm^2/Vs
	Hole mobility	1 cm^2/Vs
	Doping density	$N_A = 10^{20}$ cm^{-3}

Table 3.4: Parameters used in SCAPS to perform simulations of PK solar cells. The parameters were taken either from literature on perovskite materials research or were guesses as typical values.

Chapter 4

Results

In this chapter we will give the results obtained for different layers and device architectures. First, we will concentrate on the characterization of devices containing only one of the active layers of the complete cell, giving insight to the characteristics of each layer before analyzing their integration in the complete devices. Then we will analyze the performance of complete solar cells. Finally, we will present results on the investigation of reverse bias instabilities in our devices.

4.1 Substructures

4.1.1 FTO/TiO_2/Al Devices

In these structures, the Al electrodes were deposited by evaporation as disks of 100 μm diameter and $\sim$ 500 nm thickness thorough a shadow mask. Thus, each 2.5 x 2.5 cm^2 substrate had hundreds of devices.

Fig. 4.1 shows ten J-V curves for different FTO/TiO_2/Al devices of the same substrate, the TiO_2 being deposited by spin-coating. The spread in conductivity is supposed to be caused by the porosity in the TiO_2 film (which is known to be present from ellipsometry measurements), which may allow the top Al contact to percolate throughout the titania film. We thus postulate that the porosity in the layer allows for different amounts of shunting of the Al disks, giving different measured resistances for each disk. Indeed, the upper most curve in Fig. 4.1 corresponds to a resistance of 100 Ω, which is almost the resistance measured for the FTO alone. On the other hand, the lowest curve clearly presents a non-ohmic behavior, which is typical of titania [142, 149, 150]. We will use this curve to obtain estimates for the conductivity of the TiO_2 layer by assuming that no shunting is present for this particular Al disk.

The non-ohmic behavior is not caused by interface-limited conduction since FTO and Al both make ohmic contacts to TiO_2 and, indeed, the observed dependence is not exponential as would be expected for Schottky contacts. Instead, we identified this non-linearity with the space-charge-limited current (SCLC) mechanism, which has been reported by other authors in studies of conduction in bulk TiO_2 [149, 150]. Briefly, it is caused by the low conductivity of TiO_2 but easy electron injection, causing the current to be conducted by the very electrons that were injected instead of the electrons instrinsic to titania [151]. The equations for this mechanism give a transition from ohmic to quadratic

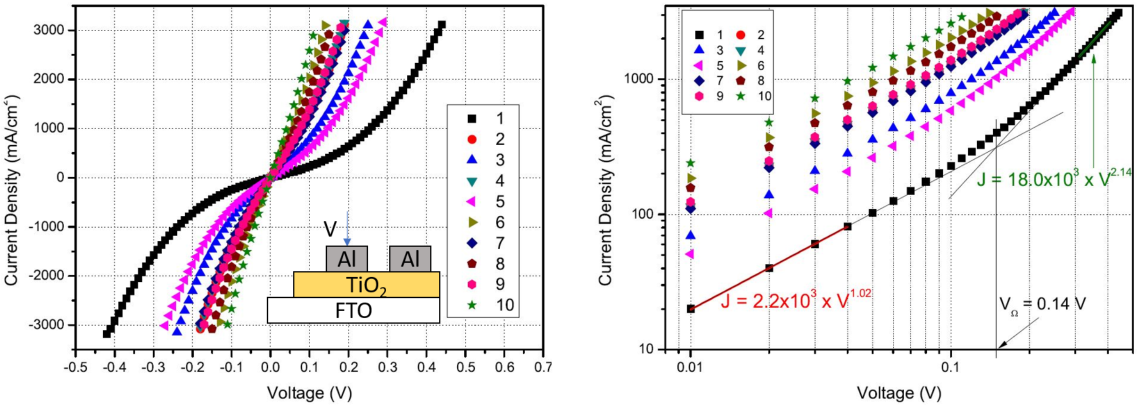

Figure 4.1: Ten I-V curves for FTO/TiO_2/Al structures on the same substrate in linear (left) and log-log (right) scales. The equations are for power law fits in the regions indicated.

behavior, which is observed in Fig. 4.1. For the ohmic part, we have

$$J = \frac{\sigma}{d} V \tag{4.1}$$

where σ is conductivity, d is thickness and V is voltage. For the quadratic part the SCLC theory gives [151]

$$J = \frac{9}{8}\frac{\epsilon\mu}{d^3} V^2 \tag{4.2}$$

where ϵ is the film's static dielectric constant and μ is the mobility. The transition from linear to quadratic dependence occurs at a voltage V_Ω obtained by equating Eqs. (4.1) and (4.2), giving

$$V_\Omega = \frac{8}{9}\frac{qd^2}{\epsilon} n_0 \tag{4.3}$$

where q is the proton charge and n_0 is the intrinsic carrier concentration of the TiO_2 layer.

From the linear coefficient in Fig. 4.1b and using $d = 20$ nm, we obtain a conductivity of $4.1 \times 10^{-6}\ \Omega^{-1}\text{cm}^{-1}$. From the transition voltage and using $\epsilon = 31 \times \epsilon_0$ (cf. Sec. 4.1.2), we obtain a free carrier concentration of $n_0 = 7.7 \times 10^{17}$ cm^{-3}, which combined with the conductivity gives a mobility of $\mu = 3.4 \times 10^{-5}$ cm^2/Vs. The conductivity may seem too low for photovoltaic applications, but note that the resistance is also low because the layer is only 20 nm thick. Since the current that a perovskite solar cell produces is ≈ 20 mA/cm^2, the voltage drop in the TiO_2 during operation is ~ 0.01 V (Fig. 4.1b). The voltage that the cell produces is ~ 1 V, so the series resistance added by the TiO_2 layer reduces the voltage of the cell by about 1 %.

4.1.2 Si/TiO_2/Al Devices

Si/TiO_2/Al structures behave differently if the Si is p-type or n-type. Consider first the p-type case (with doping density of $N_A = 2 \times 10^{14}$ cm^{-3}). The J-V curves are shown in Fig. 4.2. The work function of Al is 4.0 eV and that of Si can be calculated from

$$\phi_F = kT \ln(N_A/n_i) \tag{4.4}$$

where ϕ_F is the Fermi level and $n_i = 10^{10}$ cm^{-3} is the intrinsic carrier concentration of Si at 300 K. This gives a difference in workfunction between the metal and the Si of 0.8 eV, giving rise to a barrier for electron flow from Al to Si and to the diode behavior observed in Fig. 4.2, where the voltage in the x-axis is the voltage applied in the Al contact while the Si contact is held at ground.

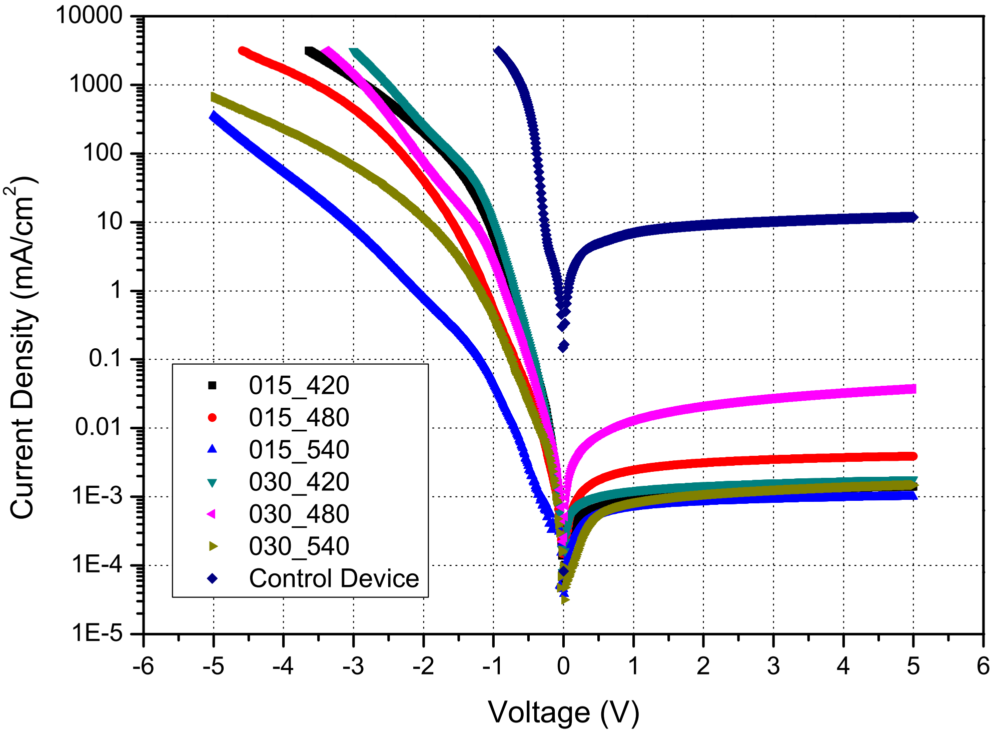

Figure 4.2: Typical J-V curves for p-Si/TiO2/Al samples fabricated with different precursor concentrations (0.15 M and 0.30 M) and sintered at different temperatures (420 °C, 480 °C and 540 °C). The control device has no TiO_2 layer, just p-Si/Al.

The most important conclusion obtained from this result is that TiO_2 is indeed not able to conduct holes because, if it was, positive voltages in Al would lead to hole injection in Si and a high current, but instead the structure is rectifying for positive voltages. Note that even the control structure without TiO_2 (where Al is deposited directly onto the p-Si) is rectifying, as it should since Al is a low work function metal and the substrate is p-type. But the reverse current for this structure is at least three orders of magnitude higher than those of the TiO_2 containing devices, meaning TiO_2 is effectively passivating the Si surface and reducing the amount of injected holes [135].

C-V curves for typical samples of Al/TiO_2/p-Si capacitors are shown in Fig. 4.3, in this case deposited in the regime 0.30 M and 480 °C. We observed an apparent dependence of the oxide capacitance with frequency. This is an artifact caused by the relatively high conductance (when compared, for example, with SiO_2 MOS capacitors) of our samples for negative voltages. As explained in Sec. 3.5.2, using lower frequencies is a method of correcting this artefact. Indeed, the capacitance for the lower frequencies of 10 kHz and 100 kHz approach the value of 525 pF. The relative dielectric constant associated to this capacitance is $\epsilon/\epsilon_0 = Cd/A = 31$, which is in agreement with reported values for TiO_2 deposited from this route [152].

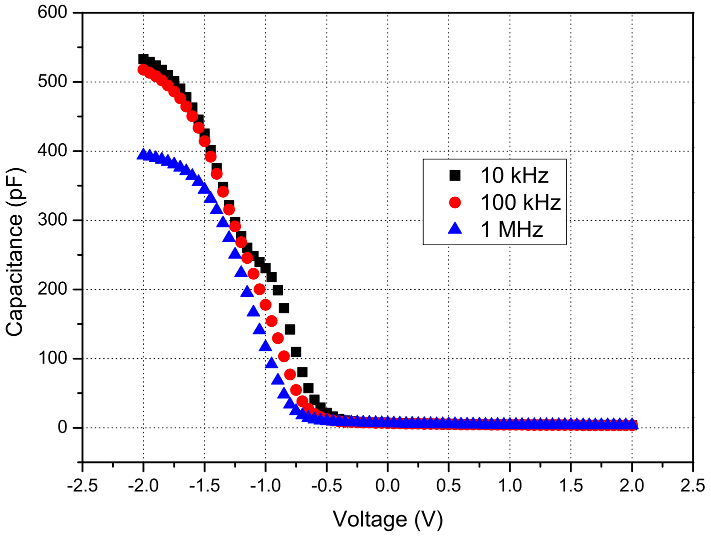

Figure 4.3: Typical capacitance-voltage curves for p-Si/TiO_2/Al structures measured at different frequencies. The shoulder observed in the 10 kHz curve is caused by defects at the TiO_2/Si interface.

For n-Si the structure behaves very differently [142], because this time the wafer is a conductor of electrons (as is TiO_2) and therefore one expects high current. The J-V curve for a typical n-Si/TiO_2/Al structure is shown in Fig. 4.4 for both forward bias (i.e. positive on Al) and reverse bias (negative on Al). Indeed, this structure is more conducting than with p-Si and it presents a linear to quadratic transition as would be expected for the SCLC mechanism, at least for forward bias. But for negative voltages in Al the current suddenly saturates at around 0.65 V, which was unexpected at first. We have published an explanation for this effect in Ref. [142], which we now explain.

For the case where TiO_2 is contacted by FTO and Al (i.e. low workfunction metals), the device has both capacitive characteristics (because it is a dielectric material sandwiched by conductive layers) and resistive characteristics (because there is charge transport through TiO_2 since it is not completely insulating). The SCLC mechanism explains this behavior [151]: since the mobility and carrier concentration in TiO_2 are relatively low, for a not-too-high applied voltage the injected carriers from the contacts will dominate over the carriers that were intrinsic to TiO_2.[1] In this regime, there is an appreciable space-charge accumulated inside the TiO_2 caused by these injected electrons. This space-charge is linearly dependent on the applied voltage, and in this sense the structure resembles a capacitor. The difference from a regular capacitor, besides the very

---

[1] The current in SCLC is quadratic because the amount of injected carriers grows linearly with V, and also the field that pushes the electrons grows linearly with V.

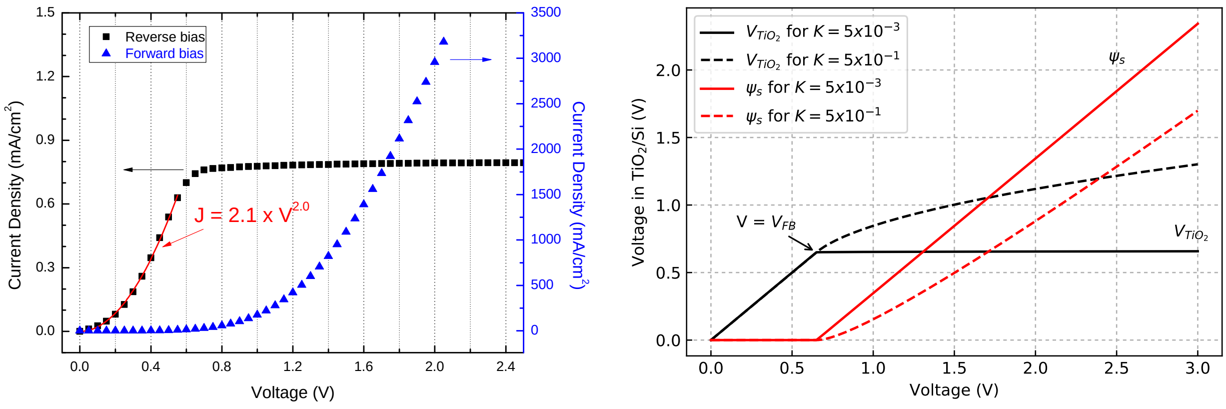

(a)

(b)

Figure 4.4: a) Typical J–V behavior of an Al/TiO$_2$/n-Si structure showing a current "saturation" for reverse biases higher than ≈ 0.65 V (negative in aluminum). The equation is for a power law fit in the region before saturation. b) Plot of voltage drop in TiO$_2$ and in Si versus applied voltage (in reverse bias) for $K = 5 \times 10^{-3}$ V$^{1/2}$ (solid lines) and $K = 5 \times 10^{-1}$ V$^{1/2}$ V$^{1/2}$ (dashed lines), where $K \equiv (8d/9\epsilon_t)\sqrt{2\epsilon_s q N_D}$.

high leakage current, is that the charge is not accumulated in one of the capacitor plates but instead is distributed throughout the titania.

Now, consider again this leaky capacitor structure but with n-type Si instead of a metal as one of the contacts and Al as the other electrode. For no applied voltage, the semiconductor surface is in accumulation, caused by the metal-semiconductor work function difference and some amount of fixed positive charges in titania. The flatband voltage [116], V_{FB}, is negative:

$$V_{FB} = \phi_m - \phi_s - \frac{Q_f}{C_{ox}} < 0 \tag{4.5}$$

because the metal work function, ϕ_m, is lower than that of the semiconductor, ϕ_s, and because the oxide charges in the film, Q_f, are positive. C_{ox} is the oxide capacitance. Now, if a negative voltage lower in magnitude than V_{FB} is applied in Al with respect to Si, electrons will start to flow via the SCLC mechanism, but the semiconductor surface will remain in accumulation. Since in accumulation the charge in Si varies as $\exp(\psi_s)$, where ψ_s is the voltage drop in Si, and the charge in TiO$_2$ varies as V_{TiO_2} , where V_{TiO_2} is the voltage drop in the film, charge neutrality in the device dictates that most of the applied voltage will drop in the oxide. In this case the current through the device is given by an SCLC power law $J \sim (V_{TiO_2})^n$, where $n \geq 2$ depending on the distribution of defects in titania. This is the observed dependence for voltages less than the voltage at which the current is truncated, as shown by the power law fit in Fig. 4.4.

For applied voltages higher than V_{FB}, a depletion layer containing positive charges will start to build up in Si to balance the negative charges accumulated in titania and maintain charge neutrality. This time, however, a significant voltage drop in Si will result, because in depletion $Q_d \sim \sqrt{\psi_s}$, where Q_d is the positive charge in the depletion region, while the charge in titania is still given by $Q_t \sim V_{TiO_2}$, where Q_t is the negative charge distributed in the film. Using the charge neutrality condition one can obtain V_{TiO_2} and ψ_s:

$$\begin{aligned} Q_t &= Q_d \\ \frac{9}{8}\frac{\epsilon_t A}{d} V_{TiO_2} &= A\sqrt{2q\epsilon_s N_D \psi_s} \\ V_{TiO_2} &= K\sqrt{\psi_s} = K\sqrt{V - V_{FB} - V_{TiO_2}} \end{aligned} \tag{4.6}$$

where q is the proton charge, ϵ_s (ϵ_t) is the static dieletric constant of Si (TiO_2), A is the electrode area, d is the film thickness and $K \equiv (8d/9\epsilon_t)\sqrt{2\epsilon_s q N_D}$. The factor of 9/8 comes from the fact that the negative charge of the capacitor is not concentrated in a plate but instead is distributed throughout a volume, making the average distance between the two plates of the capacitor slightly smaller and the capacitance slightly larger [151]. Solving Eq. (4.6) for the voltage in TiO_2 and in Si, one obtains

$$V_{TiO_2} = \frac{K^2}{2}\left(\sqrt{1 + 4\frac{(V - V_{FB})}{K^2}} - 1\right) + V_{FB} \tag{4.7}$$

$$\psi_s = \frac{K^2}{2}\left(1 + 2\frac{(V - V_{FB})}{K^2} - \sqrt{1 + 4\frac{(V - V_{FB})}{K^2}}\right) \tag{4.8}$$

Note that Eqs. (4.7) and (4.8) are only valid for voltages higher in magnitude than the flatband voltage. Overall, $V_{TiO_2} \approx V$ and $\psi_s \approx 0$ for $|V| < |V_{FB}|$ and $V_{TiO_2} \sim \sqrt{V}$ and $\psi_s \sim V$ for $|V| > |V_{FB}|$. The resulting behavior is plotted in Fig. 4.4b for $K = 5 \times 10^{-3}$ $V^{1/2}$, a value obtained using $\epsilon_s/\epsilon_0 = 11.7$, $\epsilon_t/\epsilon_0 = 30$, $d = 20$ nm and $N_D = 2 \times 10^{14}$ cm^{-3}.

This explains why the current through the structure saturates. Once the flatband voltage is reached, the "excess voltage" $V - V_{FB}$ will stop being mostly dropped in the film because of the formation of a depletion region, and the current will stop increasing. Additionally, from Eq. (4.6) and the low value of $K \sim 10^{-3}$ one can see that the excess voltage drop in titania is actually negligible in comparison to that in silicon (at least three orders of magnitude lower) after the depletion layer starts to build up. This is why V_{TiO_2}, and consequently J, becomes constant beyond $V = V_{FB}$. The structure then behaves as a current source. Note that for higher values of K the voltage drop in titania could become appreciable even when the semiconductor is in depletion, as shown in Fig. 4.4b for a higher value of $K = 0.5$ $V^{1/2}$. Higher values of K could be obtained with higher doping levels of the semiconductor or with films with lower dielectric constants and higher thicknesses.

One might expect that at the onset of strong inversion the depletion layer width should stop increasing and the current should start increasing again. However, we argue that strong inversion is actually never reached in this structure. This is because the amount of electrons injected from Al through the titania is many orders of magnitude larger than the amount of holes thermally generated forming the inversion layer. Even if the lifetime in Si is as low as 1 μs, a simple estimation [116] puts the generation current at about 10^{-4} $mAcm^{-2}$, which is still at least three orders of magnitude lower than the truncated current observed in Fig. 4.4a. This means that holes recombine with the injected electrons before they can form the inversion layer, and the semicondutor is kept in deep depletion.

To confirm these hypotheses, we show in Fig. 4.5 the region of interest of a typical capacitance–voltage (C–V) curve for this structure measured at 1 kHz. A low frequency is necessary to avoid errors caused by the high conductance of our samples. [146] The Debye length for our Si substrate is [116] $L_D = \sqrt{kT\epsilon_s/N_D q^2} = 289$ nm, corresponding to a capacitance of $\epsilon_s A/L_D = 11.3$ pF, and the measured oxide capacitance (not shown) is $C_{ox} = 400$ pF, giving a capacitance at flatband, C_{FB}, of

$$C_{FB} = \left(\left(\frac{\epsilon_s A}{L_D}\right)^{-1} + C_{ox}^{-1}\right)^{-1} \approx 10 \text{ pF}. \tag{4.9}$$

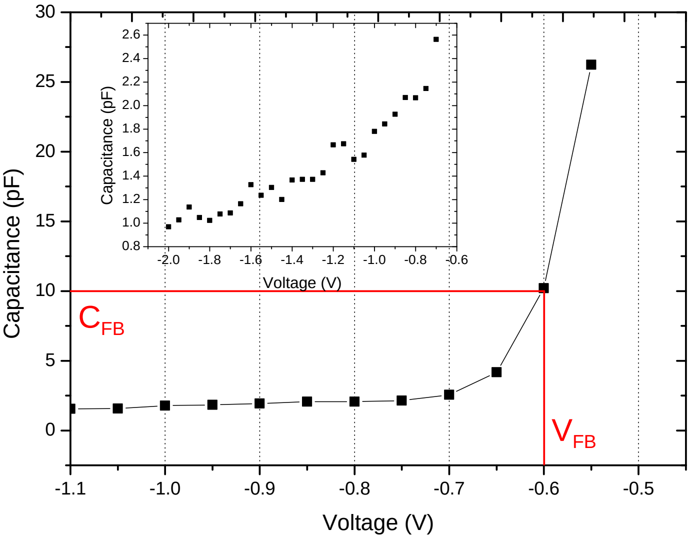

Figure 4.5: Portion of the C–V curve of Al/TiO2/n-Si structures showing the flatband capacitance at $V \approx 0.6$ V. The inset shows the deep depletion region of the same plot.

In the C-V curve this capacitance corresponds to 0.6 V, in very good agreement with the voltage at which current saturation occurs in Fig. 4.4a. It is noted that the flatband capacitance is almost equal to the minimum capacitance because of the low doping in these samples, which gives a relatively high Debye length. The hypothesis of deep depletion can also be confirmed from the C–V curve for voltages higher in module than 0.7 V, as shown in the inset of Fig. 4.5. The voltage at which strong inversion should occur is [116]

$$V_{FB} - \frac{A\sqrt{2\epsilon_s q N_D 2\phi_F}}{C_{ox}} - 2\phi_F = -1.1 \text{ V} \tag{4.10}$$

where $\phi_F = kT/q \ln(N_D/n_i)$ and n_i is the intrinsic carrier concentration in Si. However, the capacitance continues decreasing for higher voltages (in module), in agreement with the deep depletion hypothesis.

It was also found that the saturation current can be reproducibly controlled by changing the precursor concentration and the annealing temperature of titania. In Fig. 4.6 we show six J-V curves for films annealed in O_2 at three different temperatures (420, 480 and 540 °C) and deposited with two different concentrations of the organometallic precursor (0.15 and 0.30 M). The dependence is quite clear: higher annealing temperatures and higher precursor concentrations lead to lower saturation currents. At first, one might try to explain this dependence with the presence of a SiO_2 layer grown during the annealing step. However, note that a temperature of 540 °C is too low to grow a significantly thick SiO_2 layer. We therefore expect that the thickness of the interfacial layer is that of a native oxide independently of temperature, which means it cannot be the cause of different saturation currents for different samples. Instead, this phenomenon can be explained from the fact that higher temperatures and concentrations lead to more oxygen concentration and less organic content in the films [153]. A higher concentration of oxygen translates to a lower electron affinity and a higher band gap [104], leading to a higher barrier for electron injection from Al to Si and, therefore, less current. Even a 0.1 eV increase in the barrier height can change the current by almost two orders of magnitude because $\exp(-0.1q/kT) = 0.02$ (assuming a thermionic emission model). This means that the change in barrier height that produces the changes between the lowest and the highest curves in Fig. 4.6 is of order 0.1 eV. One must also note that the thickness and dielectric constant of the oxide may be different for different deposition conditions [152], changing the value of K. In particular, for the deposition at concentration of 0.15 M and annealing temperature of 540 °C a slight linear increase of the "truncated current" as a function of voltage is observed. We suppose this is a consequence of a higher K value obtained for this film. This increase in K results in a square-root dependence of the voltage drop in titania with respect to the applied voltage (dashed lines of Fig. 4.4b), but since the SCLC mechanism gives a square-law J-V dependence, the resulting behavior is approximately linear, as observed.

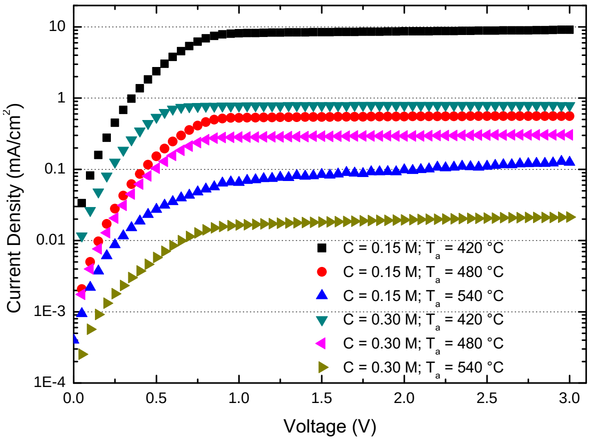

Figure 4.6: J-V curves of Al/TiO_2/n-Si structures for different deposition conditions. In the legend, C is the organometallic precursor concentration and T_a is the annealing temperature.

The structure also presented a photoconductive effect, as shown in Fig. 4.7. Here light is absorbed solely by Si, because the absorption edge of TiO_2 is at about 390 nm (gap is $\sim$ 3.2 eV) and the lamp we used in the photoconductance experiments was an incandescent lamp that produced only $\sim$ 2 mW/cm^2 of irradiance at the sample. The J-V response is only affected by light in the saturation part. This is because before saturation there is no depletion region to separate electrons and holes created by light. Instead, the photoelectrons and holes recombine before they can be collected by the terminals and constitute a photocurrent. On the other hand, once the flatband voltage is reached, a depletion region starts to set in, carriers begin to be separated and a photocurrent is created. We also note that when light is present the "saturation" current increases with increasing voltage (see the inset of Fig. 4.7). This can also be easily accounted by our model. For increasing voltage, the depletion region width grows and more photoelectrons and holes are collected, giving more photocurrent. Because strong inversion is never reached, the depletion region keeps growing indefinitely as long as the voltage is increased. These effects further confirm our model.

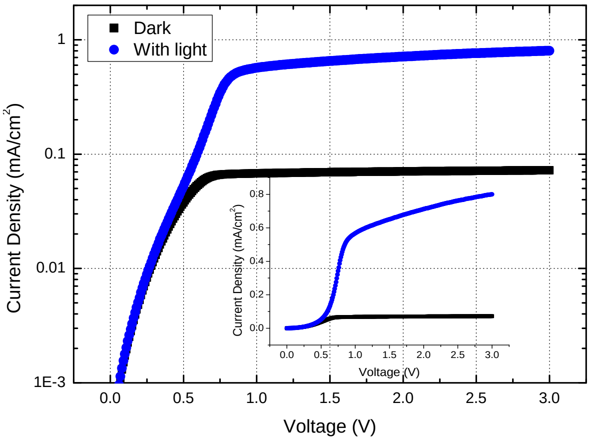

Figure 4.7: Photoconductive effect for Al/TiO$_2$/n-Si structures. The illumination is from an incandescent lamp that produced $\sim$ 2 mW/cm^2. This particular sample was produced with concentration of 0.15 M and annealing temperature of 540 °C. The inset shows the same plot in linear scale.

4.1.3 ITO/P3HT/Al and Al/P3HT/Al

In Fig. 4.8 we show J-V curves of both Al/P3HT/Al and ITO/P3HT/Al structures. These curves were taken in the dark and inside a metallic box to shield the sample from radiation with frequencies up to X-rays. Two unexpected phenomena are observed: a discontinuity at $V = 0$ V and a short-circuit current. Upon further investigation using C-V measurements, we have concluded that both phenomena are consequences of the slow movement of ionic charges inside P3HT. Although interesting, these effects are not of concern to solar cells and thus will not be discussed further.

More relevant to solar cells, the J-V curve for Al/P3HT/Al indicates that P3HT is capable of blocking electrons and only conducts holes, since, in this case, aluminium, which has a low work function, should make a Schottky contact when deposited in P3HT, which is indeed the observed behavior. Therefore, P3HT may act as an HTL. In Fig. 4.8 it is also shown the case in which the bottom contact is ITO. Having a slightly higher work function, ITO provides a slightly lower barrier for hole injection and allows a larger current through P3HT when the ITO contact is positively biased with respect to Al.

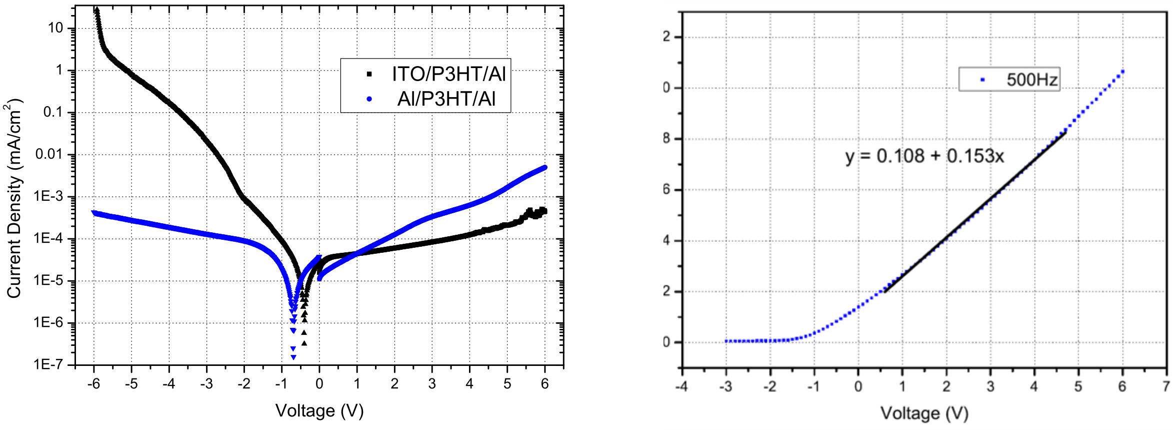

(a) (b)

Figure 4.8: J-V curves for ITO/P3HT/Al and Al/P3HT/Al samples.

We also probed the hole concentration of P3HT using C-V measurements in the structure ITO/P3HT/Al, as shown in Fig. 4.8b. Since this structure behaves like a diode, in reverse bias (i.e. positive on Al) the capacitance is given by

$$\frac{1}{C^2} = \frac{2(V - V_{bi})}{q\epsilon N_A} \tag{4.11}$$

A linear fit of $1/C^2$ vs V, shown in Fig. 4.8b, gave $N_A = 2.8 \times 10^{17}$ cm^{-3} for the concentration of holes. Assuming a mobility of about 10^{-4} cm^2/Vs [154], a conductivity of about 5×10^{-6} Ω^{-1}cm^{-1} is obtained, which is similar to that of TiO_2. Therefore, a similar series resistance is introduced by the P3HT when used in the perovskite solar cell.

4.2 Complete Solar Cells

4.2.1 ITO/NiO/Perovskite/LiF/C_{60}/Ag

We begin by showing, in Fig. 4.9, the J-V curves (both forward and reverse scans) and statistics on the first batch of working solar cells made by the author. The perovskite used in this batch was $(FAPbI_3)_{0.87}(MAPbBr_3)_{0.13}$, with a bandgap of 1.58 eV. The J-V curves are from the best-performing cells of the batch, while the statistics show the J-V parameters extracted from the J-V curves of all minimally-working cells in the batch. (We will define minimally-working in this thesis as cells with at least 0.5 V in V_{oc}, 10 mA/cm^2 in J_{sc}, 0.3 in FF and 5 % in efficiency.) This batch was meant as a test on the sensitivity of cell performance on the perovskite layer deposition technique, in particular how the antisolvent is applied during spin-coating.

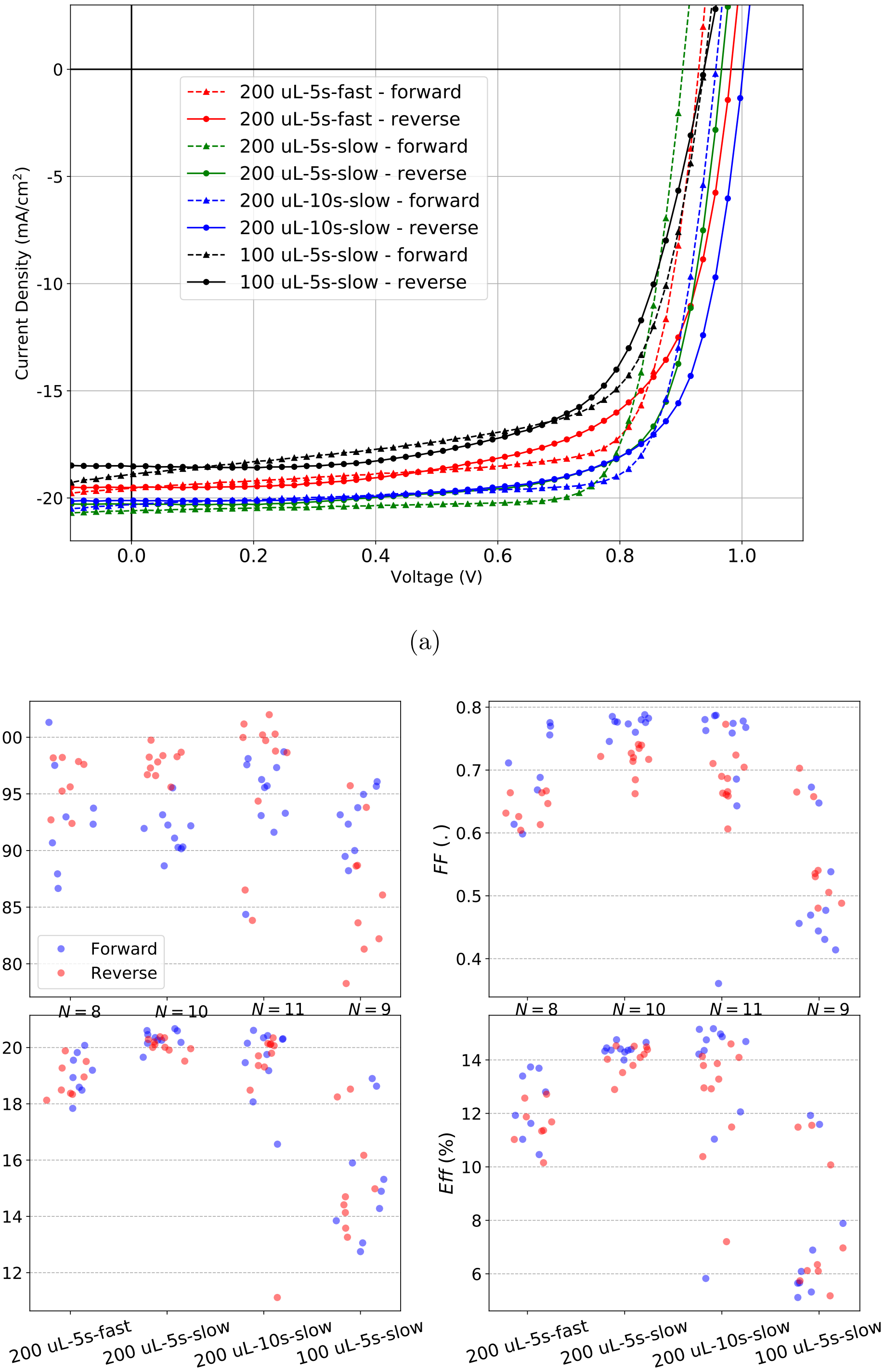

(a)

(b)

Figure 4.9: a) I-V curves of best solar cells with different anti-solvent treatment procedures. b) Distribution of IV parameters for all minimally working solar cells from this batch. Blue dots correspond to forward IV scans and red dots to reverse IV scans.

The substrates were grouped in four different categories (100 μL-5s-slow, 200 μL-5s-fast, 200 μL-5s-slow, 200 μL-10s-slow) depending on the volume of antisolvent used, how many seconds before the end of spin-coating it was applied and the speed with which the antisolvent was forced out of the pipette. All other layers and deposition procedures were equal for all cells.

This batch started with 16 substrates with 3 solar cells each, for a total of 48 solar cells (12 cells per group). As shown in Fig. 4.9, not all cells end up as minimally-working devices; group 100 μL-5s-slow ended with 9 working cells, 200 μL-5s-fast with 8, 200 μL-5s-slow with 10 and 200 μL-10s-slow with 11. Also, an appreciable spread in performance is seen for all groups. Nevertheless, trends can be noticed between the groups. In particular, the deposition with 200 μL-5s-slow had the highest efficiency cells and the lowest spread in performance across different cells, specially compared to the groups 200 μL-5s-fast and 100 μL-5s-slow. The difference in performance for the different groups is likely a consequence of different thicknesses and grain sizes for the resulting perovskite layer, because if the antisolvent is applied too soon and/or too fast, the PK solution might be washed away with the antisolvent during spinning, resulting in a too thin layer. If too little solution is used, a similar result is obtained, except that it is caused by not enough precipitation of the PK solution caused by not enough antisolvent applied. For our deposition conditions, we found that 200 μL of antisolvent gently applied 5 s before the end of spin-coating was the optimized technique, and this recipe was followed in all subsequent batches. These results show that cell performance can be very sensitive even to the slightest changes in spin-coating conditions and that it is imperative that the user takes great care in standardizing its technique to improve reproducibility.

To gain insight on the working principles of the perovskite solar cell, a typical device from this batch will be analyzed separately. The J-V curves (forward and reverse) of this cell are plotted in Fig. 4.10a. In Fig. 4.10b we show several simulations of J-V curves made with SCAPS, including a simulated structure that mimics the real cell's idealized structure. In this idealized scenario, the thicknesses of the layers are those of the real device, but there are no defects that cause recombination in the perovskite or at its interface with the ETL and HTL. The only recombination mechanism is radiative with a coefficient (see Eq. (2.5)) of $B = 6 \times 10^{-11}$ cm^{-6}, a value taken from Ref. [155]. The mobilities and doping densities of the ETL and HTL are chosen such that electron and hole selectivities are perfect and no series resistance is introduced.

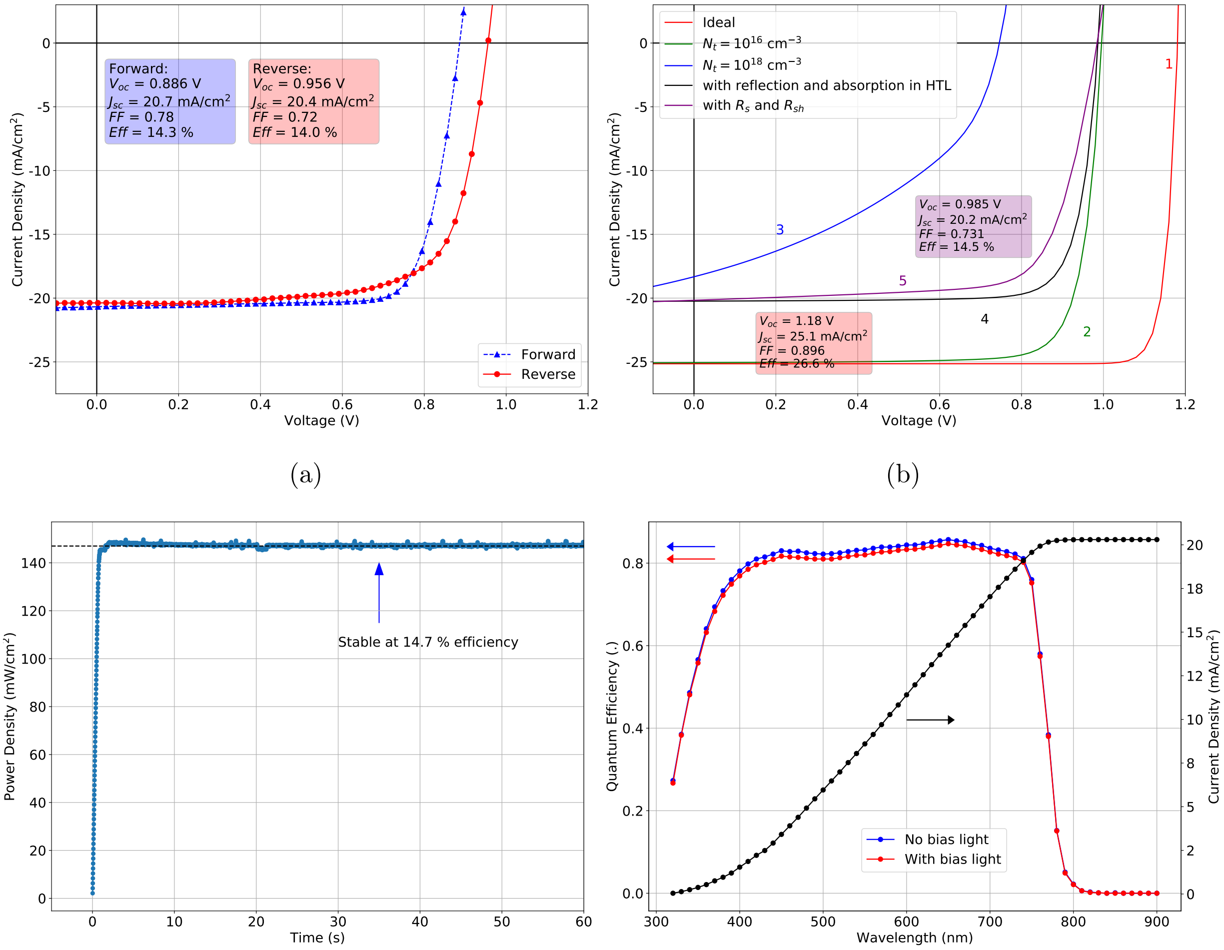

(a)

(b)

(c)

(d)

Figure 4.10: a) I-V curves (forward and reverse scans) of best solar cell in this batch. b) Simulations of I-V curves for cell structure having different defect densities, different amounts of parasitic absorption in the HTL and different series and shunt resistances. c) Maximum power point tracking curve for the same cell in a). d) External quantum efficiency and integrated current obtained from the EQE for the same cell in a).

Clearly, the real structure is far from ideal, since all measured J-V parameters are lower compared to curve 1 of Fig. 4.10b. In fact, the measured curve is dependent on scan direction and is not a perfect exponential. Possible explanations for these problems are suggested in the remaining simulations in Fig. 4.10b, which we now describe in sequence. First, the lower measured V_{oc} compared to the ideal case is explained primarily by introducing defect recombination. As shown in curve 2 of Fig. 4.10b, introducing bulk midgap defects in concentration of $N_t = 10^{16}$ cm^{-3} (for comparison, the Pb atomic density in MALI is about 10^{22} cm^{-3}) is already enough to explain the lower V_{oc} obtained. This can be understood intuitively if one remembers that V_{oc} is the separation between the Fermi-levels inside the perovskite caused by the light when the cell terminals are disconnected, and is given by the balance between carrier recombination and generation.

For a given generation rate (i.e. constant incident light), more recombination means lower carrier concentration, less Fermi-level splitting and lower V_{oc}. Note, however, that this additional recombination channel does not change J_{sc} appreciably. This is simply because at short circuit the cell is very efficient at extracting carriers (the built-in field is at its maximum) so, even with these 10^{16} cm^{-3} additional recombination centers, the cell can still produce about the same current as if the defects were not there. Nevertheless, if N_t is large enough (say 10^{18} cm^{-3} as in curve 3 of Fig. 4.10b), J_{sc} will be affected as well. This appears to not be the case for our cells, since we still observe an exponential-like curve with a reasonable J_{sc}.

Therefore, to explain the lower J_{sc}, we introduce reflection from the surfaces and parasitic absorption (i.e. absorption that does not result in current) in the HTL, as shown in curve 4 of Fig. 4.10b. In this case, J_{sc} was lowered but V_{oc} remained essentially constant. Intuitively, J_{sc} was affected because with less photons absorbed by the perovskite, less carriers are produced and extracted. At first one might think that the lower generation rate should also lower V_{oc} (and indeed it does since for zero incident light, $V_{oc} = 0$ V), but actually the dependence of V_{oc} on incident light intensity is very weak. At V_{oc}, no current is extracted, so even though the generation rate is lower, at steady-state carriers will accumulate inside the perovskite to approximately the same value as if the generation rate was higher (for a given recombination rate). The dependence of V_{oc} on light intensity is logarithmic, since

$$V_{oc} = \frac{nkT}{q} \ln\left(1 + \frac{J_L}{J_0}\right), \tag{4.12}$$

a relation easily obtained from the diode equation (Eq. (2.1)) and the definition of V_{oc}. To a first approximation, changing the generation rate only affects J_L in Eq. (4.12), which is inside the logarithm[2].

Even with these additional effects introduced, the real cell ($\eta = 14$ %) is still less efficient than the simulated ones ($\eta = 16$ % after introducing defect recombination and parasitic absorption/reflection). This time, the difference can be accounted for by the FF, which is ~ 0.75 in the real device but 0.81 in the simulated cell. The lower fill factor in this case is likely due to series and shunt resistances, as shown in curve 5 of Fig. 4.10b. Seris resistance is introduced by the carrier selective layers and means that part of the voltage produced by the cell is dropped on this resistance instead of on the load. The shunt resistance is introduced to account for pin holes in the perovskite layer, which connect the top and bottom electrodes through the ETL and HTL. A shunt resistance means that part of the current produced by the cell will be drained by the shunt instead of going to the load. For not-too-high series and shunt resistances, the V_{oc} and J_{sc} are not significantly affected, so only the FF is changed. As shown in Fig. 4.10b, introducing 3 Ωcm^2 of series resistance (instead of zero) and 1000 Ωcm^2 of shunt resistance (instead of infinity) already lowers performance so that the J-V parameters of the simulated curves approximately match those of the real cell.

The final effect that requires an explanation is hysteresis. Actually, this has already been explained [120–122] as a consequence of mobile ions, which have been ignored in the simulations. If the cell was at open-circuit before the forward scan began, the positive

---

[2] Changing the recombination rate, however, changes the ideality factor, on which V_{oc} depends linearly. This is why recombination affects V_{oc} more strongly than the generation rate.

ions were accumulated at the ETL interface and the negative ions were accumulated at the HTL interface, effectively screening the built-in field at least partially. But after the forward scan the ions were pushed by the applied voltage, changing the screening and the resulting J-V behavior. Unfortunately, SCAPS does not allow to add mobile ions in the simulation, although it is possible to approximate the behavior of the ions by introducing doping densities at the edges of the perovskite layer; see for example Ref. [120]. In any case, simulating the hysteresis would require more precise measurement conditions such as a pre-biasing protocol [121], which we have not adopted. Instead, a maximum power point tracking curve of this cell is presented in Fig. 4.10c, showing that the efficiency obtained with the J-V curve is approximately correct.

We also show the EQE of this cell in Fig. 4.10d. For wavelengths higher than about 800 nm, the efficiency of this cell is zero, as should be expected given that the bandgap of this perovskite is about 1.58 eV, which means that photons of lower energy are not absorbed. For higher energies, the EQE drops because most photons are absorbed close to the PK/NiO interface (the perovskite's absorption depth for $\lambda = 400$ nm is about 50 nm [127]), where a higher trap density is present. Also shown is the EQE measured with a bias light. The drop in efficiency is not very significant, implying that the cell is able to extract carriers efficiently even when it is flooded with carriers. On the right axis of Fig. 4.10d an integration of the EQE weighted by the Sun's spectrum is also shown, giving the accumulated current produced by each wavelength. The total current obtained with the EQE is 20.3 mA/cm^2, in good agreement with the J_{sc} in Fig. 4.10a.

4.2.2 ITO/PTAA/Perovskite/LiF/C$_{60}$/Ag

PTAA is one of the best-performing HTLs for perovskite solar cells [138]. In fact, the first perovskite cells with over 20 % efficiency featured a PTAA HTL layer [62]. However, it is very hard to use it with spin-coating because of wettability problems of the perovskite solution on the PTAA surface. The majority of PK layers that we deposited on PTAA were lost because the PK layer had several holes, as shown in Fig. 4.11.

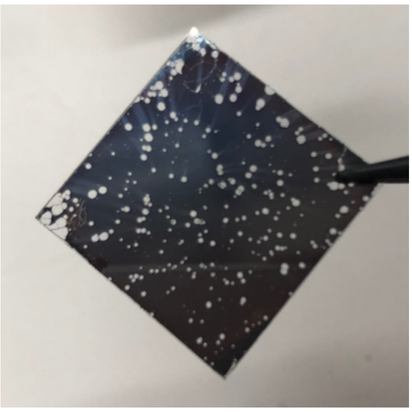

Figure 4.11: Typical perovskite layer deposited on a PTAA-covered ITO substrate, showing many holes caused by wettability problems.

Only a few samples had continuous layers, but, impressively, these were the most efficient cells produced in this work. Fig. 4.12 shows the IV curve of the most efficient cell with the PTAA/PK/C_{60} structure, featuring a V_{oc} of 1.09 V, a J_{sc} of 20.2 mA/cm^2, a FF of 76.7 % and an efficiency of 16.9 %. Note that the main improvement of these cells compared to those using NiO as HTL comes from V_{oc}, which is indicative of a lower recombination rate at the PTAA/PK interface compared to the NiO/PK interface.

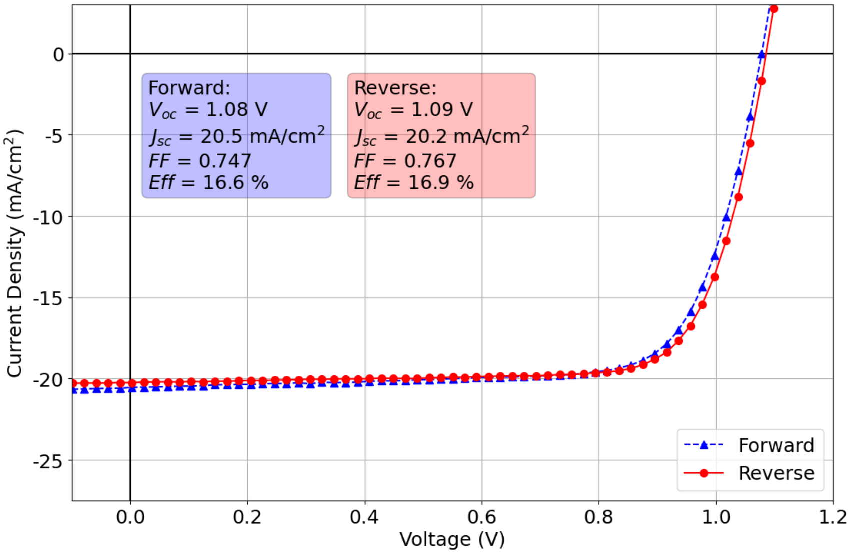

Figure 4.12: IV curve of most efficient solar cell using PTAA as the HTL.

Even though PTAA showed much better performance, we decided not to pursue it as an HTL. First, reproducibility was very pour, meaning our deposition setup still had uncontrolled variables that were preventing rigorous scientific tests. Second, and more importantly, there is no known way to deposit PTAA on the textured surfaces of Si/perovskite tandems[3]. Nevertheless, the fact that we managed to make such efficient cells with PTAA shows that there is much room for improvement with regards to lowering recombination at the HTL/PK interface (and probably also the PK/ETL interface).

4.2.3 ITO/NiO/Perovskite/LiF/C_{60}/SnO_2/ITO/Ag

We now discuss a different cell structure where the top metallic contact is substituted by a SnO_2/ITO/Ag stack. The Ag in this case does not cover the entire cell area, only the perimeter, as shown in Fig. 4.13. This cell structure is partially transparent, thus the name "semitransparent". The ITO is necessary to improve lateral conductivity at the top of the cell, and the SnO_2 is necessary to avoid sputtering damage on the C_{60} by the ITO deposition. This is the cell structure that would be replicated in a Si/perovskite tandem (with light shining from the Ag side).

In Fig. 4.13b, representative I-V curves (measured in a reverse scan) for semitransparent and opaque structures are compared. First, it is clear that the J_{sc} is lower for semitransparent, in this case by about 1 mA/cm^2. This can be easily understood by

---

[3] Spin-coating results in very non-uniform layers and regular vapour deposition techniques do not work with polymers.

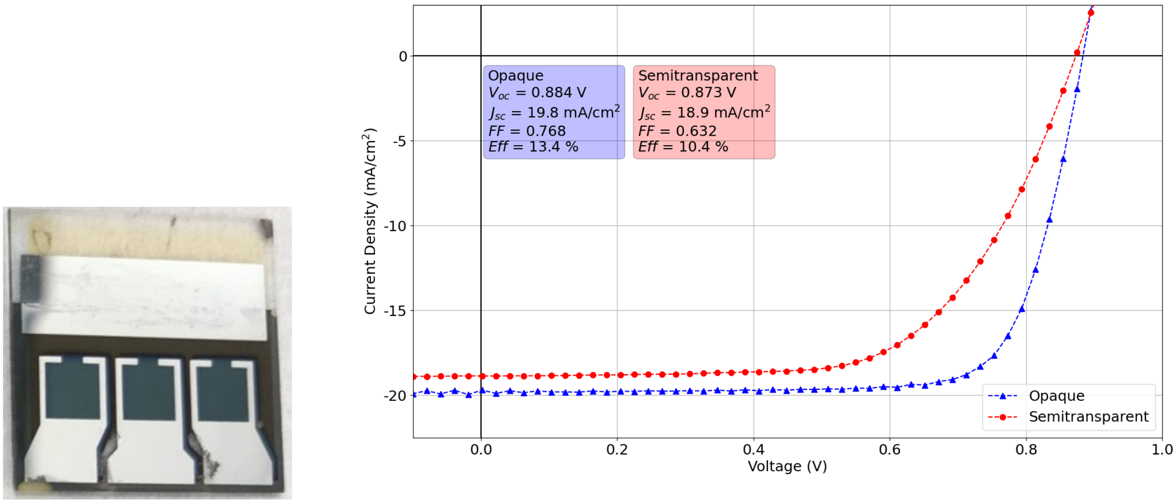

(a) (b)

Figure 4.13: a) Picture of semitransparent solar cell. b) Comparison between I-V curves of opaque and semitransparent cell structures.

the fact that this cell is semitransparent, meaning it absorbs less light, which is a consequence of the lack of a top metallic layer reflecting back the portion of the light that is transmitted through the PK/C_{60}/SnO_2/ITO stack. However, it should be noted that this current loss would be less severe in a tandem structure, because in that case the bottom cell would absorb the light transmitted through the top cell.

More critical is the observed increase in series resistance for the semitransparent structure compared to the opaque, here observed as a drop in FF (from 76.8 % for opaque to 63.2 % for semitransparent in the case of Fig. 4.13b). There are two sources of series resistance that could be at play in this case. First, since the metallic contact is only at the perimeter of the cell, the current produced far from the contact must pass laterally through the ITO. The sheet resistance of the ITO layer is about 100 Ω/sq (as measured by the four-point probe technique on a glass sample inserted on the ITO deposition together with the actual samples), so, even with the addition of the conductive ITO layer, the lateral resistance at the top of the cell is not negligible. The second source of series resistance is the longitudinal resistance associated to the new layers present in the semitransparent structure. In this case, the resistance does not come from the bulk of the layers themselves, since they are very thin. Rather, this series resistance is caused by the various contact resistances associated to the interfaces C_{60}/SnO_2 and SnO_2/ITO.

4.2.4 Different Metals as Contacts

The cells studied in this section had the same structure of those analyzed before: ITO/NiO/Perovskite/LiF/C_{60}/metal for opaque or ITO/NiO/Perovskite/LiF/C_{60}/SnO_2/ITO/metal for semitransparent; the only difference is that the top electrode composition was either Al, Ni, Cr, Cu or Ag (all deposited by evaporation). I-V curves of representative opaque solar cells are shown in Fig. 4.14a and pictures of cells using the different metals are shown in Fig. 4.14b. In the case of Ni, we observed delamination problems on most of the cells, which indicates very poor adhesion of the metal on the C_{60} layer underneath. Therefore, even for the cells where the Ni contact was intact, we expect some contact resistance that might severely limit cell performance, as indeed seems to be the case in the I-V curve shown in Fig. 4.14a for Ni. In the case of Al, we observed a reaction of the Al with one or more of the cell's remaining layers where yellow spots appeared on most of the cell area, as shown in Fig. 4.14b. This reaction probably created an insulating layer beneath the metallic contact that completely hindered current flow, which would explain the very high series resistance in Fig. 4.14a for the Al curve.

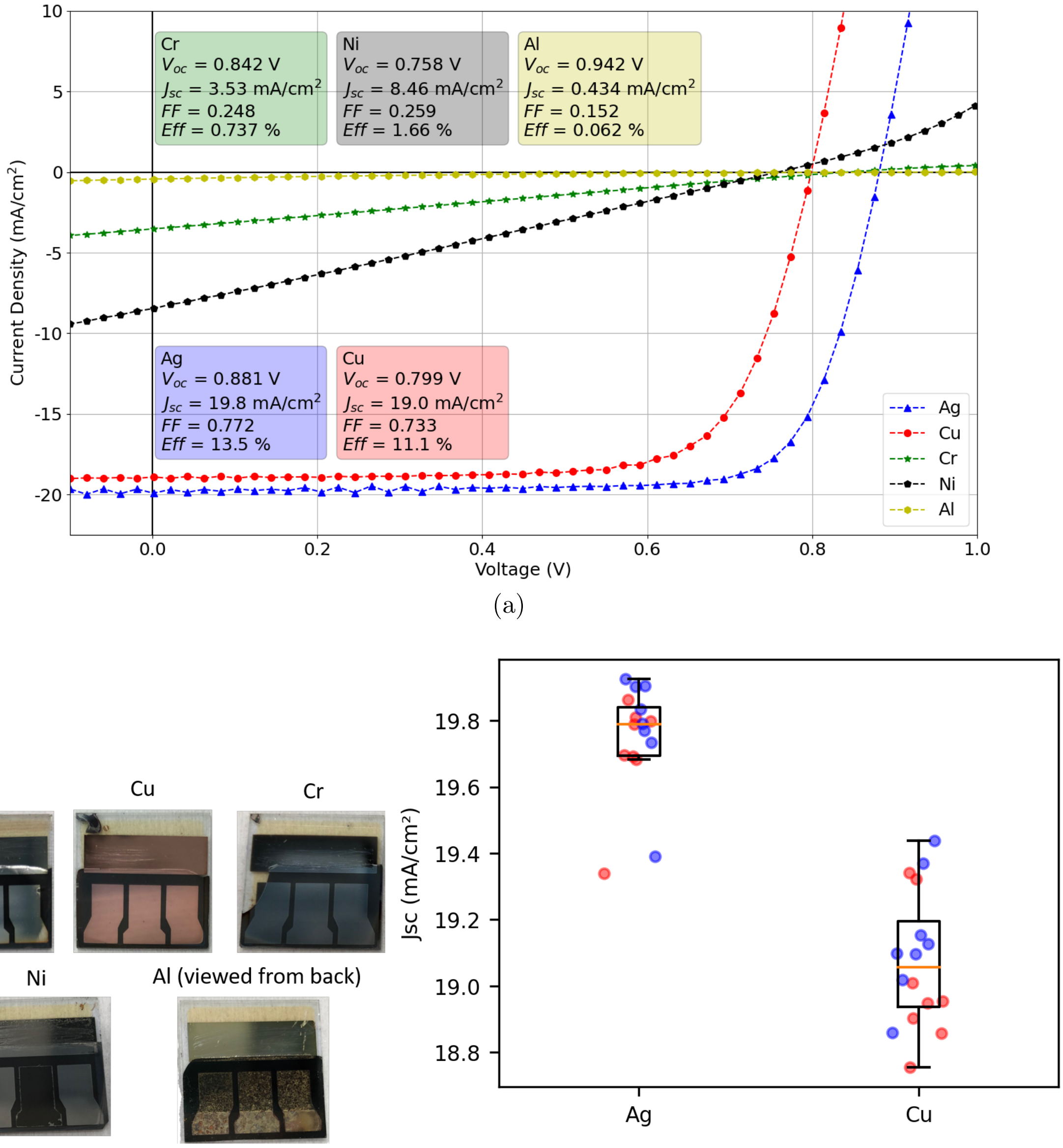

(a)

(b)

(c)

Figure 4.14: a) I-V curves of opaque solar cells using different metals as electrodes. b) Pictures of typical samples using the different top metals. c) Scatter plot of the J_{sc} of all cells using Cu and Ag.

In the Cr and Cu cases, however, no visible problems were observed on immediate inspection of the samples. Nevertheless, clearly the IV curve was affected. For Cr, the rise in series resistance with respect to the Ag reference cells can be easily explained by the much higher resistivity of Cr with respect to Ag (13 $\mu\Omega$cm compared to 1.6 $\mu\Omega$cm, a ten-fold increase). In the Cu case, however, the resistivity is very similar to that of Ag. In fact, the I-V curves for Cu and Ag do not even indicate different series resistances, since the slopes of the I-V curves near V_{oc} for the two cases are nearly the same. Furthermore, the two I-V curves are approximately parallel, which indicates a more intricate effect where the metal is affecting the built-in voltage inside the perovskite. (Also, it is not just these two particular samples shown in Fig. 4.14a that presented this effect, as shown in the statistics in Fig. 4.14c.) At first one might suspect that Cu, having a slightly higher workfunction than Ag, could have a sligthly higher barrier for electron extraction from the C_{60} and result in a lower built-in voltage inside the perovskite, causing the effect observed. This explanation does not work, however, as shown in the simulations of Fig. 4.15a for different top metal workfunctions. First, a higher metal workfunction would cause an S-shaped I-V curve, which is not what is observed. Second, the workfunction would have to be unreasonably high to even affect the I-V curve. Third, the change in workfunction alone cannot cause the lower J_{sc} observed for the Cu cells, since a small change in the built-in voltage does not change the J_{sc}. Therefore, we concluded that another effect must have happened.

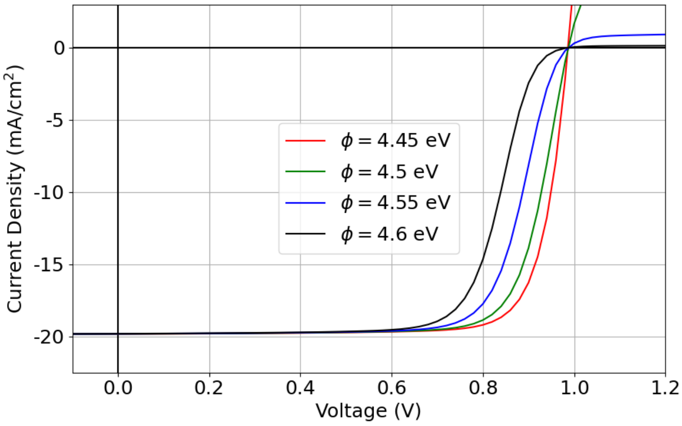

Figure 4.15: Simulations of I-V curves for different top-metal workfunctions, denoted as ϕ.

There are at least two ways for the top contact to affect the cell's J_{sc}. Both mechanisms postulate that the Cu introduces electrically and/or optically active defects at the C_{60} layer or at the interface. If the defects are optically active, the Cu would alter the optical absorption profile of the cell by altering the absorption profile of the C_{60}. Since a portion of the incident light is transmitted through the PK and C_{60} layers and reflected back by the top contact, re-entering the absorber, the transmitance of the C_{60} layer does affect the electron-hole pair generation profile inside the cell. Therefore, if the Cu generates optically active defects in the C_{60} or at the interface, it could lower the cell's J_{sc}. The other way for the top contact to affect the J_{sc} is if the defects are electronically active, meaning they introduce recombination between electrons and holes. These defects would lower both J_{sc} and V_{oc}, which is what is observed.

The hypothesis that the different metals can react with the other layers in the cell would suggest that in semi-transparent cells the effects caused by electrode composition should be less important, since in this case the SnO_2/ITO layers in between the metallic contact and the rest of the cell should act as a barrier for reactions. Indeed this seems to be the case, as shown in Fig. 4.16. Here, all metals resulted in working cells, although series resistance was again influenced by the electrode composition (to a lesser extent compared to opaque cells). In this case, it seems plausible that the different resistances of the contacts (either the metal layer resistance itself or the metal-ITO contact resistance) alone could explain the differences in performance.

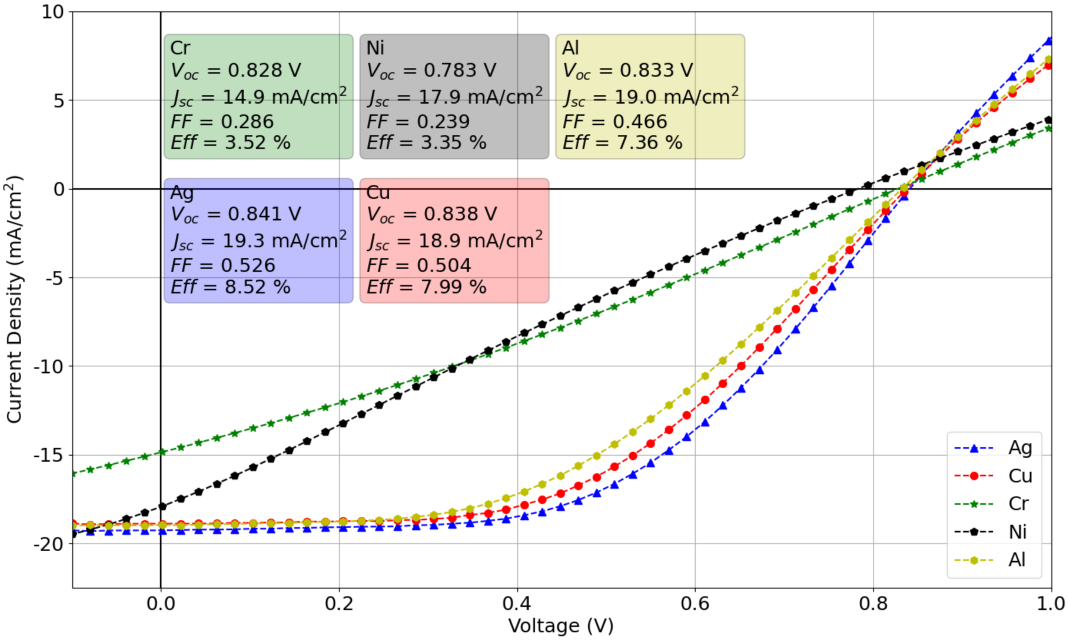

Figure 4.16: IV scans for semitransparent cells using different metals as electrodes.

4.3 Reverse Bias Instability of Perovskite Solar Cells

Our study on reverse bias stability used the perovskite $(FAPbI_3)_{0.83}(CsPbBr_3)_{0.17}$ and the cell structure shown in Fig. 4.17a, which is a semitransparent cell. The advantage of studying semitransparent cells over opaque cells is that it allows for a simultaneous assessment of the stability of regions covered and not-covered by metal electrodes. Also, it mimics the structure in some of the most efficient Si/perovskite and perovskite/perovskite tandem cells [107]. Nevertheless, it is likely that different different cell structures and layer compositions will give different results with respect to reverse bias stability.

To monitor the reverse bias induced degradation, we adopted a stress-test whereby the reverse voltage is progressively increased in increments of -0.1 V for 3 minutes per step. After each step, current-voltage curves are taken first with a forward (-0.1 V to 1.2 V) and then a reverse (1.2 V to -0.1 V) scan to monitor changes in performance. A representative evolution of the I-V curve (forward scans) of a cell using the above protocol is shown in Fig. 4.17b. Two degradation mechanisms are found to occur in

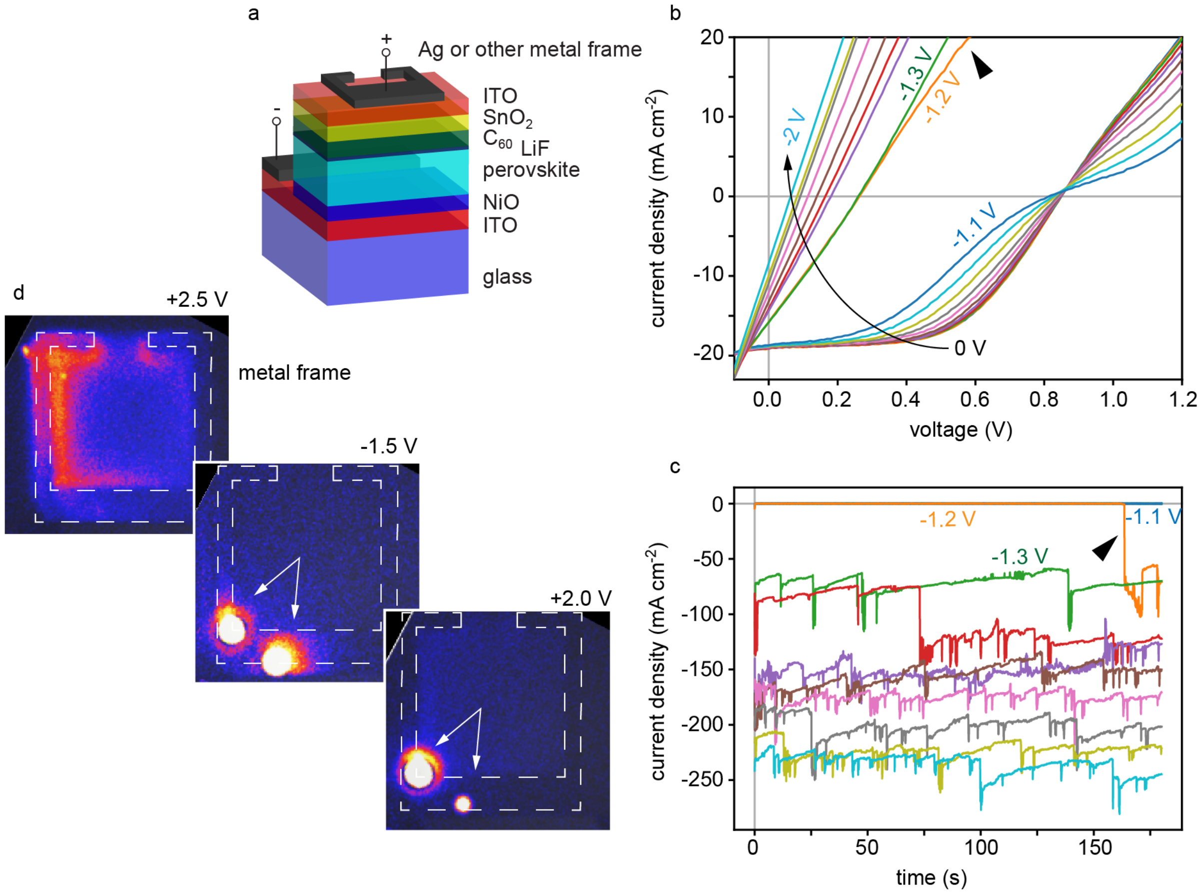

Figure 4.17: (a) Structure of the cell studied in this work. The "+" and "-" signs indicate that the cell is reverse biased. (b) I–V curves taken immediately after biasing the cell at progressively higher (in absolute value) reverse voltages. (c) Reverse current measured during the 3 min of each reverse biasing step. (d) Left: Thermograph of a fresh cell measured with a forward bias of 2.5 V, middle: same cell imaged at a reverse bias of -1.5 V, showing two new hot spots, and right: same cell under a forward bias of 2 V (after it had been reverse biased at -1.5 V), demonstrating that the shunts that formed in the reverse bias step are still present.

succession. For voltages less (in magnitude) than -1.2 V, an S-shape appears, while for higher voltages the cell becomes shunted, as observed from the decrease in V_{oc} and linear I-V characteristics. Fig. 4.17c reports the reverse current that flows through the cell at each reverse bias step. It is seen that, for this sample, the reverse current remains negligible (less than 1 mAcm^{-2}) for reverse voltages up to -1.1 V. However, after nearly 3 minutes at -1.2 V the current increases abruptly to more than 50 mAcm^{-2} in magnitude, signaling the formation of one or more shunts. In addition, burst noise, typical of metal precipitates inside semiconductor devices [156], appears at this point in the current signal.

To verify that shunts are indeed forming under reverse bias, fresh devices were analyzed by dark lock-in thermography. These devices were first driven with a forward bias of 2.5 V, with the resulting thermograph exhibiting no hot spots (top left panel of Fig. 4.17d). This initial test confirms that no significant shunts were present in the fresh state.

Subsequently, exposing the cell to a reverse voltage of -1.5 V (with 1:1 on-off duty-cycle at 25 Hz) was found to induce the formation of hot spots at the position of the Ag frame (middle panel in Fig. 4.17d). When driving the cell again in forward bias (bottom right thermograph in Fig. 4.17d), the two hot spots remained, indicating that these shunts were formed during the reverse bias treatment and that the cell remained shunted when the reverse bias was removed.

For cells stressed up to voltages of -5 V instead of -2 V, shunts at the position of the metal electrode became severe enough for burn marks to be visible by the naked eye, as shown in Fig. 4.18a. In fact, the metallic shunts could be seen from the glass side in the regions of the burn marks. Furthermore, once the shunts are formed, the high power dissipated in these regions quickly degrades the absorber (which becomes porous with Pb-rich inclusions) and the Ag electrode (which clusters in some regions) as highlighted by the scanning electron microscopy images shown in Fig. 4.18b. Notably, cells featuring Cu or a Ni/Al stack as top electrode in place of Ag showed similar shunting behaviour (Fig. 4.19a). Regular opaque cells, with a metal electrode deposited directly on top of the electron transport layer (C_{60} here) were also tested. Their stability in reverse bias was found to be even worse with electrode shunts forming at reverse voltages as low as -0.3 V (Figure 4.19b).

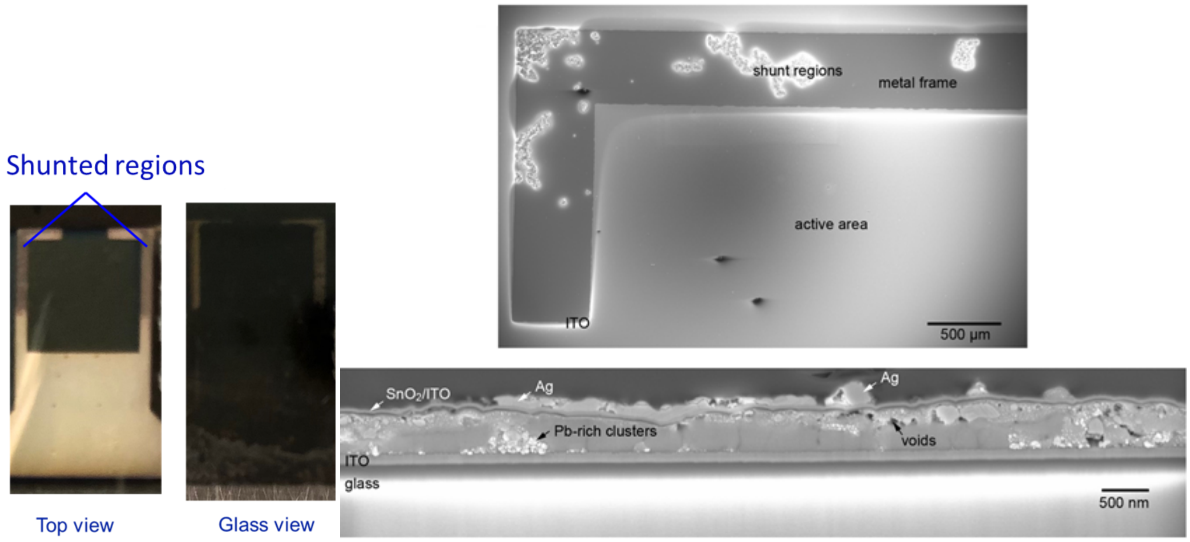

(a)

(b)

Figure 4.18: a) semitransparent solar cell reverse biased from 0 V to -5 V in 3 min steps of -0.1 V showing visible burn marks. The top Ag contact can be seen from the glass side. b-c) Top view and focused ion beam-prepared cross-section scanning electron microscopy images of shunted areas.

Bias-induced migration of Ag and other electrode materials (including Au) has been observed directly in several prior studies. [70,157] Under reverse bias, the applied potential is of the correct polarity to drive positively charged Ag ions through the perovskite layer to the opposing electrode. The most obvious explanation for our observations concerning reverse-bias shunting in cells with metal coverage is therefore that metallic filaments are formed under reverse bias in a manner analogous to that proposed for

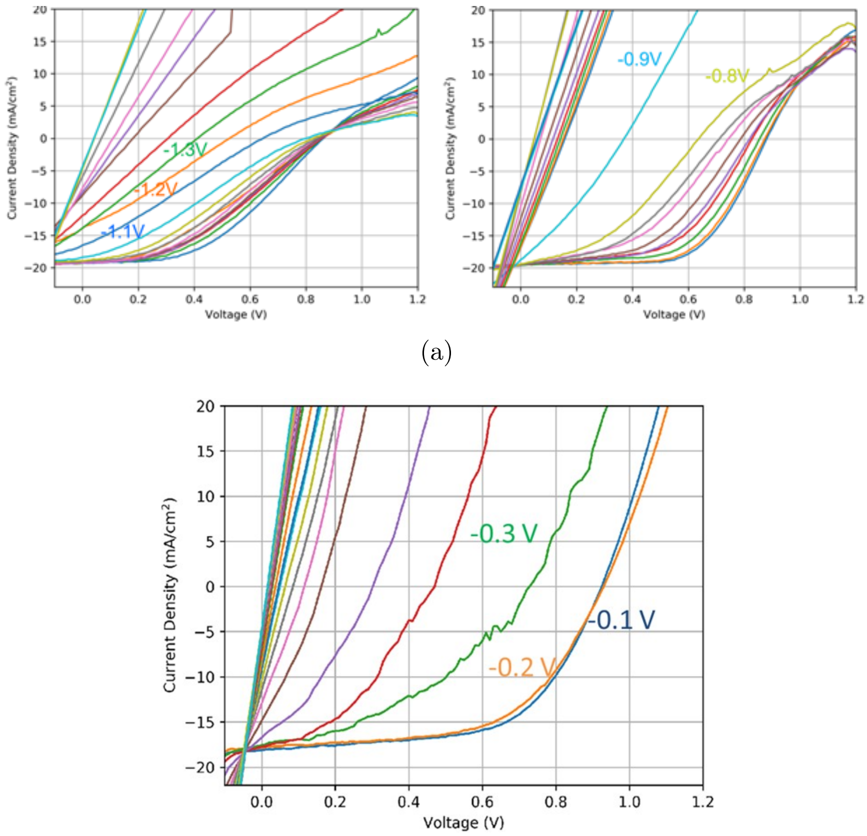

(a)

(b)

Figure 4.19: a) Evolution of the I-V curve after reverse biasing at increasing voltages devices comprising Cu (left) and a Ni/Al stack (right) as back electrode. b) I-V curve evolution of an opaque solar cell, where the Ag back contact covers the entire area of the device.

memristive devices, [158] although in this scenario migration must occur not only through the perovskite layer but also through the conformal ITO and SnO_2. SEM cross-sections of a degraded device indeed clearly show the presence of metallic domains within the perovskite layer beneath regions with missing electrode material (Fig. 4.18b), giving strong support to this hypothesis. On the other hand, even cells without a metal electrode (with only ITO on top) were found to develop shunts under reverse bias, but this time only at significantly lower voltages of about -3 V (Fig. 4.20). This indicates that the perovskite layer itself has limited stability under reverse bias, likely becoming rich in metallic lead in those regions that are observed to shunt. Therefore, we propose that there are two shunting mechanisms caused by reverse bias: electromigration of the top electrode through the perovskite and perovskite layer degradation into metallic Pb. The former mechanism is induced at lower (in magnitude) reverse voltages compared to the latter.

It is worth noting that the mere appearance of hot spots in reverse bias does not necessarily imply that it is the reverse bias itself that creates shunts. It is possible a priori for shunts to form during cell manufacturing and not be significantly affected by reverse bias, except at extreme voltages when growth due to heating occurs. In this case

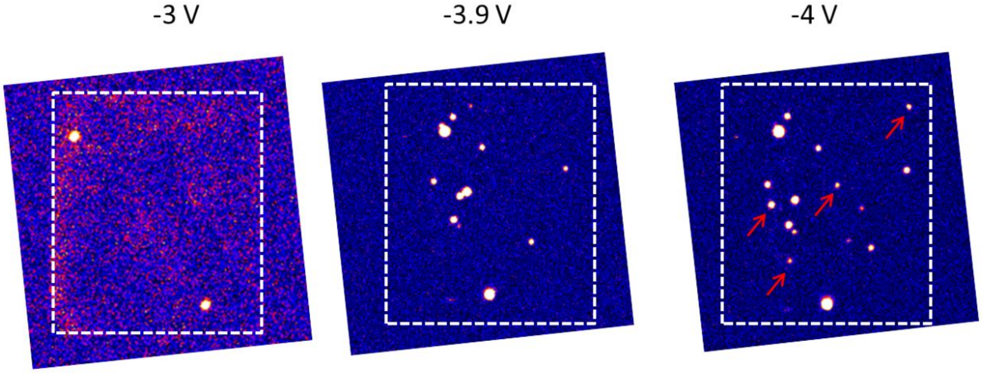

Figure 4.20: Hot spot formation observed with lock-in thermography in cells comprising no metallic top electrode (only ITO on top). The dashed white square delineates the region of the cell covered by the ITO electrode. At −3 V (left panel), two hot spots are observed, showing that even metal-electrode-free solar cells shunt under reverse bias, although only at heavier reverse biasing compared to cells with metal. In the middle and right panels, a comparison between images taken at −3.9 V and −4 V is shown. Arrows indicate hot spots that appeared abruptly during the biasing step to −4 V. The fact that these hot spots were invisible during the previous biasing step is an indication that they were created by the reverse bias itself, as opposed to simply enlarging due to heat as in c-Si solar cells. These results indicate that the absorber layer itself also shunts under reverse bias, even in the absence of a metal electrode.

a forward bias would also induce heating in the location of the shunts just as much as a reverse bias, as long as the voltages are equal in magnitude and the shunts are ohmic. This is the usual assumption when interpreting lock-in thermography images of c-Si solar cells in reverse bias, although it is possible that even some c-Si solar cell architectures can present reverse bias-activated shunting. In the case of perovskite cells, it is also possible that the fabrication process may leave some shunts, but Fig. 4.17d clearly shows that other mechanisms are occurring. Initially, at a forward bias of +2.5 V, we observe no hot spots, while at −1.5 V, some appear. These shunts then remain visible in forward bias.

Prior to electrode shunting, an S-shape in the I-V curve is observed to form with increasing severity as the reverse pre-biasing increases (Fig. 4.17b). The relation to voltage pre-biasing and similarity to I-V curves reported in several modelling studies of hysteresis [120–122] suggests that the effect is likely related to ion migration. However, one notable difference here is that the V_{oc} remains remarkably constant with increasing exposure to negative voltages, by contrast with most observations in the context of hysteresis. This is suggestive of a process that affects charge transport but has a minimal effect on recombination. To assess the mechanism associated with the S-shape formation, reverse-biased solar cells were investigated using scanning transmission electron microscopy (STEM) coupled to energy dispersive X-ray (EDX) spectroscopy. Fig. 4.21a shows a STEM high angle annular dark-field (HAADF) image of the cross-section of a cell, in a region far from the metal electrode, that was reverse biased up to −5 V using the protocol described above. Apart from the formation of large voids indicative of a loss of material during either the biasing experiments or during the TEM sample preparation by focused ion beam (FIB), the biased cell exhibits a double layer microstructure, with a relatively smooth top layer (adjacent to the n-type electrode) and a rough bottom layer. For comparison, a STEM image of an as-deposited reference cell is shown in Fig. 4.21d. The reference cell also exhibits some voids, although of a smaller size and likely induced by the FIB preparation, but no double layer structure, confirming that the latter feature is caused by the reverse bias treatment. The EDX chemical map and atomic concentration profile shown in Fig. 4.21b of the reverse biased cell also show that the top and bottom layers have different Br concentration. This is evidence of bias-induced phase segregation and will be discussed later on, but does not provide an immediate explanation for the formation of the S-shape.

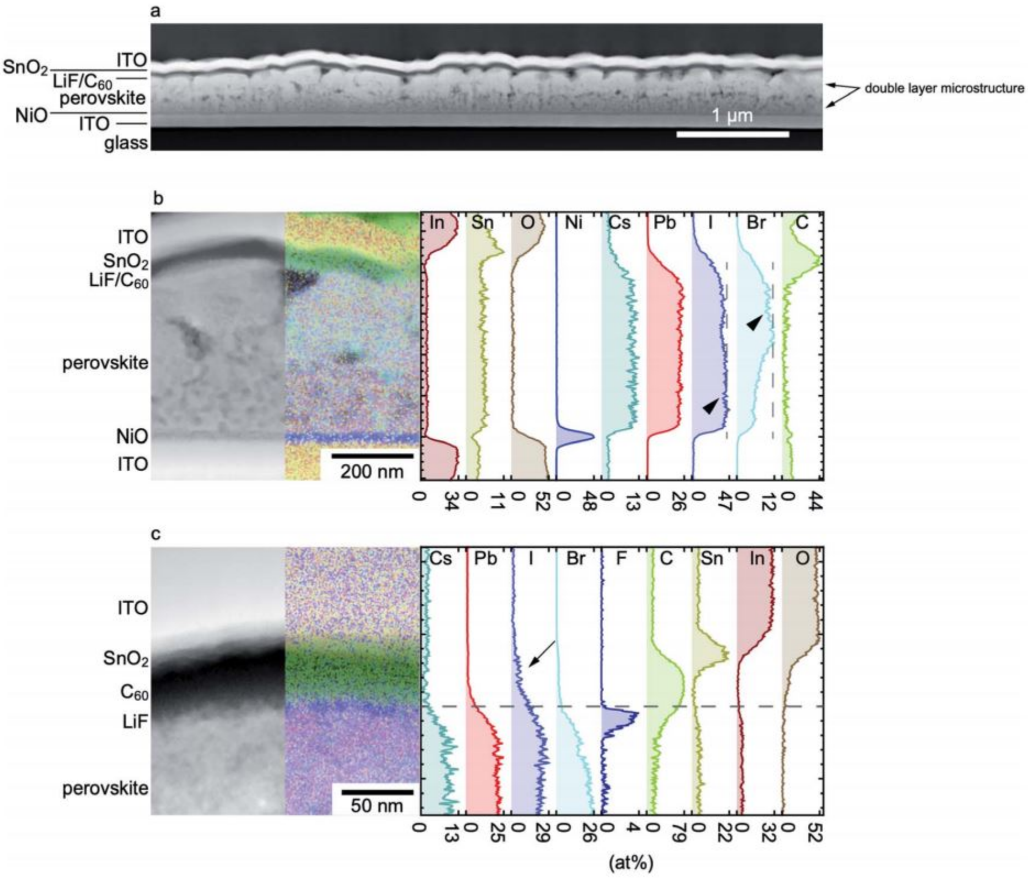

Figure 4.21: (a) Scanning transmission electron microscopy (STEM) high-angle annular dark-field (HAADF) image of a solar cell degraded at −5 V. (b) STEM HAADF image of the cell shown in (a) superimposed on its right side with its corresponding EDX chemical map and corresponding concentration profile. The Sn signal inside the PK layer is an artifact of the quantification procedure. (c) STEM HAADF image and corresponding EDX chemical map and concentration profile of a sample with a higher Br content taken in the region close to the perovskite/LiF/C_{60} interface, which highlights the migration of iodide into the C_{60} layer during reverse biasing (arrowed).

The magnified view of the perovskite/LiF/C_{60} interface shown in Fig. 4.21c provides a more suggestive explanation of the I–V characteristics seen in Fig. 4.17. Iodine is seen to have migrated beyond the LiF and into the C_{60} layer following reverse bias by comparison with the unbiased reference (Fig. 4.22). On the other hand, the Cs, Pb and Br EDX signals do not extend as far across the same interface (note that some overlap between the different layers is induced by projection effects, as the perovskite layer exhibits some roughness and the sample is about 100 nm thick). The reference sample, on the other hand, had better separated distributions for the perovskite and C_{60} layers as shown in Figure 4.21d. Voltage-driven halide migration into an organic selective contact (Spiro-OMeTAD) was also observed in a previous study employing in situ TEM [65]. One possible explanation for the S-shape behaviour is therefore that iodide acts as p-type dopant in C_{60}, as reported for I_2 in several organic semiconductors such as pentacene, [159] or that it simply charge compensates the n-type doping resulting in a reduced carrier density. In the latter case, carrier densities may be reduced to the point where transport is no longer ohmic and instead occurs in the (non-linear) space charge-limited current regime. [151]

The formation of S-shaped I-V curves following reverse bias appears to be reversible to some extent. To investigate this, solar cells without metal on their front electrodes were fabricated in order to avoid the issue of electrode shunting. These cells were then reverse biased according to the stress-testing procedure described above. As shown in Fig. 4.23a, the absence of metal indeed prevents the formation of ohmic shunts when the cell is stressed up to -2 V. Without their masking effect on the I-V curve, it is seen that the S-shape gets progressively more severe as the reverse voltage is increased. After reverse biasing, the metal electrode-free cell was submitted to maximum power point tracking (MPPT) for about 1 h and, as shown in Fig. 4.23b, the efficiency recovered to its initial value of about 7.3 % (a low value caused by a high series resistance due to the absence of a metal electrode). In Fig. 4.23c a comparison between the I-V curves before and after degradation, and after recovery, is shown. The initial and recovered I-V curves almost overlap in the power-generating quadrant, with only a small decrease in the current injection beyond V_{oc}. Notably, cells were found to recover even when left in the dark, although at a slower rate than with MPPT.

To further support the suggestion that it is the iodine inside the C_{60} layer that is causing the S-shapes in Fig. 4.17b and 4.23a, we also made EDX maps of a degraded and recovered metal electrode-free solar cell. As shown in Fig. 4.24, no iodine signal was found inside the C_{60} layer for a recovered solar cell, strengthening our hypothesis.

The phase segregation of mixed halide perovskites into I-rich (low bandgap) and Br-rich (high bandgap) regions was first reported by Hoke et al. [75] Since then, significant progress has been made in identifying the causes and implications of this phenomenon. [59,76–80] Although some factors remain unclear, [79,81] it has been shown that this effect is intimately linked to the presence of excess free carriers in the perovskite, whether by photogeneration or electrical injection. [80]

Here, direct evidence of reverse bias-induced phase segregation was obtained using electron microscopy (Fig. 4.21b). The sample investigated by STEM EDX experienced a reverse bias of -5 V, a voltage significantly below the breakdown voltage, denoted hereafter as $-V_{bd}$, ($V_{bd} \approx$ 1–1.5 V, Fig. 4.25). Consequently, a high current passed through the cell (about 1 Acm^{-2}), likely inducing this phase segregation. The steady state photoluminescence (PL) spectra shown in Fig. 4.26a are further indications of the phase segregation induced by this current injection. For this experiment, a fresh device

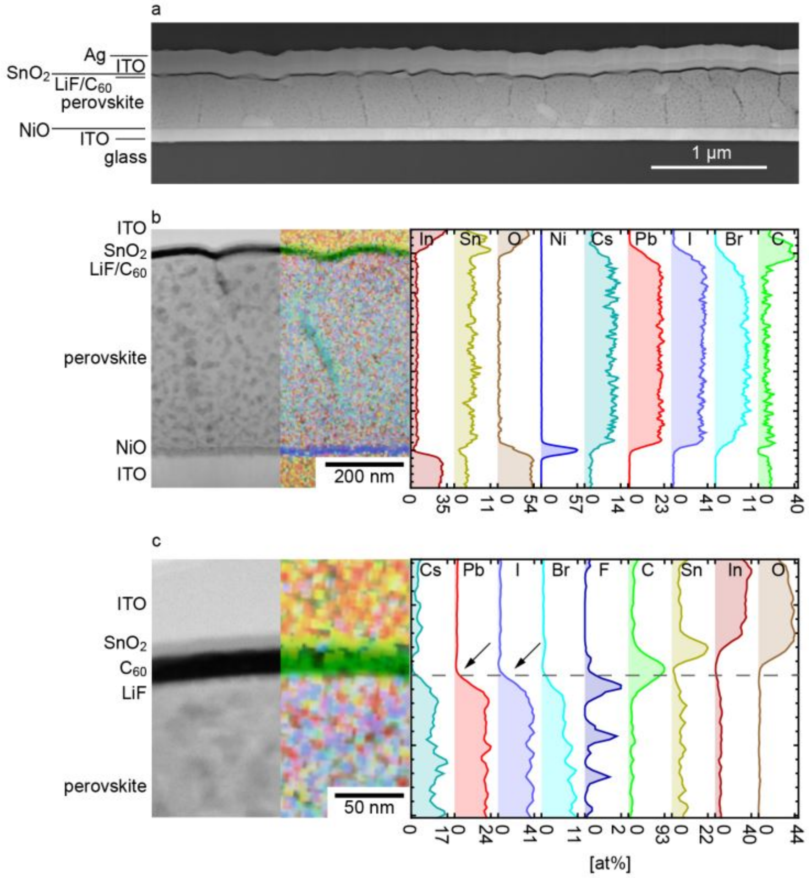

Figure 4.22: a) STEM HAADF image of a reference as-prepared device. The small voids are a consequence of the focused ion beam preparation of the TEM lamella. No double-layer structure is observed, contrary to Fig. 4.21, which was of a sample reverse biased at −5 V). (b) EDX chemical map and corresponding concentration profile of the reference sample, showing no gradient in Br (unlike Fig. 4.21). (c) STEM HAADF and EDX data of the region close to the C_{60} layer. Note that the top edges of the Pb, I and Br distributions coincide in position and are well separated from the carbon peak of the C_{60} layer.

was reverse biased at −3 V for 15 min and then the PL signal was measured from both sides of the sample (excitation wavelength of 514 nm corresponding to an absorption depth of about 120 nm). A redshift of about 0.02 eV in bandgap is observed according to the luminescence measured from the NiO side, as would be expected given the I-rich region observed in the STEM EDX data (Fig. 4.21b). By contrast, a slight blue-shift (approximately 0.005 eV) was measured from the C_{60} side, also in accordance with the EDX data. The PL laser on its own was also able to induce shifts in the bandgap, but only if a high enough photon dosage was provided with either high intensity or long exposure times. To investigate the bias-induced segregation alone, the exposure time (10 s) and intensity (1 sun) of the PL laser were chosen so that no shift was observable whilst acquiring the spectra.

Phase segregation induced by reverse biasing has not been reported in any prior study

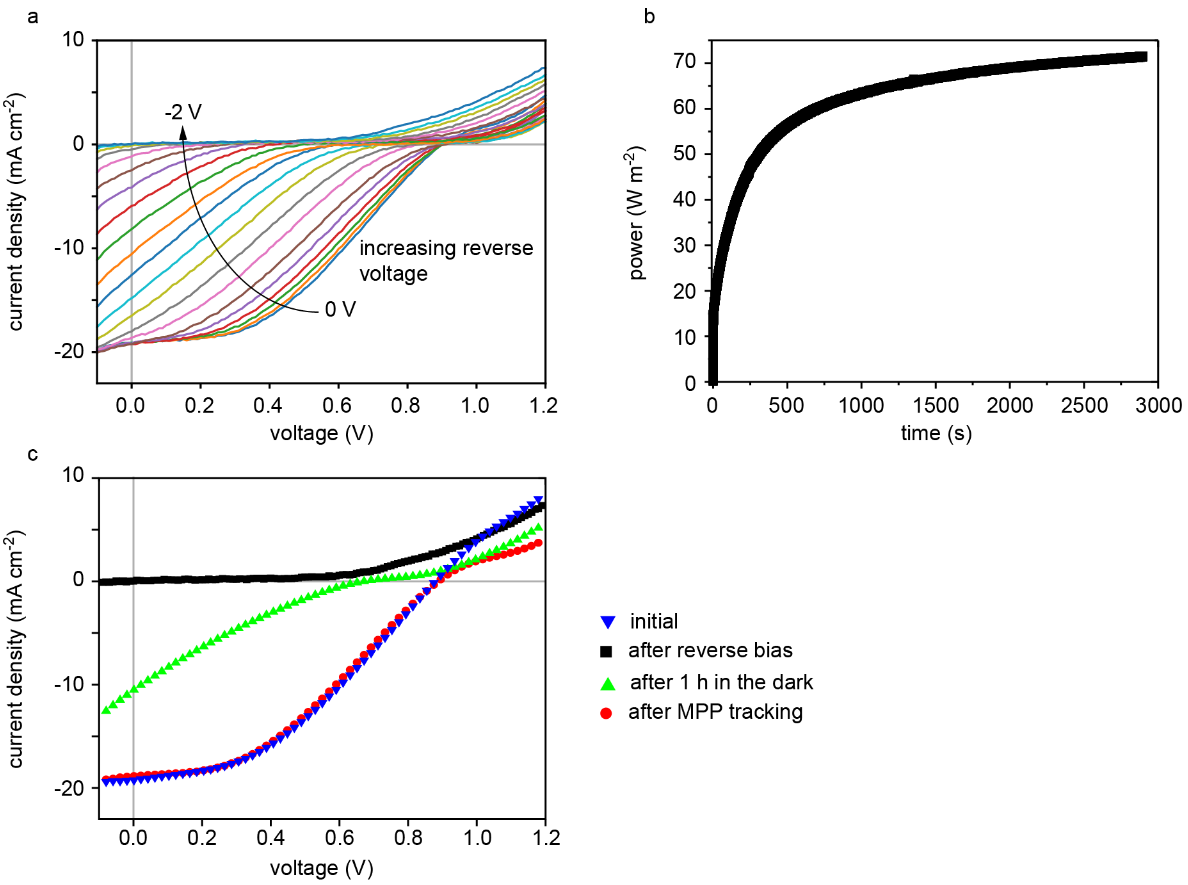

Figure 4.23: (a) I–V curves of a cell without any metal electrode taken after progressively increasing the absolute value of the reverse bias. While a severe S-shape builds up, no shunts appear. (b) Maximum power point tracking of the same cell after degradation, showing that the efficiency recovers. (c) Comparison of the I–V curves of the same cell in its fresh state, immediately after reverse biasing, after 1 h in the dark and after maximum power point tracking.

to our knowledge, although its occurrence would be expected given the link to carrier-injection in the perovskite. Duong et al. [76] observed phase segregation under forward biasing but reported negligible segregation when applying a reverse voltage of -1 V for 12 h. While the V_{bd} of the cell in that study was not reported, it can be assumed that 1 V was not sufficient to reach breakdown and negligible current was injected in the absorber. A similar situation was recreated in Fig. 4.26b, which provides the PL data of a sample biased at -0.5 V for 15 min, a voltage below the $-V_{bd}$ of approximately -0.8 V of this cell (Fig. 4.25). No bandgap shift was observed, in agreement with the hypothesis that a significant excess carrier density is required to trigger phase segregation.

Shifts in luminescence observed with PL are expected to depend not only on the extent of the phase segregation (and therefore on the value of the reverse bias applied to the cell) but also on the diffusion length of the carriers in the device. With short diffusion lengths, the wavelength of emission will be strongly influenced by the location of carrier generation, and hence result in blue-shifted emission when illuminating from

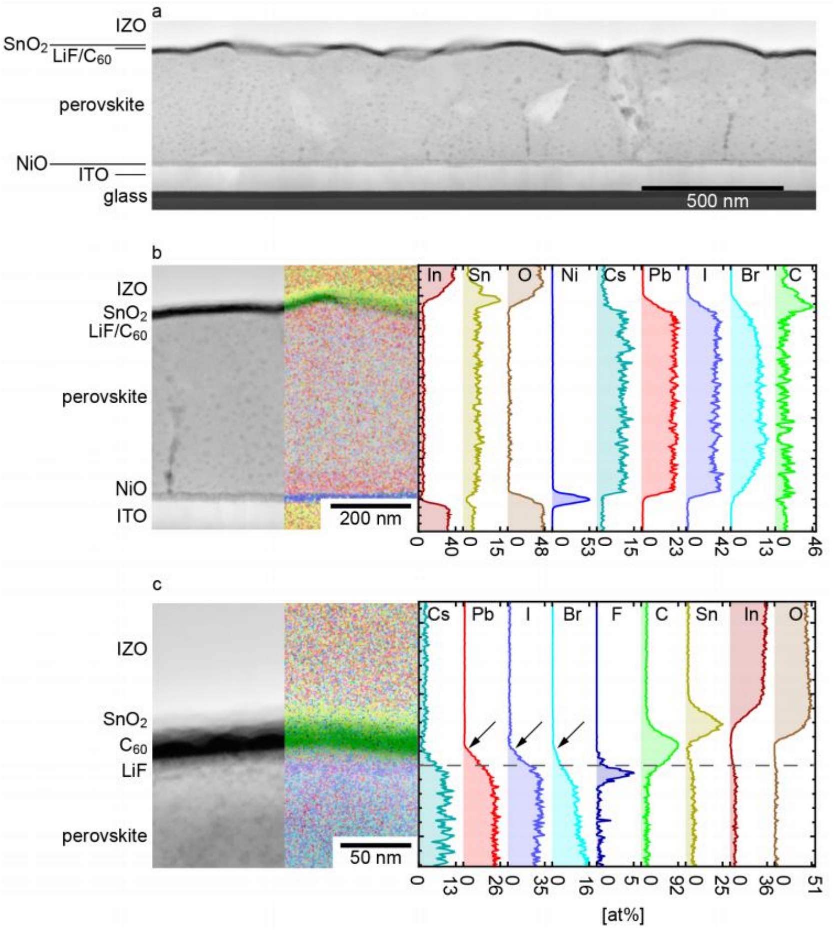

Figure 4.24: a) STEM HAADF image of an electrode metal-free device after recovering from an S-shape at MPPT. The small voids are a consequence of the focused ion beam preparation of the TEM lamella. (b) EDX chemical map and corresponding concentration profile of the recovered sample. (c) STEM HAADF and EDX data of the region close to the C_{60} layer. Note that the top edges of the Pb, I and Br distributions coincide in position and are well separated from the carbon peak of the C_{60} layer, corroborating our conclusion that it is the iodine inside the C_{60} layer that causes the S-shape.

the high-bandgap side and red-shifted emission from the low bandgap side. On the other hand, with long diffusion lengths, all carriers will migrate to the lower bandgap region and emit a low energy photon, irrespective of illumination direction. Indeed, in some cases we observed a red-shift in the perovskite bandgap in the PL spectra obtained from both sides of the device. In Fig. 4.27, for example, the PL spectra of a sample degraded at −5 V for 30 min is shown, with an observable redshift when measuring from both NiO and C_{60} sides. The difference between Fig. 4.26a and 4.25 is indicative of a difference in carrier lifetimes and size of the segregated regions. Presumably, the sample degraded at −5 V for 30 min had a thicker I-rich layer, which would translate into carriers being able to reach the lower bandgap region even when the light is shone from the C_{60} side.

It is natural to consider that the S-shape discussed previously might be a side-effect of the phase segregation, given that both phenomena are caused by reverse bias. We ruled this out by measuring the PL of samples that presented an S-shaped I–V curve.

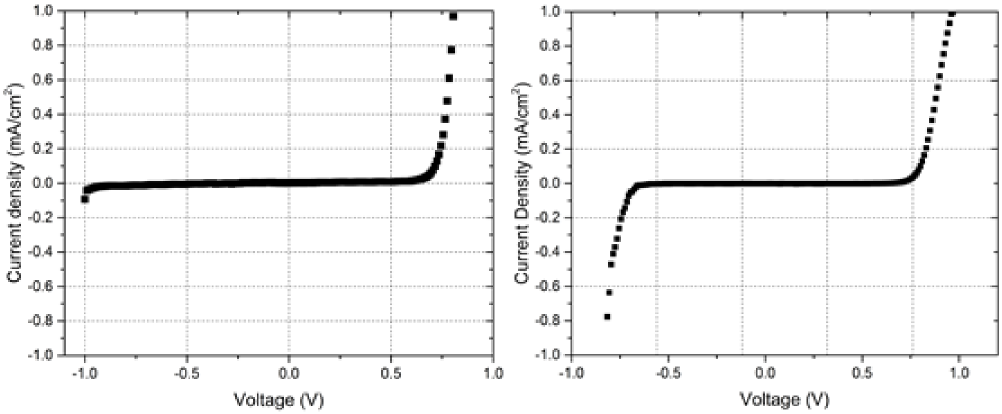

Figure 4.25: Dark I-V curves for the cells degraded at −5 V (left figure) and at −0.5 V (right figure). For the cell degraded at −5 V (left figure), the reverse bias was larger than the breakdown voltage and phase segregation was observed. For the cell degraded at −0.5 V (right figure), the reverse bias was lower than the breakdown voltage and no phase segregation was observed.

In Fig. 4.28, we show the PL of the sample for which the I–V curves after reverse bias treatments are shown in Fig. 4.23a. No observable shift in the peak position was found. Furthermore, no significant current flowed through the sample during these treatments, as shown in Fig. 4.28. Therefore, it seems that this sample did not phase segregate, even though it had an S-shaped I–V curve after reverse biasing. These observations indicate separate mechanisms for the two effects and reinforce our hypothesis that the S-shapes result rather from migration of iodide into the C_{60} layer.

While an injection of charges is required to trigger phase segregation in reverse bias, in accordance with mechanisms proposed to be the cause of light-induced phase segregation, [77,80] there are several differences between our observations and the light-induced phase segregation process first reported by Hoke et al. [75] For example, as noted above in relation to Fig. 4.21, the phase segregation induced by reverse bias results in a double layer structure within the perovskite layer with fairly uniform characteristics along the cell's lateral dimensions. This differs from the heterogeneous nucleation of iodine-rich domains observed under illumination by cathodoluminescence. [78] Another notable difference between the segregation driven by reverse bias as opposed to light concerns the kinetics of the process. [77] The images shown in Fig. 4.21 were acquired at a delay of one week after stress-testing the cells, so it is clear that bias-induced segregation lacks the reversibility of its light-driven counterpart (wherein segregation is often found to revert on a timescale of minutes to hours [77]). PL shifts also persisted for one week after reverse biasing. Notably, previous reports on current-induced phase segregation did not mention if the effect is reversible. [80] The difference in the self-diffusion rate that reverses the segregation may be related to the microstructural changes observed in our samples, in particular the irreversible appearance of a double layer microstructure (Fig. 4.21b and 4.22).

Bowring et al. [87] did not mention any phase segregation effect in their study on the reverse bias stability of $(FAPbI_3)_{0.83}(CsPbBr_3)_{0.17}$ cells. However, they did report I–V curves of a sample first degraded in the dark with a current of $-I_{mpp}$ and then recovered

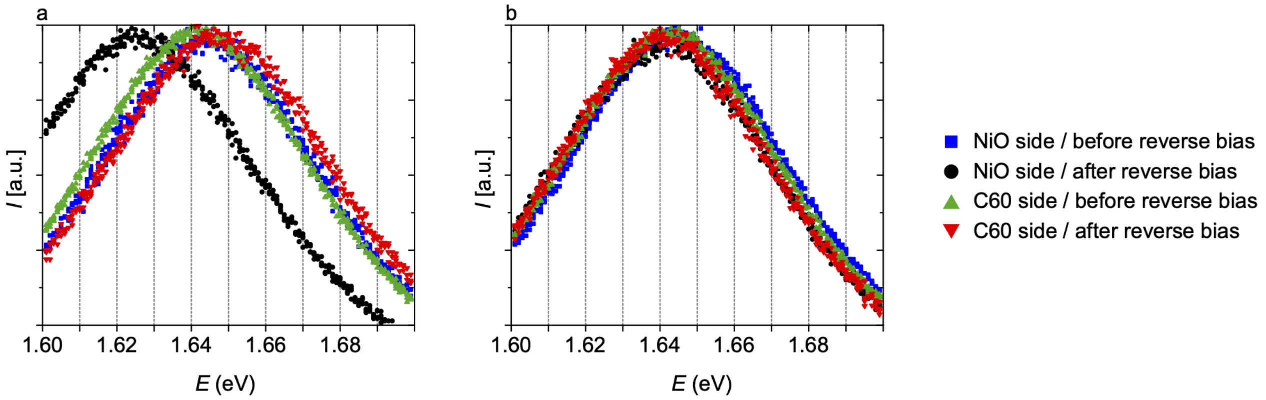

Figure 4.26: Normalized photoluminescence spectra measured from the NiO and C_{60} sides before and after reverse biasing at (a) -3 V and (b) -0.5 V for 15 min. In (a), a red-shift is measured on the NiO side, while a slight blue-shift is measured on the C_{60} side, inline with the elemental map of Fig. 4.21. No phase segregation is observed in (b) as the applied voltage is lower in absolute value than the breakdown voltage and hence no current flowed through the device.

at MPPT for 3 h. The I–V curve after recovery had a J_{sc} higher by at least 2 mAcm^{-2} and a V_{oc} lower by about 100 mV compared to before degradation. While the V_{oc} loss may be explained by an increase in bulk and/or surface recombination, the increase in J_{sc} is more difficult to explain without invoking a decrease in apparent bandgap (triggered by phase segregation). While not discussed explicitly, phase segregation is therefore consistent with their experiments as well. Furthermore, this speculation would indicate that reverse bias-induced phase segregation is not recoverable even after 3 h of MPPT, in agreement with our STEM EDX observation of irreversibly phase segregated layers.

In Fig. 4.29 we present a summary of the degradation mechanisms caused by reversed bias observed in this work.

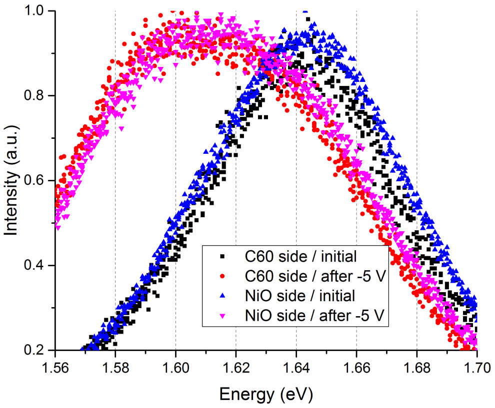

Figure 4.27: Normalized PL spectra of the perovskite taken from each side of a device degraded at −5 V for 30 min. A shift is observed after reverse biasing, irrespective of the side from which the spectrum is acquired.

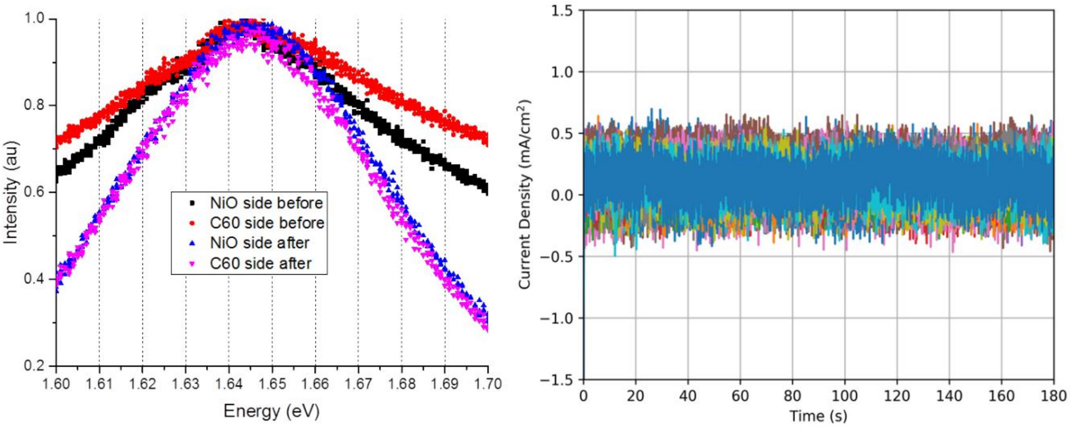

Figure 4.28: (Left panel) Normalized PL spectra comparing the perovskite before and after the reverse bias treatment shown in Figure 3a of the main text. Even though the S-shape was pronounced after reverse biasing, no bandgap shift and hence no phase segregation is observed, indicating that phase segregation is not the cause of the S-shape. (Right panel) Current as a function of time during the 3 min of reverse biasing for each step of the reverse bias protocol (0 V to −2 V in steps of −0.1 V) used in this work. The negligible current injected supports the fact that no phase segregation occurred in this sample.

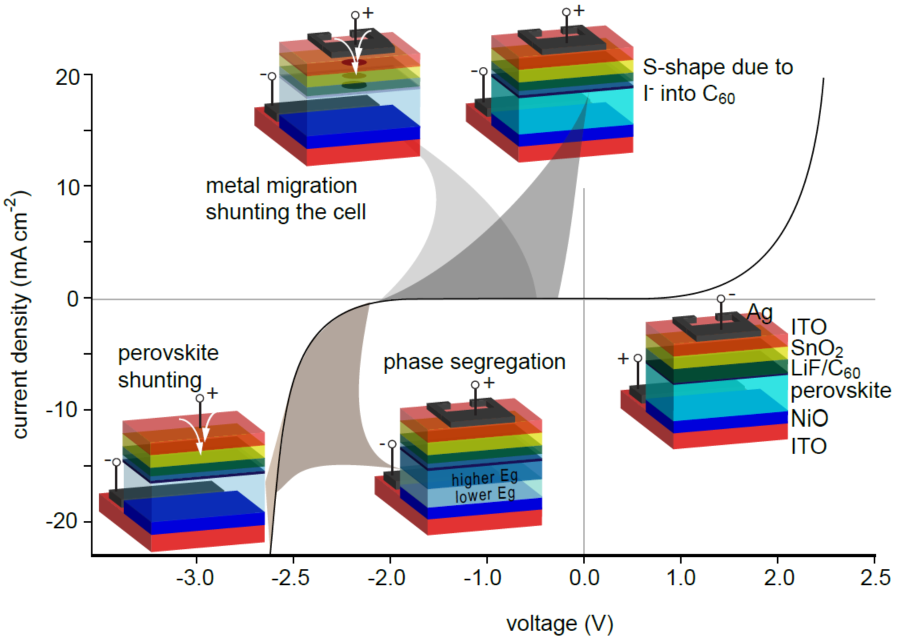

Figure 4.29: Summary of the degradation mechanisms occurring during reverse biasing as a function of the voltage range in which they occur. In this example, the breakdown voltage is -2 V, but in practice this value may range between -1 V and -4 V depending on solar cell design and processing conditions. The reverse voltages at which the mechanisms described here occur also depend on the cell design. The mechanisms are: 1) halogens being driven inside the C_{60} layer, which in our samples occurred for any reverse voltage applied; 2) shunt formation, which is voltage driven and becomes dominant for voltages higher than about -0.5 V; 3) phase segregation, which only occurs at voltages higher than the breakdown voltage, when current starts to flow through the perovskite; 4) shunt formation in the perovskite absorber, irrespective of the presence of the metal electrode.

Chapter 5

Conclusion

In this work we have presented results on many different structures of semiconductor devices. From the beginning, our goal was to learn more about heterojunctions and, in particular, their applications in perovskite solar cells. We feel this goal has been accomplished, although of course there is much more to learn about this rich field of applied physics.

We started by motivating research in solar energy, explaining why climate change demands clean energy sources. Then the current state of the art and the limits of photovoltaic technology were presented, demonstrating why it is necessary to develop tandem solar cells to achieve efficiencies beyond 30 %. The best promise so far for such tandems is those with Si as the bottom cell and perovskite as the top cell, but perovskite solar cells, although very efficient (record is currently 25.5 % in single junction), have many instabilities (e.g. water corrosion, current or light induced phase segregation, electrochemical reactions between layers) that still hinder its commercialization. The thesis then focused on these problems.

In Chapter 3 we described our method for fabricating perovskite solar cells. It starts by cleaning glass/ITO slides, then depositing the hole transport layer (in most cases 20 nm of NiO by sputtering), then the perovskite on top of it (always by spin coating), then the electron tansport layer (in most cases a double layer of 1 nm LiF and 20 nm C_{60} deposited by evaporation) and then the top electrode, which could be either a metal (Ag, Cu, Ni, Cr or Al) that covered the entire cell area, or it could be a SnO_2/ITO stack. The former results in an opaque solar cell, while the latter results in a semitransparent solar cell. The devices were then characterized by several electrical (e.g. current-voltage, capacitance-voltage, maximum powerpoint tracking) and optical (photoluminescence, dark lock-in thermography, external quantum efficiency), together with scanning and transmission electron microscopy.

In Sec. 4.1.1, we analyzed the behavior of different combinations of layers that are used in perovskite solar cells. These studies are important to understand the peculiarities of semiconductor layers before they are integrated in a complete device, where many effects are convoluted and it becomes hard to separate causes and effects. Methods for determining the hole/electron conduction characteristics of a given layer were shown. For example, TiO_2 was shown to be hole blocking and sufficiently electron conductive to be used as the ETL of a perovskite solar cell, while P3HT was shown to be electron blocking and sufficiently hole conductive. The electron conductivity of our TiO_2 layer (deposited by spin-coating) was about 4×10^{-6} Ω^{-1}cm^{-1}, which may seem low, but considering that the layer used in the perovskite cell has only $\sim$ 20 nm, the decrease in voltage that its series resistance causes is only of about 10 mV (about 1 % of the cell's voltage). Similar numbers for the hole conductivity of P3HT were also demonstrated.

Furthermore, a curious effect in the J-V curve of n-Si/TiO_2/Al was found during the studies of individual TiO_2 layers, as explained in Sec. 4.1.2. We published this effect and the explanation for it in Ref. [142]. It was related to how charges accumulate in the TiO_2 while current is passing through it, and how it affects the Si wafer underneath it. This effect had no direct consequence to the workings of perovskite solar cells, but we feel explaining it in detail gave us a much deeper understanding in the interplay between charge distribution and current conduction in semiconductor devices. This type of intuition is absolutely crucial when developing semiconductor devices such as solar cells.

In Sec. 4.2, complete perovskite solar cells were described. Two types of structures were studied, opaque solar cells (ITO/NiO/PK/LiF/C_{60}/Ag) and semitransparent solar cells (ITO/NiO/PK/LiF/C_{60}/SnO_2/ITO/Ag). Semitransparent cells are less efficient (efficiency of 10-11 %, compared to 13-15 % for opaque), as expected, but are compatible with Si/perovskite tandems. The reason it is less efficient is because it absorbs less light and because the SnO_2/ITO stack introduces more series resistance. Furthermore, the subtle dependencies of device performance on deposition conditions, such as the application of antisolvent during the PK layer deposition, were shown. Cells with different layers, such as PTAA as the HTL and other metals as electrodes, were also analyzed. PTAA was shown to be much more efficient at extracting holes and blocking electrons than NiO, with a record cell efficiency of 16.9 %. However, since it is deposited by spin-coating, it cannot be used in textured Si/perovskite tandems.

Many of these results were compared with simulations, which were very helpful on determining the possible causes of inefficiencies. For example, it was shown that if all recombination mechanisms besides radiative are suppressed, the cell's voltage can be as high as 1.18 V (for a 1.55 eV bandgap absorber), while the best voltage obtained was 1.09 V. The best possible current is 25.1 mA/cm^2 if no reflection and parasitic absorption is present, while the best current obtained was 20.7 mA/cm^2. These results point to how performance can be improved in future research.

Perhaps the experiments that rendered the most impact in perovskite solar cell research were those on reverse bias stability (Sec. 4.3). These experiments showed how perovskite cells break down when a reverse voltage is applied (which in the field would be caused by partial shading of modules), and corroborated many other studies by other authors. Unfortunately, voltages as low as -0.3 V for opaque and -1.2 V for semitransparent solar cells are already enough to trigger damages. The reasons for this instability involve at least four different mechanisms, such as metal migration from the electrodes into the perovskite, electrochemical reactions of the perovskite with the adjacent organic layer, phase segregation caused by current injection and a voltage induced conversion of the perovskite into metallic Pb. We published these results in Ref. [72]. These results had both good news and bad news associated with them. The bad news is that perovskite cells have a serious problem with stability, and the technology will not reach the market before these problems are solved. The good news is that the problems are becoming understood, which is the first step towards finding a solution.

Finally, it is mentioned that all the results of complete solar cells (Sec. 4.2) were obtained for devices fabricated at EPFL in Switzerland. We actually made a couple of batches of complete solar cells using TiO_2 and P3HT at UFRGS after the author came back to Brazil, but the devices were very inefficient and we felt the results were not worth including in the final thesis. The plan was to debug this structure until we achieved a reasonably working device fabricated in Brazil. However, the restrictions caused by the COVID-19 pandemic were too severe for us to continue these experiments. From then on we focused on simulations to explain the results already obtained.

Acknowledgements

This thesis and the work it took to create it would not have been possible without the help of many other scientists. First, I must mention that I'm forever in debpt to my advisor Henri Boudinov, if not for his incredible mastery of semiconductor physics and technology and his teaching skills, for his constant excitement with physics research that keeps students like myself motivated. Second, I thank Quentin Jeangros, my supervisor during my year in PV-lab in Switzerland. I still struggle in understanding how I got so lucky as to find such a smart, understanding and fun supervisor to work with about 10.000 km away from my home. Third, I thank the boss of PV-lab Christophe Ballif, a leading figure in the world's PV research, for accepting me in his lab and making me part of his team while I was there. Last but not least, all my co-workers and friends, both in Brazil and in Switzerland, were also central to my personal development and to that of my research when discussing day-to-day problems and aspirations. Admitting that I will forget many names, I would like to mention Frâncio Rodrigues, Ivan Kaufmann, João Abal, Daniel Jacobs, Peter Fiala, Florent Sahli, Jonathan Thomet, Olatz Arriaga, Yashi Xiao, Sofia Libraro, Assunta Scognamillo and Niccolo Salsi. I hope I get to work with you again someday.

I finish by mentioning that I've always had far better parents than I deserve. In the end, everything I do is a consequence of how you raised me and, perhaps ironically but not paradoxically, nothing makes me more proud of myself.

Bibliography

[1] M. E. Caldeira, Ken; Wickett, “Oceanography: Anthropogenic carbon and ocean ph,” *Nature*, vol. 425, p. 365, 2003.

[2] C. Mora et al., “Biotic and human vulnerability to projected changes in ocean biogeochemistry over the 21st century,” *PLoS Biology*, vol. 11, no. 10, 2013.

[3] A. A. Lacis, G. A. Schmidt, D. Rind, and R. A. Ruedy, “Atmospheric co2: Principal control knob governing earth’s temperature,” *Science*, vol. 330, no. 6002, pp. 356–359, 2010. [Online]. Available: https://science.sciencemag.org/content/330/6002/356

[4] L. Kaplan, “On the pressure dependence of radiative heat transfer in the atmosphere,” *Journal of Meteorology*, vol. 9, no. 1, 1952.

[5] P. Würfel, *Physics of Solar Cells.* Wiley, jan 2005. [Online]. Available: https://onlinelibrary.wiley.com/doi/book/10.1002/9783527618545

[6] J. H. Davies and D. R. Davies, “Earth’s surface heat flux,” *Solid Earth*, vol. 1, no. 1, pp. 5–24, feb 2010. [Online]. Available: https://www.solid-earth.net/1/5/2010/

[7] P. D. Jones, “Climate over past millennia,” *Reviews of Geophysics*, vol. 42, no. 2, p. RG2002, 2004. [Online]. Available: http://doi.wiley.com/10.1029/2003RG000143

[8] R. T. Pierrehumbert, D. Hafemeister, D. Kammen, B. G. Levi, and P. Schwartz, “Infrared Radiation and Planetary Temperature,” 2011, pp. 232–244. [Online]. Available: http://aip.scitation.org/doi/abs/10.1063/1.3653855

[9] NOAA, “Recent Daily Average Mauna Loa CO2,” 2020. [Online]. Available: https://www.esrl.noaa.gov/gmd/ccgg/trends/monthly.html

[10] M. Collins, J. R. Knutti, J.-L. Arblaster, T. Dufresne, X. Fichefet, P. Friedlingstein, W. Gao, T. Gutowski, G. Johns, M. Krinner, C. Shongwe, A. Tebaldi, W. Wehner, and M., “Long-term Climate Change: Projections, Commitments and Irreversibility,” in *Climate Change 2013: The Physical Science Basis.* Cambridge, United Kingdom and New York, NY, USA: Cambridge University Press, 2013, p. 108.

[11] K. Pistone, I. Eisenman, and V. Ramanathan, “Radiative Heating of an Ice-Free Arctic Ocean,” *Geophysical Research Letters*, vol. 46, no. 13, pp. 7474–7480, jul 2019. [Online]. Available: https://onlinelibrary.wiley.com/doi/abs/10.1029/2019GL082914

[12] S. A. Zimov, "CLIMATE CHANGE: Permafrost and the Global Carbon Budget," *Science*, vol. 312, no. 5780, pp. 1612–1613, jun 2006. [Online]. Available: https://www.sciencemag.org/lookup/doi/10.1126/science.1128908

[13] R. Wiebe and V. L. Gaddy, "The Solubility of Carbon Dioxide in Water at Various Temperatures from 12 to 40° and at Pressures to 500 Atmospheres. Critical Phenomena *," *Journal of the American Chemical Society*, vol. 62, no. 4, pp. 815–817, apr 1940. [Online]. Available: https://pubs.acs.org/doi/abs/10.1021/ja01861a033

[14] J. M. Hayes, "Fractionation of Carbon and Hydrogen Isotopes in Biosynthetic Processes," *Reviews in Mineralogy and Geochemistry*, vol. 43, no. 1, pp. 225–277, jan 2001. [Online]. Available: https://pubs.geoscienceworld.org/rimg/article/43/1/225-277/140680

[15] M. Rubino, D. M. Etheridge, C. M. Trudinger, C. E. Allison, M. O. Battle, R. L. Langenfelds, L. P. Steele, M. Curran, M. Bender, J. W. C. White, T. M. Jenk, T. Blunier, and R. J. Francey, "A revised 1000 year atmospheric δ 13 C-CO 2 record from Law Dome and South Pole, Antarctica," *Journal of Geophysical Research: Atmospheres*, vol. 118, no. 15, pp. 8482–8499, aug 2013. [Online]. Available: http://doi.wiley.com/10.1002/jgrd.50668

[16] D. Lüthi, M. Le Floch, B. Bereiter, T. Blunier, J.-M. Barnola, U. Siegenthaler, D. Raynaud, J. Jouzel, H. Fischer, K. Kawamura, and T. F. Stocker, "High-resolution carbon dioxide concentration record 650,000–800,000 years before present," *Nature*, vol. 453, no. 7193, pp. 379–382, may 2008. [Online]. Available: http://www.nature.com/articles/nature06949

[17] BP, "Statistical Review of World Energy," Tech. Rep., 2019. [Online]. Available: https://www.bp.com/content/dam/bp/business-sites/en/global/corporate/pdfs/energy-economics/statistical-review/bp-stats-review-2019-full-report.pdf

[18] B. P. Tissot and D. H. Welte, *Petroleum Formation and Occurrence.* Berlin, Heidelberg: Springer Berlin Heidelberg, 1984. [Online]. Available: http://link.springer.com/10.1007/978-3-642-87813-8

[19] Y. M. Bar-On, R. Phillips, and R. Milo, "The biomass distribution on Earth," *Proceedings of the National Academy of Sciences*, vol. 115, no. 25, pp. 6506–6511, jun 2018. [Online]. Available: http://www.pnas.org/lookup/doi/10.1073/pnas.1711842115

[20] IEA, "International Energy Agency - Data and Statistics," 2020. [Online]. Available: https://www.iea.org/data-and-statistics

[21] H. Horvath, "Atmospheric light absorption—A review," *Atmospheric Environment. Part A. General Topics*, vol. 27, no. 3, pp. 293–317, feb 1993.

[22] R. Hulstrom, R. Bird, and C. Riordan, "Spectral solar irradiance data sets for selected terrestrial conditions," *Solar Cells*, vol. 15, no. 4, pp. 365–391, dec 1985.

[23] Agency for Natural Resources and Energy, “Summary for Policymakers,” in *Climate Change 2013 - The Physical Science Basis*, Intergovernmental Panel on Climate Change, Ed. Cambridge: Cambridge University Press, 2017, pp. 1–30.

[24] K. Bleich and R. D. Guimaraes, “Renewable Infrastructure Investment Handbook: A Guide for Institutional Investors,” *World Economic Forum Industry Agenda*, no. December, p. 43, 2016.

[25] ITRPV, “International technology roadmap for photovoltaics - 2017 results,” 2018. [Online]. Available: http://www.itrpv.net/Reports/Downloads/

[26] G. Kavlak, J. McNerney, and J. E. Trancik, “Evaluating the causes of cost reduction in photovoltaic modules,” *Energy Policy*, vol. 123, pp. 700–710, dec 2018. [Online]. Available: https://linkinghub.elsevier.com/retrieve/pii/S0301421518305196

[27] K. Yoshikawa, H. Kawasaki, W. Yoshida, T. Irie, K. Konishi, K. Nakano, T. Uto, D. Adachi, M. Kanematsu, H. Uzu, and K. Yamamoto, “Silicon heterojunction solar cell with interdigitated back contacts for a photoconversion efficiency over 26%,” *Nature Energy*, vol. 2, no. 5, p. 17032, mar 2017.

[28] L. C. Hirst and N. J. Ekins-Daukes, “Fundamental losses in solar cells,” *Progress in Photovoltaics: Research and Applications*, vol. 19, no. 3, pp. 286–293, may 2011.

[29] P. T. Landsberg and G. Tonge, “Thermodynamic energy conversion efficiencies,” *Journal of Applied Physics*, vol. 51, no. 7, pp. R1–R20, jul 1980.

[30] A. Martí and G. L. Araújo, “Limiting efficiencies for photovoltaic energy conversion in multigap systems,” *Solar Energy Materials and Solar Cells*, vol. 43, no. 2, pp. 203–222, sep 1996.

[31] A. Luque and S. Hegedus, *Handbook of Photovoltaics.* West Sussex, England: John Wiley & Sons, Ltd, 2003.

[32] W. Shockley and H. J. Queisser, “Detailed Balance Limit of Efficiency of p-n Junction Solar Cells,” *Journal of Applied Physics*, vol. 32, no. 3, pp. 510–519, mar 1961.

[33] A. Richter, M. Hermle, and S. W. Glunz, “Reassessment of the Limiting Efficiency for Crystalline Silicon Solar Cells,” *IEEE Journal of Photovoltaics*, vol. 3, no. 4, pp. 1184–1191, oct 2013.

[34] NREL, “Best-research cell efficiencies chart,” 2018. [Online]. Available: https://www.nrel.gov/pv/assets/images/efficiency-chart.png

[35] M. A. Green, A. Ho-Baillie, and H. J. Snaith, “The emergence of perovskite solar cells,” *Nature Photonics*, vol. 8, no. 7, pp. 506–514, jul 2014.

[36] M. A. Green and A. Ho-Baillie, “Perovskite Solar Cells: The Birth of a New Era in Photovoltaics,” *ACS Energy Letters*, vol. 2, no. 4, pp. 822–830, apr 2017.

[37] T. Leijtens, K. Bush, R. Cheacharoen, R. Beal, A. Bowring, and M. D. McGehee, “Towards enabling stable lead halide perovskite solar cells; interplay between structural, environmental, and thermal stability,” *Journal of Materials Chemistry A*, vol. 5, no. 23, pp. 11 483–11 500, 2017.

[38] N.-G. Park, “Perovskite solar cells: an emerging photovoltaic technology,” *Materials Today*, vol. 18, no. 2, pp. 65–72, mar 2015.

[39] C. Quarti, E. Mosconi, J. M. Ball, V. D’Innocenzo, C. Tao, S. Pathak, H. J. Snaith, A. Petrozza, and F. De Angelis, “Structural and optical properties of methylammonium lead iodide across the tetragonal to cubic phase transition: implications for perovskite solar cells,” *Energy & Environmental Science*, vol. 9, no. 1, pp. 155–163, 2016. [Online]. Available: http://xlink.rsc.org/?DOI=C5EE02925B

[40] C. Eames, J. M. Frost, P. R. F. Barnes, B. C. O’Regan, A. Walsh, and M. S. Islam, “Ionic transport in hybrid lead iodide perovskite solar cells,” *Nature Communications*, vol. 6, no. 1, p. 7497, nov 2015. [Online]. Available: http://www.nature.com/articles/ncomms8497

[41] H. Tsai, W. Nie, J.-C. Blancon, C. C. Stoumpos, R. Asadpour, B. Harutyunyan, A. J. Neukirch, R. Verduzco, J. J. Crochet, S. Tretiak, L. Pedesseau, J. Even, M. A. Alam, G. Gupta, J. Lou, P. M. Ajayan, M. J. Bedzyk, M. G. Kanatzidis, and A. D. Mohite, “High-efficiency two-dimensional Ruddlesden–Popper perovskite solar cells,” *Nature*, vol. 536, no. 7616, pp. 312–316, aug 2016.

[42] D. B. Mitzi, “Templating and structural engineering in organic–inorganic perovskites,” *Journal of the Chemical Society, Dalton Transactions*, no. 1, pp. 1–12, 2001.

[43] M. Saliba, T. Matsui, K. Domanski, J.-Y. Seo, A. Ummadisingu, S. M. Zakeeruddin, J.-P. Correa-Baena, W. R. Tress, A. Abate, A. Hagfeldt, and M. Gratzel, “Incorporation of rubidium cations into perovskite solar cells improves photovoltaic performance,” *Science*, vol. 354, no. 6309, pp. 206–209, oct 2016. [Online]. Available: https://www.sciencemag.org/lookup/doi/10.1126/science.aah5557

[44] M. Abdi-Jalebi, Z. Andaji-Garmaroudi, S. Cacovich, C. Stavrakas, B. Philippe, J. M. Richter, M. Alsari, E. P. Booker, E. M. Hutter, A. J. Pearson, S. Lilliu, T. J. Savenije, H. Rensmo, G. Divitini, C. Ducati, R. H. Friend, and S. D. Stranks, “Maximizing and stabilizing luminescence from halide perovskites with potassium passivation,” *Nature*, vol. 555, no. 7697, pp. 497–501, mar 2018. [Online]. Available: http://www.nature.com/articles/nature25989

[45] M. R. Filip, G. Volonakis, and F. Giustino, “Hybrid Halide Perovskites: Fundamental Theory and Materials Design,” in *Handbook of Materials Modeling.* Cham: Springer International Publishing, 2018, pp. 1–30. [Online]. Available: http://link.springer.com/10.1007/978-3-319-50257-1_23-1

[46] N.-G. Park, M. Grätzel, and T. Miyasaka, Eds., *Organic-Inorganic Halide Perovskite Photovoltaics.* Cham: Springer International Publishing, 2016. [Online]. Available: http://link.springer.com/10.1007/978-3-319-35114-8

[47] W.-J. Yin, T. Shi, and Y. Yan, “Unique Properties of Halide Perovskites as Possible Origins of the Superior Solar Cell Performance,” *Advanced Materials*, vol. 26, no. 27, pp. 4653–4658, jul 2014. [Online]. Available: http://doi.wiley.com/10.1002/adma.201306281

[48] A. Amat, E. Mosconi, E. Ronca, C. Quarti, P. Umari, M. K. Nazeeruddin, M. Grätzel, and F. De Angelis, “Cation-Induced Band-Gap Tuning in Organohalide Perovskites: Interplay of Spin–Orbit Coupling and Octahedra Tilting,” *Nano Letters*, vol. 14, no. 6, pp. 3608–3616, jun 2014. [Online]. Available: https://pubs.acs.org/doi/10.1021/nl5012992

[49] J. H. Noh, S. H. Im, J. H. Heo, T. N. Mandal, and S. I. Seok, “Chemical Management for Colorful, Efficient, and Stable Inorganic–Organic Hybrid Nanostructured Solar Cells,” *Nano Letters*, vol. 13, no. 4, pp. 1764–1769, apr 2013. [Online]. Available: https://pubs.acs.org/doi/10.1021/nl400349b

[50] D. P. McMeekin, G. Sadoughi, W. Rehman, G. E. Eperon, M. Saliba, M. T. Horantner, A. Haghighirad, N. Sakai, L. Korte, B. Rech, M. B. Johnston, L. M. Herz, and H. J. Snaith, “A mixed-cation lead mixed-halide perovskite absorber for tandem solar cells,” *Science*, vol. 351, no. 6269, pp. 151–155, jan 2016. [Online]. Available: https://www.sciencemag.org/lookup/doi/10.1126/science.aad5845

[51] K. A. Bush, K. Frohna, R. Prasanna, R. E. Beal, T. Leijtens, S. A. Swifter, and M. D. McGehee, “Compositional Engineering for Efficient Wide Band Gap Perovskites with Improved Stability to Photoinduced Phase Segregation,” *ACS Energy Letters*, vol. 3, no. 2, pp. 428–435, feb 2018. [Online]. Available: https://pubs.acs.org/doi/10.1021/acsenergylett.7b01255

[52] J. M. Ball and A. Petrozza, “Defects in perovskite-halides and their effects in solar cells,” *Nature Energy*, vol. 1, no. 11, p. 16149, nov 2016. [Online]. Available: http://www.nature.com/articles/nenergy2016149

[53] W. Shockley and W. T. Read, “Statistics of the Recombinations of Holes and Electrons,” *Physical Review*, vol. 87, no. 5, pp. 835–842, sep 1952.

[54] X. Zhang, M. E. Turiansky, and C. G. Van de Walle, “Correctly Assessing Defect Tolerance in Halide Perovskites,” *The Journal of Physical Chemistry C*, vol. 124, no. 11, pp. 6022–6027, mar 2020. [Online]. Available: https://pubs.acs.org/doi/abs/10.1021/acs.jpcc.0c01324

[55] J. Beilsten-Edmands, G. E. Eperon, R. D. Johnson, H. J. Snaith, and P. G. Radaelli, “Non-ferroelectric nature of the conductance hysteresis in CH 3 NH 3 PbI 3 perovskite-based photovoltaic devices,” *Applied Physics Letters*, vol. 106, no. 17, p. 173502, apr 2015. [Online]. Available: http://aip.scitation.org/doi/10.1063/1.4919109

[56] J. M. Frost, K. T. Butler, F. Brivio, C. H. Hendon, M. van Schilfgaarde, and A. Walsh, “Atomistic Origins of High-Performance in Hybrid Halide Perovskite Solar Cells,” *Nano Letters*, vol. 14, no. 5, pp. 2584–2590, may 2014.

[57] C. Li, S. Tscheuschner, F. Paulus, P. E. Hopkinson, J. Kießling, A. Köhler, Y. Vaynzof, and S. Huettner, "Iodine Migration and its Effect on Hysteresis in Perovskite Solar Cells," *Advanced Materials*, vol. 28, no. 12, pp. 2446–2454, mar 2016. [Online]. Available: http://doi.wiley.com/10.1002/adma.201503832

[58] Y. Yuan, J. Chae, Y. Shao, Q. Wang, Z. Xiao, A. Centrone, and J. Huang, "Photovoltaic Switching Mechanism in Lateral Structure Hybrid Perovskite Solar Cells," *Advanced Energy Materials*, vol. 5, no. 15, p. 1500615, aug 2015. [Online]. Available: http://doi.wiley.com/10.1002/aenm.201500615

[59] D. W. DeQuilettes, W. Zhang, V. M. Burlakov, D. J. Graham, T. Leijtens, A. Osherov, V. Bulović, H. J. Snaith, D. S. Ginger, and S. D. Stranks, "Photo-induced halide redistribution in organic–inorganic perovskite films," *Nature Communications*, vol. 7, no. 1, p. 11683, sep 2016. [Online]. Available: http://www.nature.com/articles/ncomms11683

[60] Y. Shao, Y. Fang, T. Li, Q. Wang, Q. Dong, Y. Deng, Y. Yuan, H. Wei, M. Wang, A. Gruverman, J. Shield, and J. Huang, "Grain boundary dominated ion migration in polycrystalline organic–inorganic halide perovskite films," *Energy & Environmental Science*, vol. 9, no. 5, pp. 1752–1759, 2016. [Online]. Available: http://xlink.rsc.org/?DOI=C6EE00413J

[61] S. De Wolf, J. Holovsky, S.-J. Moon, P. Löper, B. Niesen, M. Ledinsky, F.-J. Haug, J.-H. Yum, and C. Ballif, "Organometallic Halide Perovskites: Sharp Optical Absorption Edge and Its Relation to Photovoltaic Performance," *The Journal of Physical Chemistry Letters*, vol. 5, no. 6, pp. 1035–1039, mar 2014.

[62] W. S. Yang, J. H. Noh, N. J. Jeon, Y. C. Kim, S. Ryu, J. Seo, and S. I. Seok, "High-performance photovoltaic perovskite layers fabricated through intramolecular exchange," *Science*, vol. 348, no. 6240, pp. 1234–1237, jun 2015.

[63] N. Arora, M. I. Dar, A. Hinderhofer, N. Pellet, F. Schreiber, S. M. Zakeeruddin, and M. Grätzel, "Perovskite solar cells with CuSCN hole extraction layers yield stabilized efficiencies greater than 20%," *Science*, vol. 358, no. 6364, pp. 768–771, nov 2017.

[64] C. Momblona, L. Gil-Escrig, E. Bandiello, E. M. Hutter, M. Sessolo, K. Lederer, J. Blochwitz-Nimoth, and H. J. Bolink, "Efficient vacuum deposited p-i-n and n-i-p perovskite solar cells employing doped charge transport layers," *Energy Environ. Sci.*, vol. 9, no. 11, pp. 3456–3463, 2016.

[65] Q. Jeangros, M. Duchamp, J. Werner, M. Kruth, R. E. Dunin-Borkowski, B. Niesen, C. Ballif, and A. Hessler-Wyser, "In Situ TEM Analysis of Organic–Inorganic Metal-Halide Perovskite Solar Cells under Electrical Bias," *Nano Letters*, vol. 16, no. 11, pp. 7013–7018, nov 2016.

[66] N. Aristidou, I. Sanchez-Molina, T. Chotchuangchutchaval, M. Brown, L. Martinez, T. Rath, and S. A. Haque, "The Role of Oxygen in the Degradation of Methylammonium Lead Trihalide Perovskite Photoactive Layers," *Angewandte Chemie International Edition*, vol. 54, no. 28, pp. 8208–8212, jul 2015.

[67] T. Leijtens, G. E. Eperon, N. K. Noel, S. N. Habisreutinger, A. Petrozza, and H. J. Snaith, “Stability of Metal Halide Perovskite Solar Cells,” *Advanced Energy Materials*, vol. 5, no. 20, p. 1500963, oct 2015.

[68] T. A. Berhe, W.-N. Su, C.-H. Chen, C.-J. Pan, J.-H. Cheng, H.-M. Chen, M.-C. Tsai, L.-Y. Chen, A. A. Dubale, and B.-J. Hwang, “Organometal halide perovskite solar cells: degradation and stability,” *Energy & Environmental Science*, vol. 9, no. 2, pp. 323–356, 2016.

[69] A. Dualeh, P. Gao, S. I. Seok, M. K. Nazeeruddin, and M. Grätzel, “Thermal Behavior of Methylammonium Lead-Trihalide Perovskite Photovoltaic Light Harvesters,” *Chemistry of Materials*, vol. 26, no. 21, pp. 6160–6164, nov 2014.

[70] K. Domanski, J.-P. Correa-Baena, N. Mine, M. K. Nazeeruddin, A. Abate, M. Saliba, W. Tress, A. Hagfeldt, and M. Grätzel, “Not All That Glitters Is Gold: Metal-Migration-Induced Degradation in Perovskite Solar Cells,” *ACS Nano*, vol. 10, no. 6, pp. 6306–6314, jun 2016.

[71] G. E. Eperon, S. D. Stranks, C. Menelaou, M. B. Johnston, L. M. Herz, and H. J. Snaith, “Formamidinium lead trihalide: a broadly tunable perovskite for efficient planar heterojunction solar cells,” *Energy & Environmental Science*, vol. 7, no. 3, p. 982, 2014.

[72] R. A. Z. Razera, D. A. Jacobs, F. Fu, P. Fiala, M. Dussouillez, F. Sahli, T. C. J. Yang, L. Ding, A. Walter, A. F. Feil, H. I. Boudinov, S. Nicolay, C. Ballif, and Q. Jeangros, “Instability of p–i–n perovskite solar cells under reverse bias,” *Journal of Materials Chemistry A*, vol. 8, no. 1, pp. 242–250, 2020. [Online]. Available: http://xlink.rsc.org/?DOI=C9TA12032G

[73] K. A. Bush, C. D. Bailie, Y. Chen, A. R. Bowring, W. Wang, W. Ma, T. Leijtens, F. Moghadam, and M. D. McGehee, “Thermal and Environmental Stability of Semi-Transparent Perovskite Solar Cells for Tandems Enabled by a Solution-Processed Nanoparticle Buffer Layer and Sputtered ITO Electrode,” *Advanced Materials*, vol. 28, no. 20, pp. 3937–3943, may 2016.

[74] A. Mei, X. Li, L. Liu, Z. Ku, T. Liu, Y. Rong, M. Xu, M. Hu, J. Chen, Y. Yang, M. Gratzel, and H. Han, “A hole-conductor-free, fully printable mesoscopic perovskite solar cell with high stability,” *Science*, vol. 345, no. 6194, pp. 295–298, jul 2014.

[75] E. T. Hoke, D. J. Slotcavage, E. R. Dohner, A. R. Bowring, H. I. Karunadasa, and M. D. McGehee, “Reversible photo-induced trap formation in mixed-halide hybrid perovskites for photovoltaics,” *Chemical Science*, vol. 6, no. 1, pp. 613–617, 2015. [Online]. Available: http://xlink.rsc.org/?DOI=C4SC03141E

[76] T. Duong, H. K. Mulmudi, Y. Wu, X. Fu, H. Shen, J. Peng, N. Wu, H. T. Nguyen, D. Macdonald, M. Lockrey, T. P. White, K. Weber, and K. Catchpole, “Light and Electrically Induced Phase Segregation and Its Impact on the Stability of Quadruple Cation High Bandgap Perovskite Solar Cells,” *ACS Applied Materials*

& Interfaces, vol. 9, no. 32, pp. 26 859–26 866, aug 2017. [Online]. Available: https://pubs.acs.org/doi/10.1021/acsami.7b06816

[77] S. Draguta, O. Sharia, S. J. Yoon, M. C. Brennan, Y. V. Morozov, J. S. Manser, P. V. Kamat, W. F. Schneider, and M. Kuno, "Rationalizing the light-induced phase separation of mixed halide organic–inorganic perovskites," *Nature Communications*, vol. 8, no. 1, p. 200, dec 2017. [Online]. Available: http://www.nature.com/articles/s41467-017-00284-2

[78] C. G. Bischak, C. L. Hetherington, H. Wu, S. Aloni, D. F. Ogletree, D. T. Limmer, and N. S. Ginsberg, "Origin of Reversible Photoinduced Phase Separation in Hybrid Perovskites," *Nano Letters*, vol. 17, no. 2, pp. 1028–1033, feb 2017. [Online]. Available: https://pubs.acs.org/doi/10.1021/acs.nanolett.6b04453

[79] A. J. Barker, A. Sadhanala, F. Deschler, M. Gandini, S. P. Senanayak, P. M. Pearce, E. Mosconi, A. J. Pearson, Y. Wu, A. R. Srimath Kandada, T. Leijtens, F. De Angelis, S. E. Dutton, A. Petrozza, and R. H. Friend, "Defect-Assisted Photoinduced Halide Segregation in Mixed-Halide Perovskite Thin Films," *ACS Energy Letters*, vol. 2, no. 6, pp. 1416–1424, jun 2017. [Online]. Available: https://pubs.acs.org/doi/10.1021/acsenergylett.7b00282

[80] I. L. Braly, R. J. Stoddard, A. Rajagopal, A. R. Uhl, J. K. Katahara, A. K.-Y. Jen, and H. W. Hillhouse, "Current-Induced Phase Segregation in Mixed Halide Hybrid Perovskites and its Impact on Two-Terminal Tandem Solar Cell Design," *ACS Energy Letters*, vol. 2, no. 8, pp. 1841–1847, aug 2017. [Online]. Available: https://pubs.acs.org/doi/10.1021/acsenergylett.7b00525

[81] R. A. Belisle, K. A. Bush, L. Bertoluzzi, A. Gold-Parker, M. F. Toney, and M. D. McGehee, "Impact of Surfaces on Photoinduced Halide Segregation in Mixed-Halide Perovskites," *ACS Energy Letters*, vol. 3, no. 11, pp. 2694–2700, nov 2018. [Online]. Available: https://pubs.acs.org/doi/10.1021/acsenergylett.8b01562

[82] J. Xu, C. C. Boyd, Z. J. Yu, A. F. Palmstrom, D. J. Witter, B. W. Larson, R. M. France, J. Werner, S. P. Harvey, E. J. Wolf, W. Weigand, S. Manzoor, M. F. A. M. van Hest, J. J. Berry, J. M. Luther, Z. C. Holman, and M. D. McGehee, "Triple-halide wide–band gap perovskites with suppressed phase segregation for efficient tandems," *Science*, vol. 367, no. 6482, pp. 1097–1104, mar 2020. [Online]. Available: https://www.sciencemag.org/lookup/doi/10.1126/science.aaz5074

[83] S. Daliento, F. Di Napoli, P. Guerriero, and V. D'Alessandro, "A modified bypass circuit for improved hot spot reliability of solar panels subject to partial shading," *Solar Energy*, vol. 134, pp. 211–218, sep 2016. [Online]. Available: https://linkinghub.elsevier.com/retrieve/pii/S0038092X16300810

[84] B. B. Pannebakker, A. C. de Waal, and W. G. van Sark, "Photovoltaics in the shade: one bypass diode per solar cell revisited," *Progress in Photovoltaics: Research and Applications*, vol. 25, no. 10, pp. 836–849, oct 2017. [Online]. Available: http://doi.wiley.com/10.1002/pip.2898

[85] A. Woyte, J. Nijs, and R. Belmans, "Partial shadowing of photovoltaic arrays with different system configurations: literature review and field test results," *Solar Energy*, vol. 74, no. 3, pp. 217–233, mar 2003. [Online]. Available: https://linkinghub.elsevier.com/retrieve/pii/S0038092X03001555

[86] M. Köntges, "Review of Failures of Photovoltaic Modules," IEA, Tech. Rep., 2014.

[87] A. R. Bowring, L. Bertoluzzi, B. C. O'Regan, and M. D. McGehee, "Reverse Bias Behavior of Halide Perovskite Solar Cells," *Advanced Energy Materials*, vol. 8, no. 8, p. 1702365, mar 2018.

[88] J. Werner, E. J. Wolf, C. C. Boyd, M. F. A. M. van Hest, J. M. Luther, K. Zhu, J. J. Berry, and M. D. McGehee, "Learning from existing photovoltaic technologies to identify alternative perovskite module designs," *Energy & Environmental Science*, 2020. [Online]. Available: http://pubs.rsc.org/en/Content/ArticleLanding/2020/EE/D0EE01923B

[89] A. Kojima, K. Teshima, Y. Shirai, and T. Miyasaka, "Organometal Halide Perovskites as Visible-Light Sensitizers for Photovoltaic Cells," *Journal of the American Chemical Society*, vol. 131, no. 17, pp. 6050–6051, may 2009.

[90] H.-S. Kim, C.-R. Lee, J.-H. Im, K.-B. Lee, T. Moehl, A. Marchioro, S.-J. Moon, R. Humphry-Baker, J.-H. Yum, J. E. Moser, M. Grätzel, and N.-G. Park, "Lead Iodide Perovskite Sensitized All-Solid-State Submicron Thin Film Mesoscopic Solar Cell with Efficiency Exceeding 9%," *Scientific Reports*, vol. 2, no. 1, p. 591, dec 2012.

[91] M. M. Lee, J. Teuscher, T. Miyasaka, T. N. Murakami, and H. J. Snaith, "Efficient Hybrid Solar Cells Based on Meso-Superstructured Organometal Halide Perovskites," *Science*, vol. 338, no. 6107, pp. 643–647, nov 2012.

[92] V. D'Innocenzo, G. Grancini, M. J. P. Alcocer, A. R. S. Kandada, S. D. Stranks, M. M. Lee, G. Lanzani, H. J. Snaith, and A. Petrozza, "Excitons versus free charges in organo-lead tri-halide perovskites," *Nature Communications*, vol. 5, no. 1, p. 3586, dec 2014.

[93] Q. Lin, A. Armin, R. C. R. Nagiri, P. L. Burn, and P. Meredith, "Electro-optics of perovskite solar cells," *Nature Photonics*, vol. 9, no. 2, pp. 106–112, feb 2015.

[94] J. Burschka, N. Pellet, S.-J. Moon, R. Humphry-Baker, P. Gao, M. K. Nazeeruddin, and M. Grätzel, "Sequential deposition as a route to high-performance perovskite-sensitized solar cells," *Nature*, vol. 499, no. 7458, pp. 316–319, jul 2013.

[95] M. Liu, M. B. Johnston, and H. J. Snaith, "Efficient planar heterojunction perovskite solar cells by vapour deposition," *Nature*, vol. 501, no. 7467, pp. 395–398, sep 2013.

[96] N. J. Jeon, J. H. Noh, Y. C. Kim, W. S. Yang, S. Ryu, and S. I. Seok, "Solvent engineering for high-performance inorganic–organic hybrid perovskite solar cells," *Nature Materials*, vol. 13, no. 9, pp. 897–903, sep 2014.

[97] H. J. Snaith and P. Hacke, "Enabling reliability assessments of pre-commercial perovskite photovoltaics with lessons learned from industrial standards," *Nature Energy*, vol. 3, no. 6, pp. 459–465, jun 2018.

[98] G. Grancini, C. Roldán-Carmona, I. Zimmermann, E. Mosconi, X. Lee, D. Martineau, S. Narbey, F. Oswald, F. De Angelis, M. Graetzel, and M. K. Nazeeruddin, "One-Year stable perovskite solar cells by 2D/3D interface engineering," *Nature Communications*, vol. 8, p. 15684, jun 2017.

[99] F. Sahli, J. Werner, B. A. Kamino, M. Bräuninger, R. Monnard, B. Paviet-Salomon, L. Barraud, L. Ding, J. J. Diaz Leon, D. Sacchetto, G. Cattaneo, M. Despeisse, M. Boccard, S. Nicolay, Q. Jeangros, B. Niesen, and C. Ballif, "Fully textured monolithic perovskite/silicon tandem solar cells with 25.2% power conversion efficiency," *Nature Materials*, jun 2018.

[100] F. Dimroth, M. Grave, P. Beutel, U. Fiedeler, C. Karcher, T. N. D. Tibbits, E. Oliva, G. Siefer, M. Schachtner, A. Wekkeli, A. W. Bett, R. Krause, M. Piccin, N. Blanc, C. Drazek, E. Guiot, B. Ghyselen, T. Salvetat, A. Tauzin, T. Signamarcheix, A. Dobrich, T. Hannappel, and K. Schwarzburg, "Wafer bonded four-junction GaInP/GaAs//GaInAsP/GaInAs concentrator solar cells with 44.7% efficiency," *Progress in Photovoltaics: Research and Applications*, vol. 22, no. 3, pp. 277–282, mar 2014.

[101] S. P. Bremner, M. Y. Levy, and C. B. Honsberg, "Analysis of tandem solar cell efficiencies under AM1.5G spectrum using a rapid flux calculation method," *Progress in Photovoltaics: Research and Applications*, vol. 16, no. 3, pp. 225–233, may 2008. [Online]. Available: http://doi.wiley.com/10.1002/pip.799

[102] J. F. Geisz, R. M. France, K. L. Schulte, M. A. Steiner, A. G. Norman, H. L. Guthrey, M. R. Young, T. Song, and T. Moriarty, "Six-junction III–V solar cells with 47.1% conversion efficiency under 143 Suns concentration," *Nature Energy*, vol. 5, no. 4, pp. 326–335, apr 2020. [Online]. Available: http://www.nature.com/articles/s41560-020-0598-5

[103] J. Werner, B. Niesen, and C. Ballif, "Perovskite/Silicon Tandem Solar Cells: Marriage of Convenience or True Love Story? - An Overview," *Advanced Materials Interfaces*, vol. 5, no. 1, p. 1700731, jan 2018.

[104] Z. J. Yu, M. Leilaeioun, and Z. Holman, "Selecting tandem partners for silicon solar cells," *Nature Energy*, vol. 1, no. 11, p. 16137, sep 2016.

[105] Oxford PV, "Oxford PV sets world record for perovskite solar cell," 2018. [Online]. Available: https://www.oxfordpv.com/news/oxford-pv-sets-world-record-perovskite-solar-cell

[106] J. Werner, F. Sahli, F. Fu, J. J. Diaz Leon, A. Walter, B. A. Kamino, B. Niesen, S. Nicolay, Q. Jeangros, and C. Ballif, "Perovskite/Perovskite/Silicon Monolithic Triple-Junction Solar Cells with a Fully Textured Design," *ACS Energy Letters*, vol. 3, no. 9, pp. 2052–2058, sep 2018. [Online]. Available: https://pubs.acs.org/doi/10.1021/acsenergylett.8b01165

[107] F. Sahli, B. A. Kamino, J. Werner, M. Bräuninger, B. Paviet-Salomon, L. Barraud, R. Monnard, J. P. Seif, A. Tomasi, Q. Jeangros, A. Hessler-Wyser, S. De Wolf, M. Despeisse, S. Nicolay, B. Niesen, and C. Ballif, "Improved Optics in Monolithic Perovskite/Silicon Tandem Solar Cells with a Nanocrystalline Silicon Recombination Junction," *Advanced Energy Materials*, vol. 8, no. 6, p. 1701609, feb 2018.

[108] N. N. Lal, T. P. White, and K. R. Catchpole, "Optics and Light Trapping for Tandem Solar Cells on Silicon," *IEEE Journal of Photovoltaics*, vol. 4, no. 6, pp. 1380–1386, nov 2014.

[109] P. Loper, B. Niesen, S.-J. Moon, S. Martin de Nicolas, J. Holovsky, Z. Remes, M. Ledinsky, F.-J. Haug, J.-H. Yum, S. De Wolf, and C. Ballif, "Organic–Inorganic Halide Perovskites: Perspectives for Silicon-Based Tandem Solar Cells," *IEEE Journal of Photovoltaics*, vol. 4, no. 6, pp. 1545–1551, nov 2014.

[110] J. P. Mailoa, C. D. Bailie, E. C. Johlin, E. T. Hoke, A. J. Akey, W. H. Nguyen, M. D. McGehee, and T. Buonassisi, "A 2-terminal perovskite/silicon multijunction solar cell enabled by a silicon tunnel junction," *Applied Physics Letters*, vol. 106, no. 12, p. 121105, mar 2015.

[111] S. Albrecht, M. Saliba, J. P. Correa Baena, F. Lang, L. Kegelmann, M. Mews, L. Steier, A. Abate, J. Rappich, L. Korte, R. Schlatmann, M. K. Nazeeruddin, A. Hagfeldt, M. Grätzel, and B. Rech, "Monolithic perovskite/silicon-heterojunction tandem solar cells processed at low temperature," *Energy & Environmental Science*, vol. 9, no. 1, pp. 81–88, 2016.

[112] J. Werner, C.-H. Weng, A. Walter, L. Fesquet, J. P. Seif, S. De Wolf, B. Niesen, and C. Ballif, "Efficient Monolithic Perovskite/Silicon Tandem Solar Cell with Cell Area >1 cm 2," *The Journal of Physical Chemistry Letters*, vol. 7, no. 1, pp. 161–166, jan 2016.

[113] K. A. Bush, A. F. Palmstrom, Z. J. Yu, M. Boccard, R. Cheacharoen, J. P. Mailoa, D. P. McMeekin, R. L. Z. Hoye, C. D. Bailie, T. Leijtens, I. M. Peters, M. C. Minichetti, N. Rolston, R. Prasanna, S. Sofia, D. Harwood, W. Ma, F. Moghadam, H. J. Snaith, T. Buonassisi, Z. C. Holman, S. F. Bent, and M. D. McGehee, "23.6%-efficient monolithic perovskite/silicon tandem solar cells with improved stability," *Nature Energy*, vol. 2, no. 4, p. 17009, feb 2017.

[114] M. Saliba, T. Matsui, J.-Y. Seo, K. Domanski, J.-P. Correa-Baena, M. K. Nazeeruddin, S. M. Zakeeruddin, W. Tress, A. Abate, A. Hagfeldt, and M. Grätzel, "Cesium-containing triple cation perovskite solar cells: improved stability, reproducibility and high efficiency," *Energy & Environmental Science*, vol. 9, no. 6, pp. 1989–1997, 2016.

[115] M. A. Green, *Solar Cells Operating Principles, Technology and System Applications*. New Jersey: Prentice Hall, Inc, 1998.

[116] Sze, *Physics of Semiconductor Devices*, 3rd ed., ser. Environmental Science and Engineering. New Jersey: Joh Wiley and Sons, Inc, 2007.

[117] U. Wurfel, A. Cuevas, and P. Wurfel, “Charge Carrier Separation in Solar Cells,” *IEEE Journal of Photovoltaics*, vol. 5, no. 1, pp. 461–469, jan 2015. [Online]. Available: http://ieeexplore.ieee.org/lpdocs/epic03/wrapper.htm?arnumber=6960066

[118] R. Tung, “The physics and chemistry of the Schottky barrier height,” *Applied Physics Reviews*, vol. 1, no. 1, p. 011304, mar 2014. [Online]. Available: http://aip.scitation.org/doi/10.1063/1.4858400

[119] M. I. Saidaminov, A. L. Abdelhady, B. Murali, E. Alarousu, V. M. Burlakov, W. Peng, I. Dursun, L. Wang, Y. He, G. Maculan, A. Goriely, T. Wu, O. F. Mohammed, and O. M. Bakr, “High-quality bulk hybrid perovskite single crystals within minutes by inverse temperature crystallization,” *Nature Communications*, vol. 6, no. 1, p. 7586, nov 2015. [Online]. Available: http://www.nature.com/articles/ncomms8586

[120] D. A. Jacobs, Y. Wu, H. Shen, C. Barugkin, F. J. Beck, T. P. White, K. Weber, and K. R. Catchpole, “Hysteresis phenomena in perovskite solar cells: the many and varied effects of ionic accumulation,” *Physical Chemistry Chemical Physics*, vol. 19, no. 4, pp. 3094–3103, 2017. [Online]. Available: http://xlink.rsc.org/?DOI=C6CP06989D

[121] W. Tress, N. Marinova, T. Moehl, S. M. Zakeeruddin, M. K. Nazeeruddin, and M. Grätzel, “Understanding the rate-dependent J–V hysteresis, slow time component, and aging in CH 3 NH 3 PbI 3 perovskite solar cells: the role of a compensated electric field,” *Energy & Environmental Science*, vol. 8, no. 3, pp. 995–1004, 2015. [Online]. Available: http://xlink.rsc.org/?DOI=C4EE03664F

[122] P. Calado, A. M. Telford, D. Bryant, X. Li, J. Nelson, B. C. O’Regan, and P. R. Barnes, “Evidence for ion migration in hybrid perovskite solar cells with minimal hysteresis,” *Nature Communications*, vol. 7, no. 1, p. 13831, dec 2016. [Online]. Available: http://www.nature.com/articles/ncomms13831

[123] A. Mahboubi Soufiani, Z. Yang, T. Young, A. Miyata, A. Surrente, A. Pascoe, K. Galkowski, M. Abdi-Jalebi, R. Brenes, J. Urban, N. Zhang, V. Bulović, O. Portugall, Y.-B. Cheng, R. J. Nicholas, A. Ho-Baillie, M. A. Green, P. Plochocka, and S. D. Stranks, “Impact of microstructure on the electron–hole interaction in lead halide perovskites,” *Energy & Environmental Science*, vol. 10, no. 6, pp. 1358–1366, 2017.

[124] T. S. Sherkar, C. Momblona, L. Gil-Escrig, H. J. Bolink, and L. J. A. Koster, “Improving Perovskite Solar Cells: Insights From a Validated Device Model,” *Advanced Energy Materials*, vol. 7, no. 13, p. 1602432, jul 2017.

[125] S. Selberherr, *Analysis and Simulation of Semiconductor Devices.* Vienna: Springer Vienna, 1984. [Online]. Available: http://link.springer.com/10.1007/978-3-7091-8752-4

[126] A. Richter, F. Werner, A. Cuevas, J. Schmidt, and S. Glunz, “Improved Parameterization of Auger Recombination in Silicon,” *Energy Procedia*, vol. 27, pp. 88–94, 2012.

[127] J. Werner, G. Nogay, F. Sahli, T. C.-J. Yang, M. Bräuninger, G. Christmann, A. Walter, B. A. Kamino, P. Fiala, P. Löper, S. Nicolay, Q. Jeangros, B. Niesen, and C. Ballif, "Complex Refractive Indices of Cesium–Formamidinium-Based Mixed-Halide Perovskites with Optical Band Gaps from 1.5 to 1.8 eV," *ACS Energy Letters*, vol. 3, no. 3, pp. 742–747, mar 2018. [Online]. Available: https://pubs.acs.org/doi/10.1021/acsenergylett.8b00089

[128] G. F. Burkhard, E. T. Hoke, and M. D. McGehee, "Accounting for Interference, Scattering, and Electrode Absorption to Make Accurate Internal Quantum Efficiency Measurements in Organic and Other Thin Solar Cells," *Advanced Materials*, vol. 22, no. 30, pp. 3293–3297, aug 2010.

[129] L. Pettersson, L. Roman, and O. Inganas, "Modeling photocurrent action spectra of photovoltaic devices based on organic thin films," *Journal of Applied Physics*, vol. 86, no. 1, 1999.

[130] A. Pockett, G. E. Eperon, N. Sakai, H. J. Snaith, L. M. Peter, and P. J. Cameron, "Microseconds, milliseconds and seconds: deconvoluting the dynamic behaviour of planar perovskite solar cells," *Physical Chemistry Chemical Physics*, vol. 19, no. 8, pp. 5959–5970, 2017.

[131] M. Boccard and C. Ballif, "Influence of the Subcell Properties on the Fill Factor of Two-Terminal Perovskite–Silicon Tandem Solar Cells," *ACS Energy Letters*, vol. 5, no. 4, pp. 1077–1082, apr 2020. [Online]. Available: https://pubs.acs.org/doi/10.1021/acsenergylett.0c00156

[132] M. Saliba, J.-P. Correa-Baena, C. M. Wolff, M. Stolterfoht, N. Phung, S. Albrecht, D. Neher, and A. Abate, "How to Make over 20Perovskite Solar Cells in Regular (n–i–p) and Inverted (p–i–n) Architectures," *Chemistry of Materials*, vol. 30, no. 13, pp. 4193–4201, jul 2018. [Online]. Available: https://pubs.acs.org/doi/10.1021/acs.chemmater.8b00136

[133] C. Jeffrey Brinker and G. W. Scherer, *Sol-Gel Science - The Physics and Chemistry of Sol-Gel Processing*, 1st ed. Academic Press Inc, 1990.

[134] G. E. Jellison, L. A. Boatner, J. D. Budai, B.-S. Jeong, and D. P. Norton, "Spectroscopic ellipsometry of thin film and bulk anatase (TiO2)," *Journal of Applied Physics*, vol. 93, no. 12, pp. 9537–9541, jun 2003.

[135] G. Man, J. Schwartz, J. C. Sturm, and A. Kahn, "Electronically Passivated Hole-Blocking Titanium Dioxide/Silicon Heterojunction for Hybrid Silicon Photovoltaics," *Advanced Materials Interfaces*, vol. 3, no. 15, p. 1600026, aug 2016.

[136] N. D. Abazović, M. I. Čomor, M. D. Dramićanin, D. J. Jovanović, S. P. Ahrenkiel, and J. M. Nedeljković, "Photoluminescence of Anatase and Rutile TiO 2 Particles †," *The Journal of Physical Chemistry B*, vol. 110, no. 50, pp. 25 366–25 370, dec 2006.

[137] S. Hu, M. H. Richter, M. F. Lichterman, J. Beardslee, T. Mayer, B. S. Brunschwig, and N. S. Lewis, "Electrical, Photoelectrochemical, and Photoelectron Spectroscopic Investigation of the Interfacial Transport and Energetics of Amorphous TiO 2 /Si Heterojunctions," *The Journal of Physical Chemistry C*, vol. 120, no. 6, pp. 3117–3129, feb 2016.

[138] M. Stolterfoht, C. M. Wolff, J. A. Márquez, S. Zhang, C. J. Hages, D. Rothhardt, S. Albrecht, P. L. Burn, P. Meredith, T. Unold, and D. Neher, "Visualization and suppression of interfacial recombination for high-efficiency large-area pin perovskite solar cells," *Nature Energy*, vol. 3, no. 10, pp. 847–854, oct 2018. [Online]. Available: http://www.nature.com/articles/s41560-018-0219-8

[139] H. Miyamae, Y. Numahata, and M. Nagata, "THE CRYSTAL STRUCTURE OF LEAD(II) IODIDE-DIMETHYLSULPHOXIDE(1/2), PbI 2 (dmso) 2," *Chemistry Letters*, vol. 9, no. 6, pp. 663–664, jun 1980. [Online]. Available: http://www.journal.csj.jp/doi/10.1246/cl.1980.663

[140] G. V. Leite, E. A. Van Etten, M. M. Forte, and H. Boudinov, "Degradation of current due to charge transport in top gated P3HT—PVA organic field effect transistors," *Synthetic Metals*, vol. 229, pp. 33–38, jul 2017. [Online]. Available: https://linkinghub.elsevier.com/retrieve/pii/S0379677917301212

[141] S. Wozny, M. Yang, A. M. Nardes, C. C. Mercado, S. Ferrere, M. O. Reese, W. Zhou, and K. Zhu, "Controlled Humidity Study on the Formation of Higher Efficiency Formamidinium Lead Triiodide-Based Solar Cells," *Chemistry of Materials*, vol. 27, no. 13, pp. 4814–4820, jul 2015. [Online]. Available: https://pubs.acs.org/doi/10.1021/acs.chemmater.5b01691

[142] R. A. Z. Razera, H. I. Boudinov, F. S. B. Rodrigues, R. Z. Ferreira, and A. F. Feil, "Anomalous Current-Voltage Behavior in Al/TiO 2 /n-Si Structures," *physica status solidi (RRL) - Rapid Research Letters*, vol. 12, no. 6, p. 1800057, jun 2018.

[143] H. J. Snaith, A. Abate, J. M. Ball, G. E. Eperon, T. Leijtens, N. K. Noel, S. D. Stranks, J. T.-W. Wang, K. Wojciechowski, and W. Zhang, "Anomalous Hysteresis in Perovskite Solar Cells," *The Journal of Physical Chemistry Letters*, vol. 5, no. 9, pp. 1511–1515, may 2014. [Online]. Available: https://pubs.acs.org/doi/10.1021/jz500113x

[144] N. Pellet, "Investigations on hybrid organic-inorganic perovskites for high performance solar cells," Ph.D. dissertation, EPFL, 2017.

[145] E. H. Nicollian and J. R. Brews, *MOS (Metal Oxide Semiconductor) Physics and Technology.* New York: John Wiley & Sons, Inc., 1982.

[146] D. Schroder, *Semiconductor Device and Material Characterization*, 3rd ed. New Jersey: John Wiley & Sons, Inc., 2006.

[147] O. Breitenstein, J. Bauer, K. Bothe, D. Hinken, J. Müller, W. Kwapil, M. C. Schubert, and W. Warta, “Can Luminescence Imaging Replace Lock-in Thermography on Solar Cells?” *IEEE Journal of Photovoltaics*, vol. 1, no. 2, pp. 159–167, oct 2011. [Online]. Available: http://ieeexplore.ieee.org/document/6047555/

[148] M. Burgelman, P. Nollet, and S. Degrave, “Modelling polycrystalline semiconductor solar cells,” *Thin Solid Films*, vol. 361-362, pp. 527–532, feb 2000. [Online]. Available: https://linkinghub.elsevier.com/retrieve/pii/S0040609099008251

[149] K. M. Kim, B. J. Choi, Y. C. Shin, S. Choi, and C. S. Hwang, “Anode-interface localized filamentary mechanism in resistive switching of TiO2 thin films,” *Applied Physics Letters*, vol. 91, no. 1, p. 012907, jul 2007.

[150] C. Neusel, H. Jelitto, and G. A. Schneider, “Electrical conduction mechanism in bulk ceramic insulators at high voltages until dielectric breakdown,” *Journal of Applied Physics*, vol. 117, no. 15, p. 154902, apr 2015.

[151] M. Lampert and P. Mark, *Current Injection in Solids.* Academic Press Inc, 1970.

[152] T. Busani and R. A. B. Devine, “Dielectric and infrared properties of TiO 2 films containing anatase and rutile,” *Semiconductor Science and Technology*, vol. 20, no. 8, pp. 870–875, aug 2005.

[153] W. Brown and W. Grannemann, “Current-voltage characteristics of metal-titanium dioxide-silicon structures,” *Thin Solid Films*, vol. 51, no. 1, pp. 119–132, may 1978.

[154] A. J. Mozer, N. S. Sariciftci, A. Pivrikas, R. Österbacka, G. Juška, L. Brassat, and H. Bässler, “Charge carrier mobility in regioregular poly(3-hexylthiophene) probed by transient conductivity techniques: A comparative study,” *Physical Review B*, vol. 71, no. 3, p. 035214, jan 2005.

[155] X. Zhang, J.-X. Shen, W. Wang, and C. G. Van de Walle, “First-Principles Analysis of Radiative Recombination in Lead-Halide Perovskites,” *ACS Energy Letters*, vol. 3, no. 10, pp. 2329–2334, oct 2018. [Online]. Available: https://pubs.acs.org/doi/10.1021/acsenergylett.8b01297

[156] S. Hsu, R. Whittier, and C. Mead, “Physical model for burst noise in semiconductor devices,” *Solid-State Electronics*, vol. 13, no. 7, pp. 1055–1071, jul 1970. [Online]. Available: https://linkinghub.elsevier.com/retrieve/pii/0038110170901024

[157] S. Wu, R. Chen, S. Zhang, B. H. Babu, Y. Yue, H. Zhu, Z. Yang, C. Chen, W. Chen, Y. Huang, S. Fang, T. Liu, L. Han, and W. Chen, “A chemically inert bismuth interlayer enhances long-term stability of inverted perovskite solar cells,” *Nature Communications*, vol. 10, no. 1, p. 1161, dec 2019. [Online]. Available: http://www.nature.com/articles/s41467-019-09167-0

[158] E. Yoo, M. Lyu, J.-H. Yun, C. Kang, Y. Choi, and L. Wang, “Bifunctional resistive switching behavior in an organolead halide perovskite based Ag/CH 3 NH 3 PbI 3x Cl x /FTO structure,” *Journal of Materials Chemistry C*, vol. 4, no. 33, pp. 7824–7830, 2016. [Online]. Available: http://xlink.rsc.org/?DOI=C6TC02503J

[159] B. Lüssem, C.-M. Keum, D. Kasemann, B. Naab, Z. Bao, and K. Leo, “Doped Organic Transistors,” *Chemical Reviews*, vol. 116, no. 22, pp. 13 714–13 751, nov 2016. [Online]. Available: https://pubs.acs.org/doi/10.1021/acs.chemrev.6b00329